ADMITTANCE SPECTROSCOPY STUDY OF POLYMER DIODES IN SMALL MAGNETIC FIELDS

by

Kamdem Djidjou Thaddée

A dissertation submitted to the faculty of
The University of Utah
in partial fulfillment of the requirements for the degree of

Doctor of Philosophy

in

Physics

Department of Physics and Astronomy

The University of Utah

August 2013

The University of Utah Graduate School

STATEMENT OF DISSERTATION APPROVAL

The dissertation of **Kamdem Djidjou Thaddée**

has been approved by the following supervisory committee members:

Andrey Rogachev	, Chair	**11/05/2012** Date Approved
Mikhail Raikh	, Member	**11/05/2012** Date Approved
Jordan Gerton	, Member	**11/05/2012** Date Approved
Stephan LeBohec	, Member	**11/05/2012** Date Approved
Sivaraman Guruswamy	, Member	**11/05/2012** Date Approved

and by **David Kieda**, Chair of the Department of **Physics and Astronomy**

and by Donna M. White, Interim Dean of The Graduate School.

ABSTRACT

We performed a systematic study of bipolar and unipolar diodes based on the π-conjugated polymer, 2-methoxy-5-(2'-ethylhexyloxy) (MEH-PPV), using electronic and magneto-transport measurements with magnetic field in the range 0 mT – 180 mT and admittance spectroscopy in the frequencies varying from 1 Hz to 10 MHz. The admittance spectra of bipolar devices reveal two relaxation processes with distinct time scales that are influenced by the magnetic field. The slower process, which dominates the device capacitance at frequencies less than 10 Hz, is attributed to the trap-assisted monomolecular recombination. The second faster process is attributed to the electron-hole bimolecular recombination kinetics. When magnetic field of magnitude 30 mT is applied, τ_2 decreases by approximately 30 %. We observed that bipolar devices have strong divergent contribution to the device differential capacitance at low frequencies. It is positive at low biases voltages, turns negative at intermediate biases, and becomes positive again at stronger biases. In addition, by carefully selecting bias voltage, we were able to tune some bipolar diodes from the state with the negative capacitance to the state with the positive capacitance just by applying magnetic field.

The magneto-conductance has a characteristic cutoff frequency that shifts to higher frequencies with increasing bias voltages. In particular, the magneto-conductance at 10 MHz in a bipolar device was measured to be 4.5 % in the magnetic field of magnitude 30 mT. For bipolar devices, the frequency-dependent response of the device admittance to

the small magnetic field is identical to the response of the admittance to the small increase in the bias voltage in zero magnetic field. We found that the response of the admittance on the magnetic field is consistent with the polaron-polaron model of the organic magnetoresistance. The admittance of unipolar diodes did not reveal any magnetic field.

CONTENTS

LIST OF FIGURES

ACKNOWLEDGEMENTS

I would like to express my deep and sincere gratitude to my advisor, Prof. Andrey Rogachev. He exposed me to different experimental skills as well as theoretical knowledge of condensed matter physics. This work would have not been achieved without his guidance, patience and availability.

I would also like to thank all the members of my supervisory committee, Prof. Mikhail Raikh, Prof. Siva Guruswamy, Prof. Jordan Gerton and Prof. Stephan Lebohec who took time to thoroughly review my thesis and provide valuable comments and suggestions.

I am deeply thankful to Dr Matt Delong, Dr Randy Polson, Dr Brian Baker to have trained me to valuable technical skills.

A special thank is addressed to my lab members Dr Hyunjeong Kim, Shirin Jamali, Kevin Davenport and James Skowronek.

I am deeply thankful to all the professors who guided me in course study and to the staff of the department of Physics to have made my stay here comfortable.

Finally, I would acknowledge the constant and important support of my parents, my brothers and sisters. This work is dedicated to the entire Djidjou's family.

CHAPTER 1

INTRODUCTION

The light emission from a solid material after an application of electrical field was first reported by Henry Joseph Round in 1907. This phenomenon was termed electroluminescence [1]. Electroluminescence is the emission of optical radiation (ultraviolet, visible, or infrared) as a result of electronic excitation in a device or material, excluding any radiation that is purely the result of the temperature of the material (incandescence) [2]. The solid material used for the observation was SiC (carborundum) and the voltage applied was in the range of 10 V to 110 V. It was proposed that the light resulted from the electrodes contacts with SiC, which were forming Schottky diodes. Two decades later, Oleg Losev proved that the emitted light was not resulting from incandescence and postulated that light was emitted by a process "very similar to cold electronic discharge" [3]. The efficiency of the LED made of SiC films was very low, about 0.005% [1].

In the mid of the twentieth century, the era of III-V compound semiconductors started. The research on these materials led to the report of the first LEDs based on GaAs.

Over the years, the field has grown and extended to organic materials. Until the 1970s, polymers were considered to be insulators and were employed in numerous applications such as electrical wire insulators or insulating interlayers in capacitors [4].

However, the work of Mott and Gurney in1940, showed the possibility to inject electrons or holes from a suitable contact into insulators or semiconductors. Based on that, the first organic electroluminescent devices, made with a polymer polyvinyl carbazole (PVK) were reported in 1975 [5], two years before A. J. Heeger, A. G. MacDiarmid, and H. Shirakawa discovered that conjugated polymers have semiconductor properties [6,7]. These three researchers received the Nobel Prize in Chemistry for the discovery and development of conductive polymers. These materials, oppositely to their inorganic counterparts, present advantages such as relative ease of fabrication, chemical variability, flexibility and low cost.

The discovery of electroluminescence in poly-p-phenylenevinylene based devices [8] accelerated the research in organic light emitting devices.

The understanding of the transport mechanism in organic semiconductors is still under study. Besides DC transport measurements, several types of dynamical measurements have been used in the field, such as dark-injection space-charge-limited current transient, transient electroluminescence, time-of-flight (TOF) technique, admittance spectroscopy. In the first three approaches, the mobility of charge carriers is obtained from the delay time of the carriers propagating across the film, after their injection into an initially charge-free organic film [9]. This usually requires a thick film ($\geq 1\mu m$). Admittance spectroscopy helps to distinguish the different relaxation processes that occur on different time scales and get information about the charge carriers' distribution inside the OLED.

In several recent experiments, the response of organic light emitting diodes to an alternating magnetic field has been studied. Recently, Wagemans *et al.* showed that the

magnetoconductance decreases when the frequency of the alternating magnetic field is increased. Using admittance spectroscopy, they showed that the decrease is stronger for lower voltages and is linked to the presence of a negative capacitance [10]. Previously, Veeraraghavan *et al.* studied the frequency response of OMAR in Alq_3 sandwiched between PEDOT and Ca layers and placed in AC magnetic field. They showed that the OMAR was not frequency dependent up to 100 *kHz* and concluded that the OMAR mechanism is faster than 10 μs [11].

This thesis presents the study of the effect of small magnetic fields in the range of 0 *mT* to 180 *mT* on polymer diodes based on poly(2-methoxy-5-(2'-ethyl)-hexoxy-1,4-phenylenevinylene) (MEH-PPV) or poly[2,5-dioctyloxy-1,4-phenylenevinylene] (DOO-PPV) using admittance spectroscopy in the frequency range of 1 *Hz* to 10 *MHz* at room temperature.

Here, the frequency response of the magnetic field effect on organic light emitting diodes results from the application of an AC electric field superimposed to a DC electric field. With admittance spectroscopy, we probed the different relaxation processes occurring in the devices. This helps for a better understanding of the transport mechanism in polymer diodes and the overall improvement of their efficiency.

In Chapter 2 the details of the device structure, the π-conjugated polymers properties, the conduction and light emission mechanisms in OLED are presented.

In Chapter 3, a review of the different models explaining the organic magnetoresistance (OMAR) will be presented. That includes the bipolaron model, the polaron pair model and the exciton model.

In Chapter 4, the experimental methods for samples fabrications and measurements are presented.

In Chapter 5, the theory of current injection into solids and the results of DC measurements are presented and analyzed.

In Chapter 6, the theory of admittance spectroscopy and the results of AC measurements are presented.

A conclusion ends the work.

1.1 References

1. E. Fred Schubert, "Light-emitting diodes," Cambridge, (2003).

2. S. M. Sze, Kwok K. Ng, "Physics of semiconductor devices," 3rd edition, Wiley (2003).

3. Losev Oleg. V., "Luminous carborundum detector and detection effect and oscillations with crystals," Philosophical Magazine 7, 1024 (1928).

4. K. Mullen, U. Scherf, "Organic light-emitting devices, synthesis, properties, and applications," Wiley, (2006).

5. R. H. Partridge, Radiation Sources, U.S. Patent 3,995,299, (1976).

6. C. K. Chiang, C. R. Fincher, Y.W. Park, A. J. Heeger, H. Shirakawa, E. J. Louis, S. C. Gau, and A. G. MacDiarmid, "Electrical conductivity in doped polyacetylene," Phys. Rev. Lett. **39**, 1098 (1977).

7. H. Shirakawa, E. J. Louis, A. G. MacDiarmid, C. K. Chiang, and A. J. Heeger, "Synthesis of electrically conducting organic polymers: halogen derivatives of polyacetylene, $(CH)_x$," Chem. Commun. **16**, 578 (1977).

8. J. H. Burroughes, D. D. C. Bradley, A. R. Brown, R. N. Marks, K. Mackay, R. H. Friend, P. L. Burns, and A. B. Holmes, "Light-emitting diodes based on conjugated polymers," Nature, **347**, 539 (1990).

9. D. Poplavskyy, F. So, "Bipolar carrier transport in a conjugated polymer by admittance spectroscopy," J. Appl. Phys. **99**, 033707 (2006).

10. W.Wagemans, P. Janssen, E. H. M. van der Heijden, M. Kemerink, and B. Koopmans, "Frequency dependence of organic magnetoresistance," Appl. Phys. Lett. **97**, 123301 (2010).

11. G. Veeraraghavan, T. D. Nguyen, Y. Sheng, O. Mermer, and M. Wohlgenannt, "An 8 x 8 pixel array pen-input OLED screen based on organic magnetoresistance," IEEE, Vol. **54**, No **6** (2007).

CHAPTER 2

ORGANIC LIGHT EMITTING DIODES

Organic Light Emitting Diodes are organic semiconductor devices. Organic semiconductors is the class of carbon-based compounds having an alternating sequences of single and double or single and triple bounds between the carbon atoms. The organic semiconductors are of two groups of materials: the conducting polymers which are macromolecules made up of chains of monomeres and the small molecular weight compounds which have a molecular weight below 1*kg/mol*.

The first attempts to develop organic electroluminescent (EL) devices based on small molecules in 1960s by Helfrich gave significant current output when the voltage around 100 *V* or above was applied across a 5-mm-thick anthracene sample with diameter 1 *cm* (Figure 2.1) [1]. Using thin organic films of the same material, Vincett and coworkers reported electroluminescence below 30 *V*. In 1987, Tang used a double layer structure of organic thin films (Diamine/Alq_3) to realize for the first time an efficient OLED (1% photon/electron) at driving voltage below 10 *V* (Figure 2.2) [2]. Three years later, Burroughes et *al.* [3] reported the first polymer OLED based on unsubstituted poly (p-phenylenevinylene) (PPV) operating below 15 *V* (Figure 2.3). This work was followed by a work on a polymer OLED made with a solution-processible polymer, poly (2-methoxy-5-(2'-ethyl)-hexoxy-1,4-phenylenevinylene) (MEH-PPV) sandwiched between two different electrodes. Since then, MEH-PPV has become one of the most widely

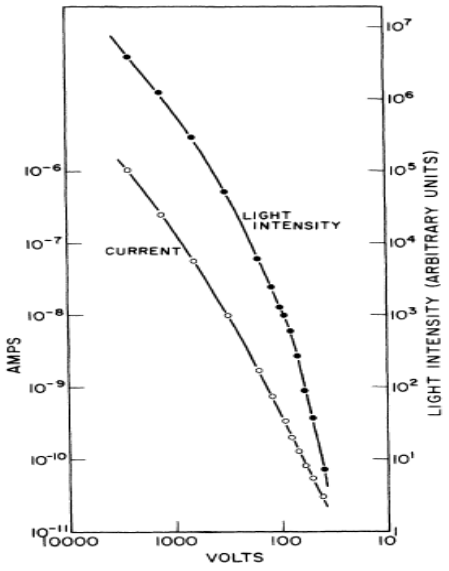

Figure 2.1 *I vs. V for anthracene. From Ref. [1]*

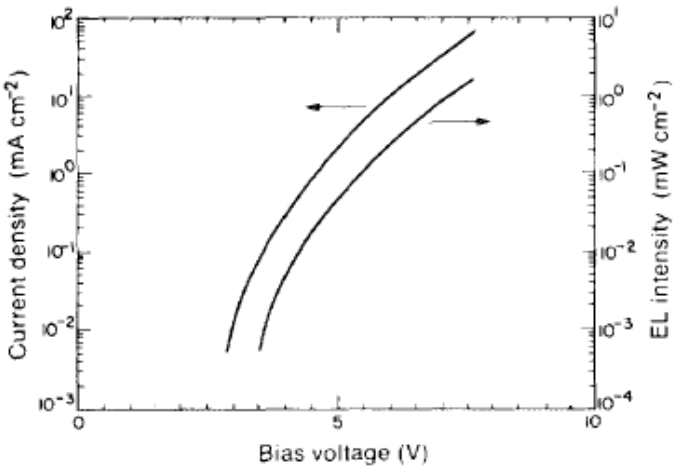

Figure 2.2 *Current density vs. voltage for organic thin film of diamine/Alq_3. From Ref. [2]*

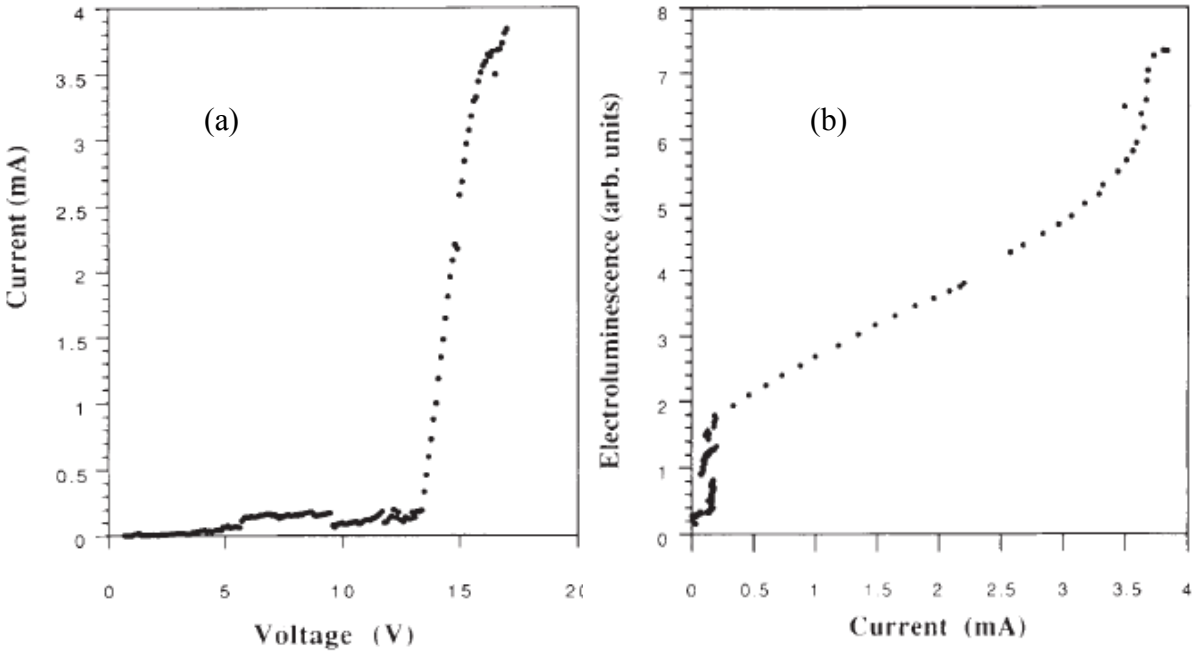

Figure 2.3 *(a) IV, (b) electroluminesce vs. current for 70 nm thick PPV film. From Ref. [3]*

used polymers for the investigation of properties of polymer semiconductors. This soluble polymer derivative has intrinsically low charge impurity (typically below 10^{14} / cm^3) and high photoluminescent efficiency [4].

2.1 Device structure

OLEDs used in this work are based on polymers layers sandwiched between two different electrodes, in cross-bar geometry. We measured a series of bipolar samples (samples in which holes and electrons were injected from electrodes at appropriate bias voltages) and unipolar samples (samples where the only expected charge carriers are holes). Both types of devices are made on glass substrates covered with a transparent conducting ITO which is anode in the forward bias mode. A thin layer of Ca, deposited by e-beam evaporation and protected from oxidation by a thick layer of Al, is the cathode for bipolar samples, whilst a layer of Au plays the role of cathode in unipolar samples. For majority of the samples, on top of the ITO anode, a thin layer of poly (3,4-ethylene dioxy-2,4-thiophene)-polystyrene sulfonate (PEDOT-PSS) was spin-coated before a layer of poly(2-methoxy-5-(2'-ethyl)-hexoxy-1,4-phenylenevinylene) (MEH-PPV) or poly[2,5-dioctyloxy-1,4-phenylenevinylene] (DOO-PPV) was spin-coated.

The PEDOT-PSS layer inserted between the ITO and the electroluminescent MEH-PPV provides multiple benefits for the polymer OLED devices [4]:

- It serves as a polymeric anode and matches the highest occupied molecular orbit (HOMO) of the MEH-PPV to facilitate hole injection
- It serves as a planization layer to smoothing the rough ITO surface and eliminating shorts due to sharp spikes on the ITO surface

- It serves as a chemical barrier preventing inorganic atoms in the ITO layer (such as indium) from diffusing into the electroluminescent polymer layer.

In all samples, the thicknesses of Ca and Al are, respectively, 20 *nm* and 100 *nm*. Devices with variable thicknesses of MEH-PPV were measured. The devices were sealed with a glass slide to provide protection against oxidation. Multilayers structures of the devices are shown in Figure 2.4.

All polymers used in devices were π-conjugated polymers. The properties of these polymers are shown in the next section.

2.2 π-conjugated polymers

Π-conjugated polymers are polymers in which single and double or single and triple bonds alternate throughout the polymer backbone. Π bonds are the second and third bonds of a double or triple bonds between C atoms. In this class of polymers, the carbon

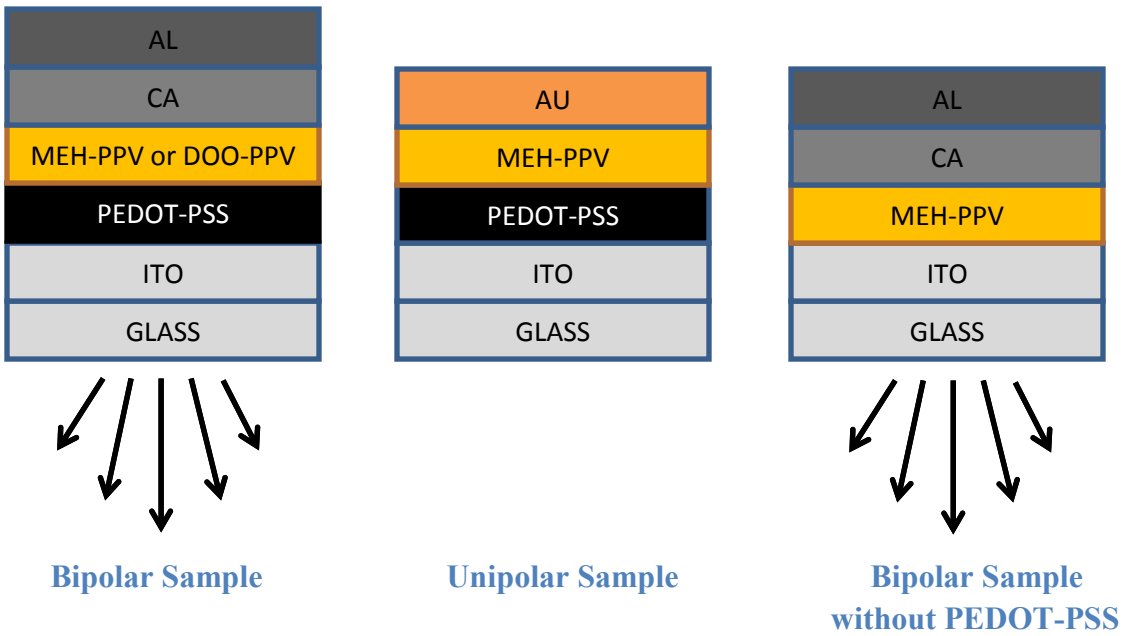

Figure 2.4: *Multilayer structures of devices used*

orbitals are in the sp^2p_z configuration (Figure 2.5). Therefore, there is one unpaired electron per carbon atom: an electron on p_z atomic orbital called the π electron. The three sp^2 electrons are covalently bonded to neighboring carbons atoms in the chain on either side and to the side-group via σ molecular orbitals. The remaining electron in the p_z atomic orbital forms a covalent bond via a π molecular orbital with a neighboring carbon atom in the chain on one side only; p_z orbitals of successive carbon atoms along the chain overlap, forming the delocalized π bands. The number of carbon atoms within the repeat unit determines the number of π bands. Conjugated polymers can exhibit semiconducting or metallic properties, depending on whether the bands are filled or partially filled [4]. When the energy gap, that is the difference between the highest occupied molecular π orbital (HOMO) and the lowest unoccupied molecular π* orbital (LUMO), is in the range 1.5 *eV* to 3 *eV*, the conjugated polymer is a semiconductor. Due to the overlap of π orbital wave functions of adjacent carbon atoms, the electrons occupying such orbitals are relatively delocalized. In the perfect isolated polymer, the delocalized π electron cloud extends along the whole length of the chain. However, in the real chain various defects such as impurities (e.g., H, O, Cl, or F atoms which eliminate the double bond, etc.) or intrinsic defects (e.g., kinks, torsional conformations, a cross-link with a neighboring chain, etc.) break the conjugation. In the typical polymer film, the length of a conjugated segment typically varies from ~5 repeat units to ~ 15 repeat units. The HOMO-LUMO gap decreases with increasing conjugation length to an asymptotic value usually reached at ~10 repeat units. An important characteristic of both polymer and small molecular films is disorder. Although polymer chains may be quite long, typically the π-conjugation

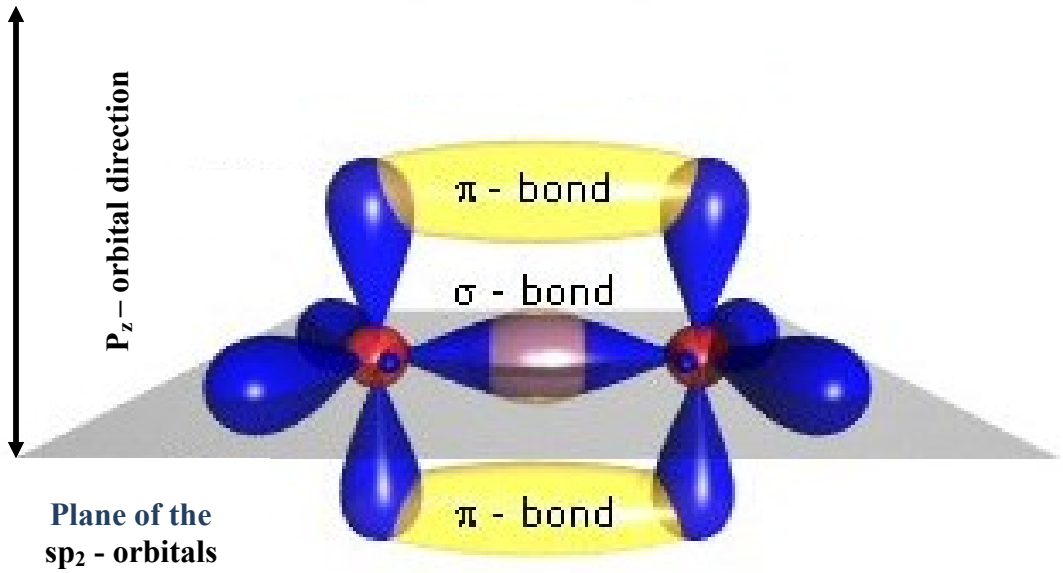

Figure 2.5 *Scheme of the orbitals and bounds for two sp2-hybridised carbon atoms. Adapted from www.orgworld.de*

is interrupted by topological defects. Hence the conjugated polymers can be considered as an assembly of conjugated segments [5].

For PPV (Figure 2.6) [4], each unit contains 8 carbon atoms. Using Hund's rules for the spins, the four π orbitals with the lowest energy are filled and the four π orbitals with the highest energy are empty. The energy gap here is ≈ 2.5 *eV*. PPV is insoluble. Its derivative, MEH-PPV (Figure 2.6), obtained by replacing the alkyl groups of PPV derivatives with alkoxy groups on the 2 and 5 positions, is soluble in nonpolar organic solvents (such as xylene or toluene) and its energy gap can be reduced from 2.5 *eV* to 2.1 *eV*.

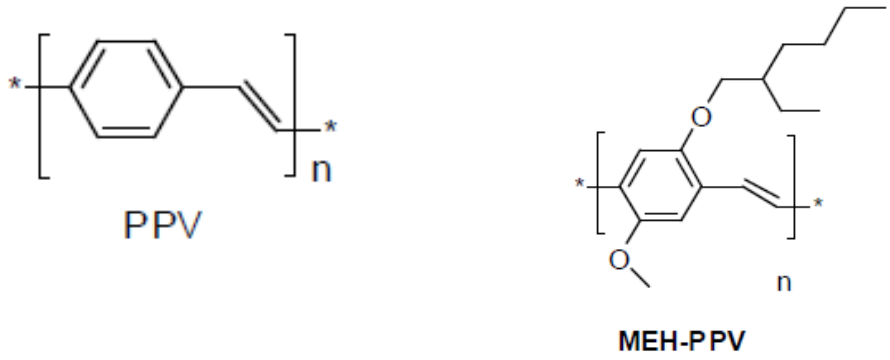

Figure 2.6 *Chemical unit of PPV and MEH-PPV*

2.3 Conduction and light emission mechanisms in OLEDs

In polymers, the intermolecular bonding is weak, of Van-der-Waals type, due to the separation distance between molecular chains. This makes the mobility of charge carriers in these materials low. In MEH-PPV, Bozano *et al.* obtained holes and electrons mobilities, respectively, of $1 \pm 0.5 \times 10^{-7} cm^2 / Vs$ and $1 \pm 0.5 \times 10^{-8} cm^2 / Vs$ at room temperature [6].

The main transport mechanism in polymer semiconductors is hopping. In these materials, the electron exchange interactions are much smaller than in inorganic semiconductor, while the electron-phonon interactions may be the same. Then, there is a possibility that the electron-phonon interactions may dominate in polymers. Due to this strong electron and lattice coupling, charge carriers in the polymer OLEDs are rather localized to molecules chains, and therefore the charge carrier motion can locally distort the lattice. For that reason, the charge carriers in polymers are either positive polarons (p^+) with spin 1/2 or negative polarons (e^-) with spin -1/2 instead of electrons and holes. Polarons are localized on segment chains and move from chain to chain through hopping. Their motion can lead to the formation of the following microscopic species [7]:

- Polaron pairs are formed by oppositely charged polarons on adjacent chains, due to Coulombic interaction
- Bipolarons are formed by charged polarons on the same segment. They can be doubly positively charged or doubly negatively charged
- Excitons which are intrachain species resulting from Coulombic interactions between two oppositely charged polaron separated by a distance less than the exciton capture radius.

Due to its spin, the charged polaron interacts with the nuclear spin of surrounding hydrogen nuclei; that is known as hyperfine interaction (HFI). Recently, by replacing protons with deuterons (that have smaller HFI constant), in an organic layer, it was demonstrated that indeed the HFI plays a crucial role in organic magnetoresistance effect [8]. The spin-orbit coupling is generally small in polymer due to the low atomic number Z of carbon atoms.

The disorder in polymers also induce locally varying polarization energies [9]; this leads to a Gaussian density of states for the distribution of transport sites (Figure 2.7).

The light emission of polymer OLEDs depend on charge carriers' injection into the EL polymer and charge carriers transport through the EL polymer.

2.3.1 Charge carriers' injection into EL polymer

Charge carriers injection is determined by the work functions of electrodes materials and the interfaces between electrodes and organic EL polymer. The EL polymers used for this thesis are undoped MEH-PPV and DOO-PPV. The OLEDs analyzed can be classified in two groups: bipolar OLEDs (where the charge carriers are positive and negative polarons) and unipolar OLEDs (where the expected charge carriers are just of

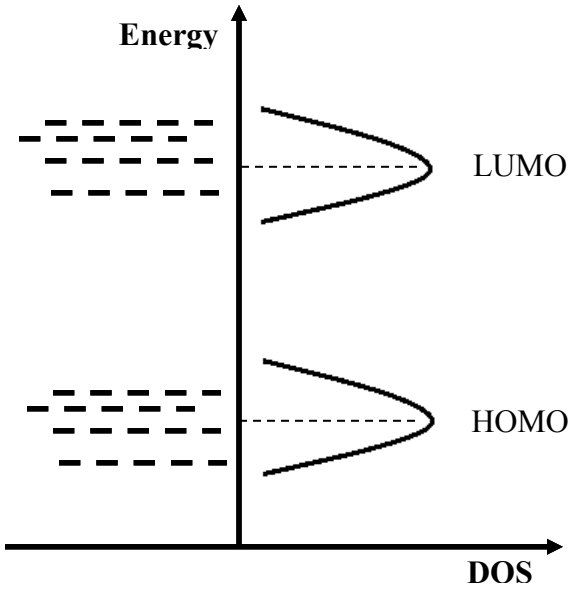

Figure 2.7: *Gaussian density of states (DOS) distribution of molecular sites for LUMO and HOMO*

one sign; for the polymer used here, they are positive polarons). Our bipolar samples had the following multilayers structures ITO/PEDOT-PSS/MEH-PPV/Ca/Al, ITO/PEDOT-PSS/DOO-PPV/Ca/Al, ITO/MEH-PPV/Ca/Al. The only unipolar multilayer layer structure studied was ITO/PEDOT-PSS/MEH-PPV/Au.

The characteristics energies for the polymers and inorganic elements used in the studied OLEDs are shown in Figure 2.8.

For bipolar devices, not under applied electric field, the difference in work function between the electrodes results in the diffusion of electrons from the cathode (Ca) to the anode (PEDOT-PSS or ITO). This is shown in Figure 2.9 (a). Due to this diffusion, the interface EL polymer/cathode is positively charged while the interface EL polymer/anode is negatively charged; and an electric field opposite to the flow of electrons is created in the EL layer. This diffusion of electrons to the anode stops when the Fermi levels of both

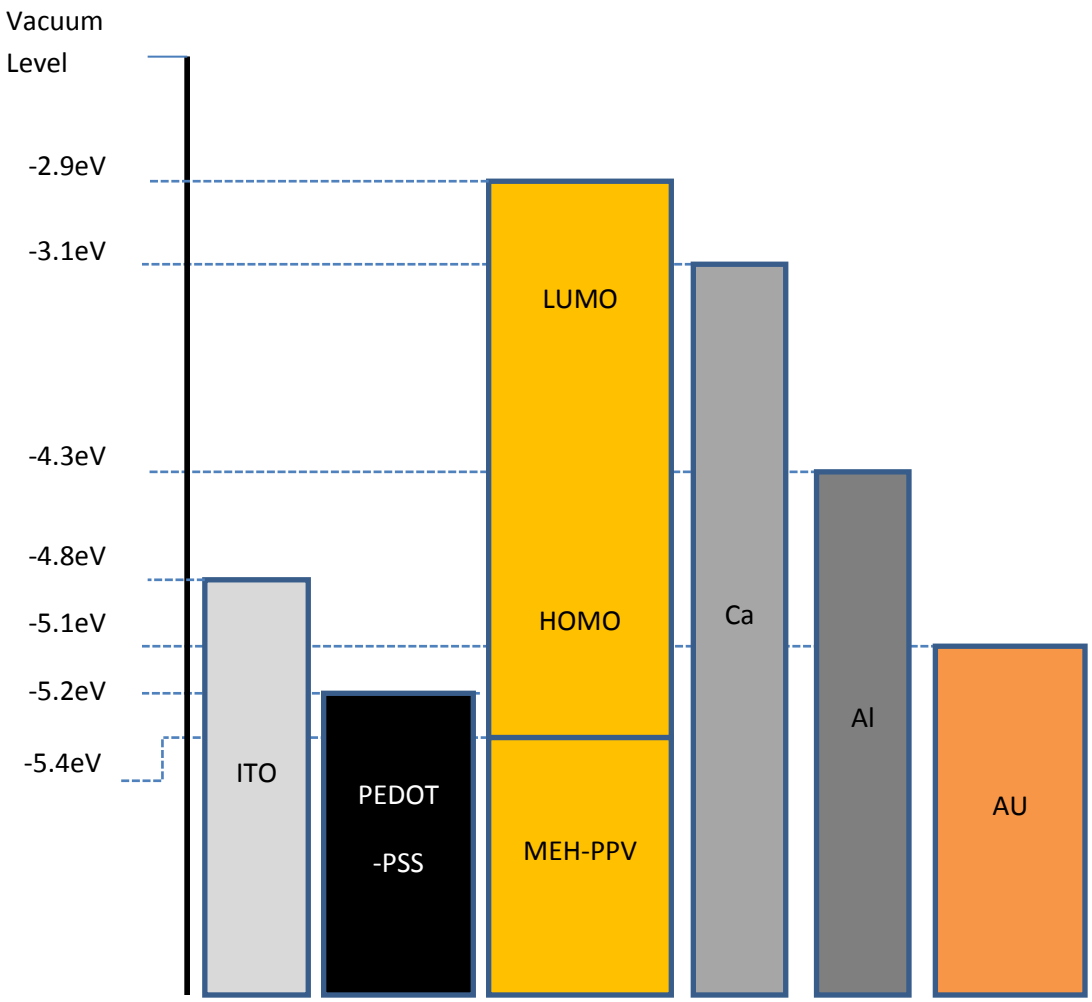

Figure 2.8 *Energy levels of different materials used in samples fabrication*

electrodes are aligned. The application of a potential in the forward bias affects the Fermi levels of both electrodes as shown in Figure 2.9 (b). When the driving voltage equals the built-in potential (the electrical potential which results from the difference between the work functions of the anode and the cathode), the HOMO and LUMO of the EL layer are horizontal. For any bias voltage greater than the built-in potential (V_{bi}), holes are injected from the anode to the EL polymer and electrons are injected from the cathode to the EL polymer (Figure 2.9 (c)).

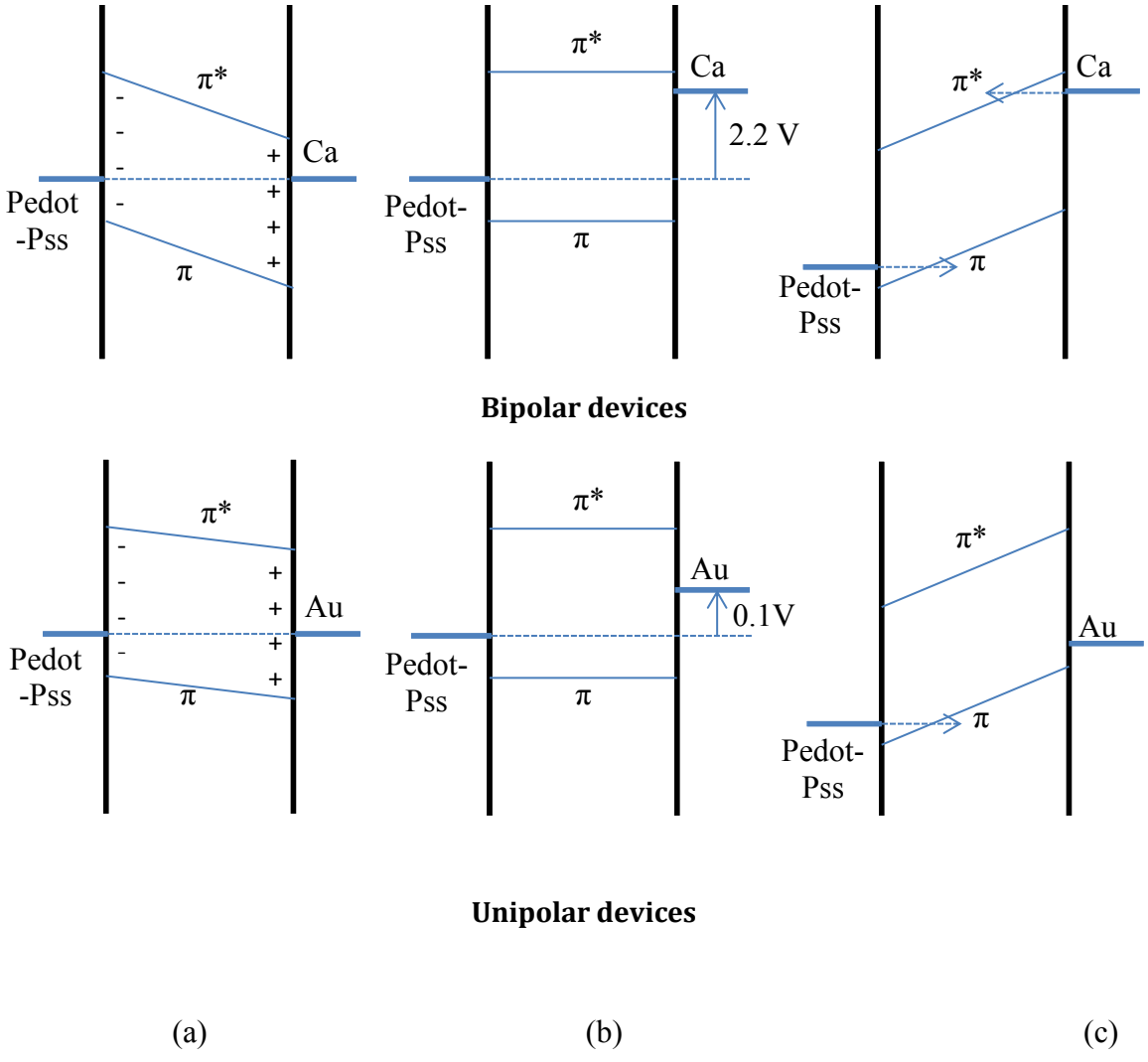

Figure 2.9: *Energy levels diagrams of a polymer diode under different bias voltage regimes*

The injection mechanism depends on the heights of the barriers which result from the difference in work functions of the HOMO and LUMO bands of the EL polymer with the anode and cathode materials, respectively.

For barrier heights less than 100 *meV* (comparable to thermal energy at room temperature), thermionic emissions (thermal-assisted carrier tunneling) are the dominating mechanism of injection at room temperature (Figure 2.10(a)). The current flow is described by the Schottky emission process [10]:

$$J = \frac{4\pi q m k^2}{h^3} T^2 \exp\left(-\frac{q\Phi_B}{kT}\right)\left[\exp\left(\frac{qV}{kT}\right)-1\right] \tag{2.1}$$

where m is the effective mass of the electron (hole), k is the Boltzmann's constant, h is Planck's constant, T is the temperature, q is the elementary charge, Φ_B is the barrier height and V is the applied voltage.

When the barrier height is large, the tunneling is dominant. For a barrier with triangular shape, the tunneling is described by Fowler-Nordheim theory (Figure 2.10(b)). The current flow is given by the equation [10]:

$$J = \frac{q^2 V^2}{8\pi h \Phi_B} \exp\left[-\frac{8\pi\sqrt{m}(q\Phi_B)^{3/2}}{3hqV}\right] \tag{2.2}$$

where m is the mass of the carrier (electron or hole).

(a) Schottky thermal injection

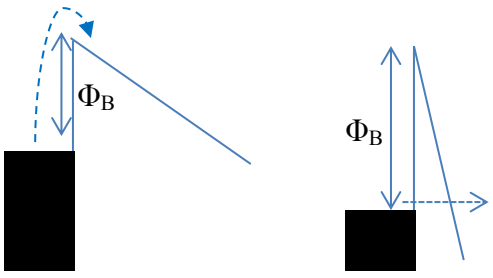

(b) Fowler-Nordheim tunneling injection by local high electric field

Fiure. 2.10: *Injection mechanisms depending on the barrier height*

2.3.2 Charge carriers' transport through EL polymer

The injected charge carriers move through the EL polymer due to the applied electric field. The transport depends on the bulk properties of the EL polymer. In unipolar PPV-based OLEDs with ohmic contacts, and with relatively large thickness (larger than 150 *nm*), the hole current is space-charge-limited and the electron current is traps-limited. The high mobility of holes compared to electrons is responsible of space-charge-limited hole current (SCLC), while the defects with energy levels below the conduction band that occur due to disorder, structural imperfectness or chemical impurities are responsible of traps-limited electron current [13]. The SCLC enhances the internal electric field of the device. In the absence of traps, the current generated by one type of charge carriers is given by Child's law [10]:

$$J = \frac{9\varepsilon\varepsilon_0 \mu V^2}{8L^3} \tag{2.4}$$

where ε is the relative dielectric constant, ε_0 is the dielectric constant, μ is the charge mobility and L is the device thickness.

In SCLC regime without traps, the mobility of the charge carrier often follows Poole-Frenkel formula as [6]:

$$\mu = \mu_0 \exp(\beta V / L) \tag{2.5}$$

where μ_0 is the zero-field mobility and β is the electric field coefficient.

When the driving electric potential is less than V_{bi}, the current flow is governed by Ohm's law [11].

2.3.3 Light emission mechanism

The drift of e^- and p^+ towards each other in the EL-polymer under the presence of the bias voltage can lead to the formation of polaron pairs (Figure 2.11 (i)) when they are on adjacent chains, i.e., their separation is less than the Coulomb capture radius defined by the equation

$$r_c = \frac{q^2}{4\pi\varepsilon_0\varepsilon_r kT} \tag{2.6}$$

The polaron pairs can latter dissociate in positive polaron and negative polaron (Figure 2.11(ii)), or form exciton when e^- and p^+ are captured in a single molecule. The exciton can decay to the ground state by recombination of electron and hole and emission of a photon of light $h\nu$ (Figure 2.11(iii)) [12]. Due to the spin of the charged polarons, the polaron pairs and excitons will be either in singlet configuration $S = \frac{1}{\sqrt{2}}\left(\left|\uparrow\downarrow\right\rangle - \left|\downarrow\uparrow\right\rangle\right)$ or in triplet configuration $T_0 = \frac{1}{\sqrt{2}}\left(\left|\uparrow\downarrow\right\rangle + \left|\downarrow\uparrow\right\rangle\right)$, or $T_1 = \left|\uparrow\uparrow\right\rangle$, or $T_{-1} = \left|\downarrow\downarrow\right\rangle$.

The theory revealed that polaron pairs form both singlet excitons and triplet excitons in the ratio of 1 to 3. Since triplet states' energy is less than singlet states' energy and that radiative transition from triplet state is forbidden for polymers, only singlet excitons decay radiatively and emit light (Figure 2.12) [5]. Hence maximum EL quantum efficiency is limited to 25%.

The internal EL quantum efficiency η_ϕ is the ratio of the number of emitter photons inside the device divided by the number of charge carriers injected into the device. It is given by [5]:

$$\eta_\phi = \gamma\eta_r\Phi_f \tag{2.7}$$

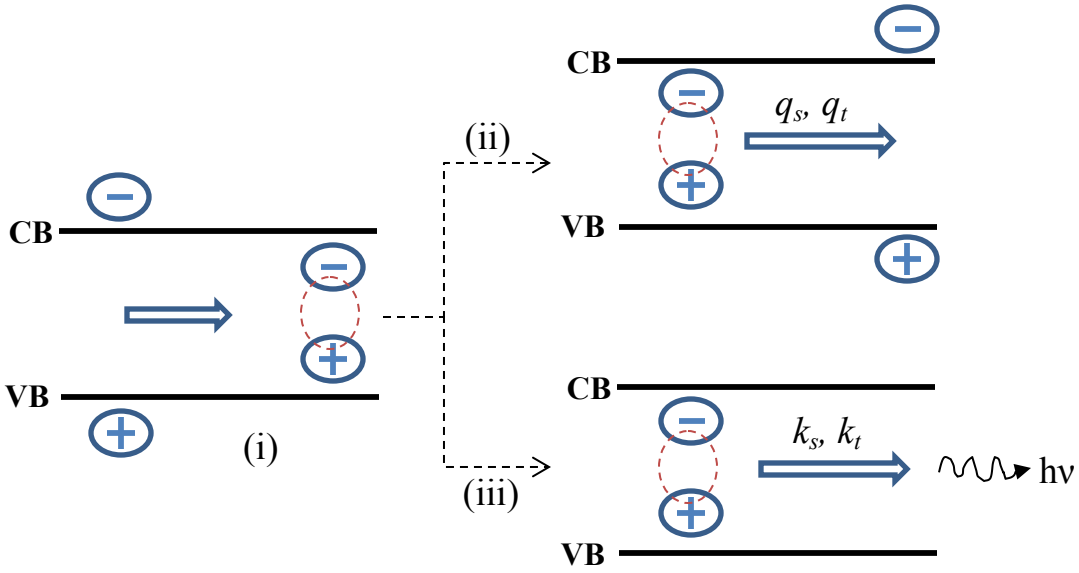

Figure 2.11: *Schematic illustration of the process of (i) formation of intermediate electron-hole pairs and then the subsequent, (ii) dissociation or (iii) recombination. q_s and q_t are the dissociation rates of singlet and triplet respectively; k_s and k_t are respectively the recombination rates of singlet and triplet; image adapted from Ref [12]*

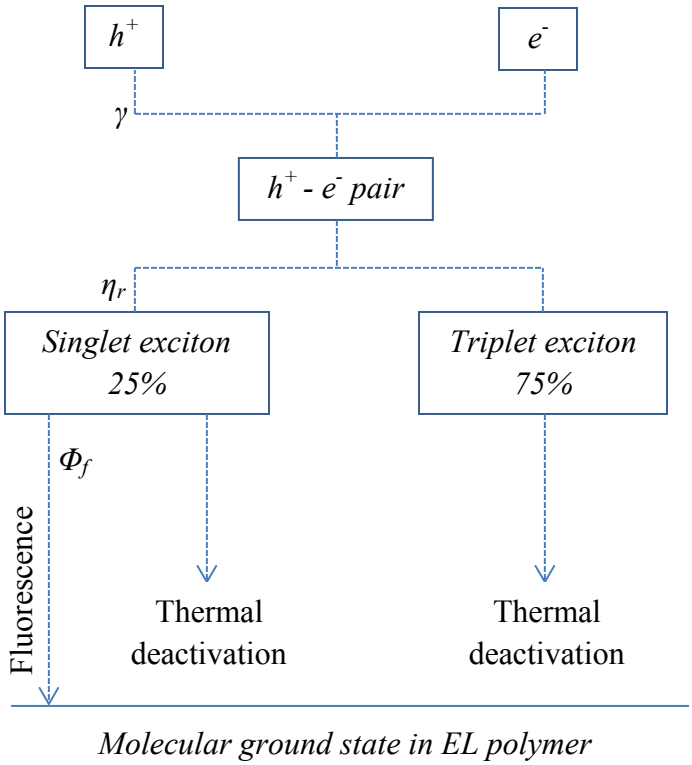

Figure 2.12: *Schematic representation of the elementary processes for charge carrier recombination*

where γ is the charge balance factor, η_r is the efficiency for production of singlet excitons and Φ_f is the quantum efficiency of fluorescence.

For bipolar devices, in the absence of traps, the current flow through the device can be represented as Figure 2.13. The charge balance factor γ is defined by the equation [5]

$$\gamma = \frac{J_r}{J} \quad \text{with} \quad J = J_p + J_{n'} = J_n + J_{p'} \qquad J_r = J_p - J_{p'} = J_n - J_{n'} \tag{2.8}$$

where J is the current in the circuit, J_r is the recombination current, J_p is the incident hole current, $J_{p'}$ is the hole current after recombination, J_n is the incident electron current and $J_{n'}$ is the electron current after recombination.

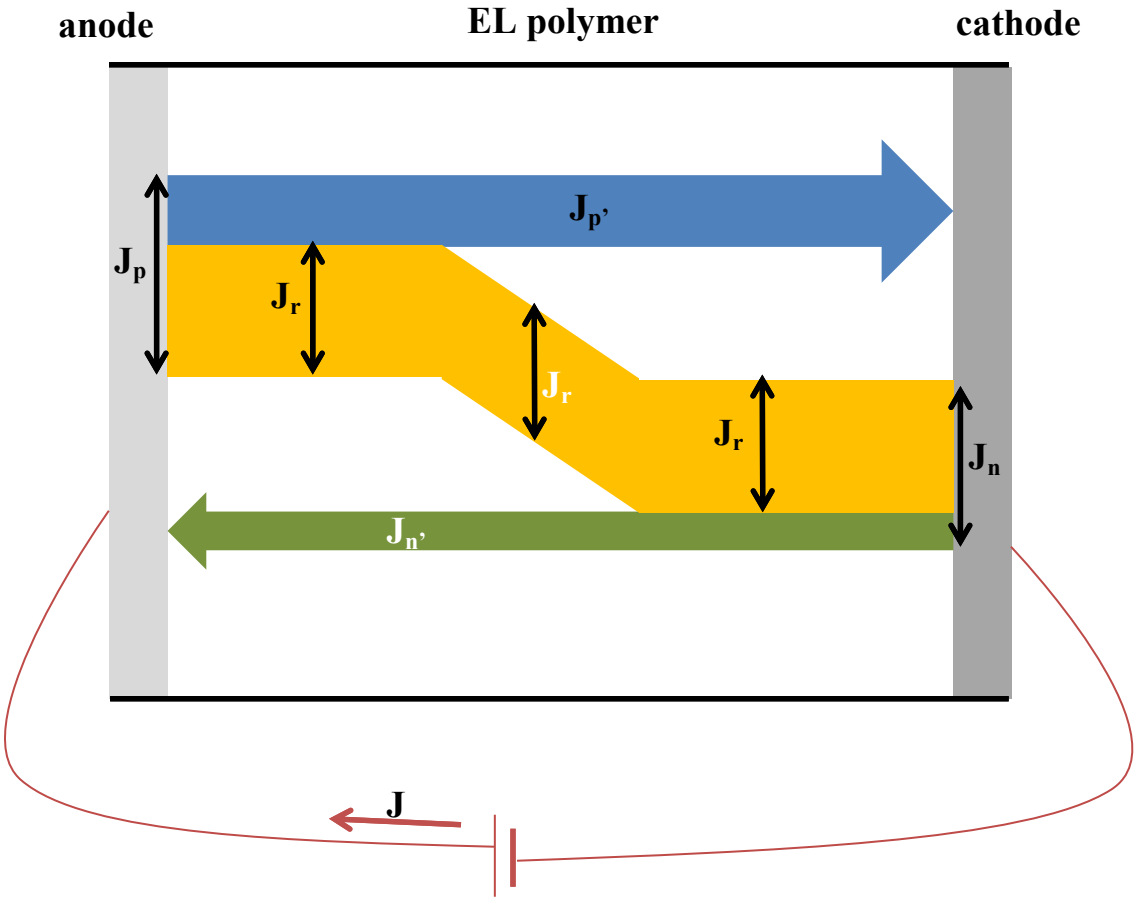

Figure 2.13: *Current flow through an OLED device without trap*

2.1 References

1. W. Helfrich, W. G. Schneider, "Recombination radiation in anthracene crystals," Phys. Rev. Lett. **14**, 229 (1965).

2. C. W. Tang, S. A. VanSlyke, "Organic electroluminescent diode," Appl. Phys. Lett. **51**, 913 (1987).

3. J. H. Burroughes, D. D. C. Bradley, A. R. Brown, R. N. Marks, K. Mackay, R. H. Friend, P. L. Burns, and A. B. Holmes, "Light-emitting diodes based on conjugated polymers," Nature **347**, 539 (1990).

4. Z. Li, H. Meng, "Organic light-emitting materials and devices," Taylor & Francis, (2007).

5. J. Shinar, "Organic light-emitting devices; a survey," AIP PRESS (2004).

6. L. Bozano, S. Carter, "Temperature- and field- dependent electron and hole mobilities in polymer light-emitting diodes," Appl. Phys. Lett. **74**, 1132 (1999).

7. Fujian Wang, "Magnetic and spin effects in organic devices," PhD thesis, University of Utah, (2009).

8. T.D. Nguyen, G. Hukic-Makkosian, F. Wang, L. Wojcik, X.-G. Li, E. Ehrenfreund, Z. V. Vardeny, "Isotope effect in spin response of π-conjugated polymer films and devices," Nat. Mater. **9**, 345 (2010).

9. W. Brutting, "Organic semiconductors," Institute of Physics, University of Augsburg, Germany, (2005).

10. S. M. Sze, Kwok K. Ng, "Physics of semiconductor devices," 3rd edition, Wiley (2007)

11. P. Stallinga, "Electrical characterization of organic electronic materials and devices," Wiley 2009.

12. V. N. Prigodin, J. D. Bergeson, D. M. Lincoln, A. J. Epstein, "Anomalous room temperature magnetoresistance in organic semiconductors," Synth. Met. **156**,757 (2006).

13. M. Kuik, H.T. Nicolai, M. Lenes, G-J.A.H. Wetzelaer, M. Lu, and P.W.M. Blom, "Determination of the trap-assisted recombination strength in polymer light emitting diodes," Appl. Phys. Lett. **98**, 093301 (2011).

CHAPTER 3

ORGANIC MAGNETORESISTANCE (OMAR) MECHANISMS

Recent transport and electroluminescence studies have shown that an external magnetic field can change the current and light output of organic light emitting diodes (OLEDs) with no ferromagnetic electrodes. The phenomenon is commonly referred to as organic magnetoresistance (OMAR); it is quite universal and since its discovery in 2003 [1], it has been observed in many organic diodes based on small molecules [2, 3] and π-conjugated polymers [4, 5, 6]. The organic magnetoresistance can reach sizable value of 20 % in a relatively small field on the order of 10 mT at room temperature. When a device is voltage-biased, the most common parameter used to demonstrate the OMAR is magnetoconductance (MC) defined as:

$$MC = \frac{I(H) - I(0)}{I(0)} \tag{3.1}$$

where $I(H)$ and $I(0)$ stand for the current at magnetic field H the current at zero magnetic field, respectively. A typical result is displayed in Figure. 3.1 [7].

Several mechanisms have been proposed to explain the OMAR, however, none of them can account for the whole body of the experimental observations. The models consider the effect of magnetic field on various electronic and spin-related processes in

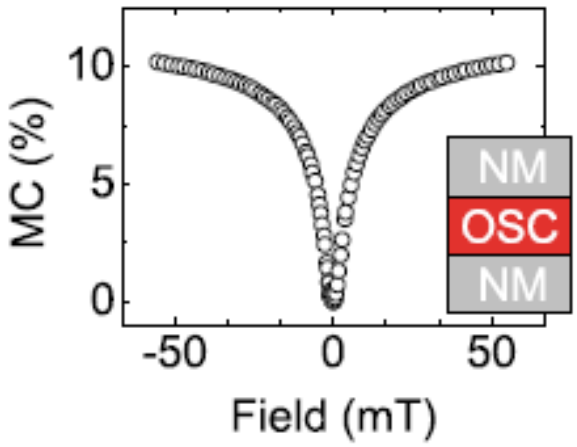

Figure 3.1: *A typical OMAR curve of an ITO/PEDOT-PSS/Alq_3 (100 nm)/LiF/Al measured at room temperature. Magnetoconductance vs. magnetic field. NM stands for nonmagnetic electrodes and OSC for organic semiconductor. From Ref. [7]*

the organic interlayer of the devices, such as bipolaron formation [9], singlet to triplet interconvertion in electrostatically bound electron-hole pairs [9, 10] and detrapping of charges by triplet excitons [12]. Figure 3.2 is an illustration of particle interactions that are considered in different OMAR models [8].

Most of these models are based on the hyperfine interaction (HFI) between the injected spin ½ carriers and nuclear spins in the organic active layer. By replacing protons with deuterons atoms which have a weaker HFI strength, Tho *et al.* proved that the hyperfine interaction indeed plays a central role in OMAR effect [6]. The hyperfine field experience by a carrier result from the interaction between the spin of the carrier and the sum of the surrounding spins from hydrogen nuclei. That results in an extra term in a Hamiltonian given by

$$H_{hf} = \frac{g\mu_B}{\hbar}\vec{B}_{hf,i}\cdot\vec{S}_i \qquad (3.2)$$

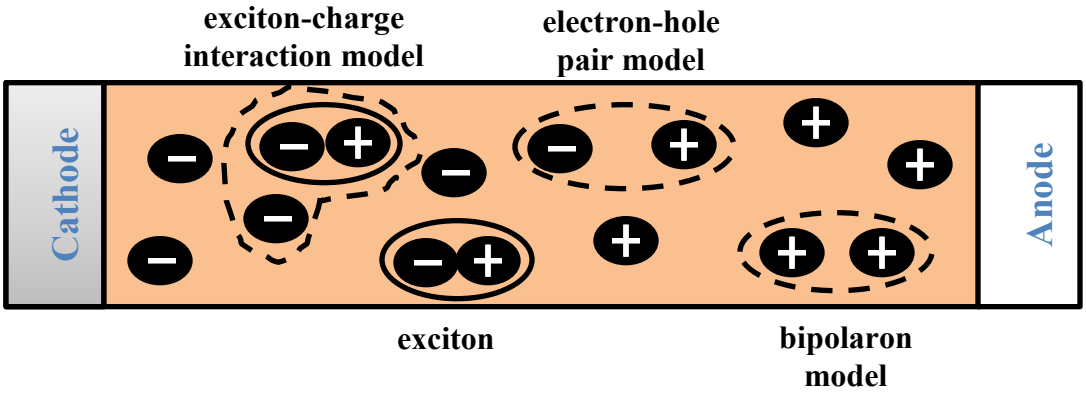

Figure 3.2: *Particles interactions in different OMAR models. Adapted from Ref. [8]*

where $\vec{S}_i$ is the spin operator of the polaron ith, $\vec{B}_{hf,i}$ is the hyperfine field experienced by polaron ith, g is the polaron g-factor (≈2), μ_B is the Bohr magneton and $\hbar$ is the reduced Planck constant.

A typical variation of magnetoconductance, illustrated by Figure 3.1 highlights two important regimes of magnetic field effects: the small-field magnetic field effects (SMFE) with a field in the range of 1 – 10 mT and the large-field magnetic-field effect (LMFE). In SMFE regime, the random hyperfine fields (B_{hf}) induces spin decoherence (Figure 3.3), resulting in the change of singlet (S) and triplet (T) character of carrier pairs [7].

In LMFE region, B_{hf} at each molecular site is too small compared to B_{eff}, which is the sum of the applied external homogeneous magnetic field (B) and (B_{hf}). Hence, the precession of spins on different molecular sites gets more coherent and (S) and (T) characters are preserved for a longer time, resulting in a small change in MC.

Other common features to all OMAR models mentioned above are:

a. The line shape of magnetoconductance (MC) versus magnetic field (H). It was

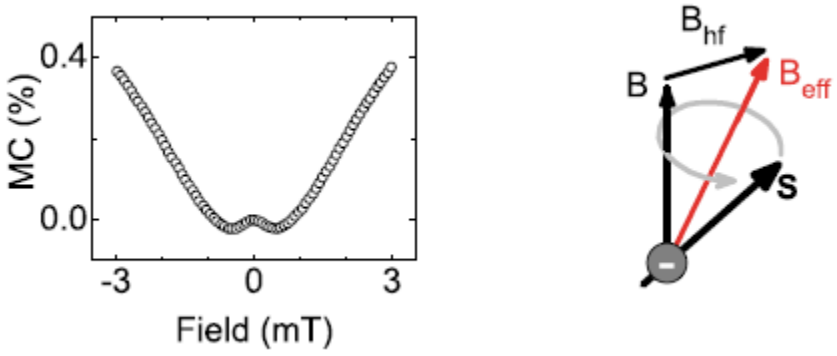

Figure 3.3: *SMFE regime. From Ref. [7]*

shown [18] that *MC* vs. *H* can be fitted with a Lorentzian function

$$MC(H) \propto \frac{B^2}{B_0^2 + B^2} \tag{3.3}$$

or an empirical non-Lorentzian function

$$MC(H) \propto \frac{B^2}{(B_0 + |B|)^2} \tag{3.4}$$

where B_0 denotes the quarter-saturation field. It is generally in the range of 3 mT to 6 mT and is related to the magnitude of hyperfine fields. The main difference between the Lorentzian and non-Lorentzian function is the way they converge to their high field value MC_∞, as illustrated by Figure 3.4 [7].

b. OMAR effect is independent of the direction of the magnetic field

c. OMAR effect is a property of the bulk of a polymer.

The next paragraphs will highlight the difference between the different OMAR models.

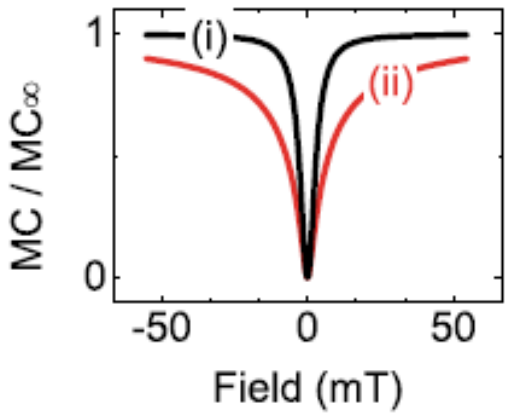

Figure 3.4: *The two different lineshapes used to fit OMAR curves, namely a (i) Lorentzian (ii) or non-Lorentzian. From Ref. [7]*

3.1 Bipolaron model

Due to disordered nature of π-conjugated polymers, the main mode of conduction of charges is hoping of carriers from one localized site to another. The strong electron-phonon coupling makes the energy needed for a doubly-occupied site modest [9]. This doubly-occupied site, named bipolaron, is possible only if the spins of the two carriers are in singlet configuration. The bipolaron formation is not possible when the spins of polaron are in triplet configuration: that leads to the "spin-blocking" [9], which is the basic notion of bipolaron model. Figure 3.5 gives an illustration of the bipolaron model [8].

The effect of the magnetic field on the "spin-blocking" is responsible for the magnetoconductance according to this model. In fact, Wagemans and coworkers explained in Reference [8] how the spin blocking process is lifted. Each polaron in the polymer is subjected to a hyperfine magnetic field due to the presence of all hydrogen nuclei around. The total magnetic field experienced by the spin of a given carrier, $B_{total,i}$,

is therefore the sum of the applied constant magnetic field B and the hyperfine field $B_{hf,i}$ caused by all surrounding nuclei. The total Hamiltonian associated with the magnetic field effect experience by a carrier ith is:

$$H = \frac{g\mu_B}{\hbar}\vec{B}\cdot\vec{S}_i + H_{hf} \tag{3.5}$$

When the applied magnetic field is zero or very small (less than 10 mT), $B_{total,i}$ strongly depend on the magnitude and direction of $B_{hf,i}$. The random orientation of $B_{hf,i}$ on each carrier site will cause the precession of the spin to be randomly altered from site to site (Figure 3.5a). This process is favorable for double-occupancy of a site since the precession may result in the spin adjustment of one carrier with respect to another one; hence increasing the populations of bipolarons at the expense of free carriers to transport the current. A negative MC results from this process.

The sign of the MC can be positive at high magnetic field. In fact, when the applied magnetic field B is large, the randomness introduced previously by the hyperfine field is hindered and the total magnetic field experience by each charge carrier is almost the same (Figure 3.5b). This reduces the probability for spin to lose their polarization and adjust

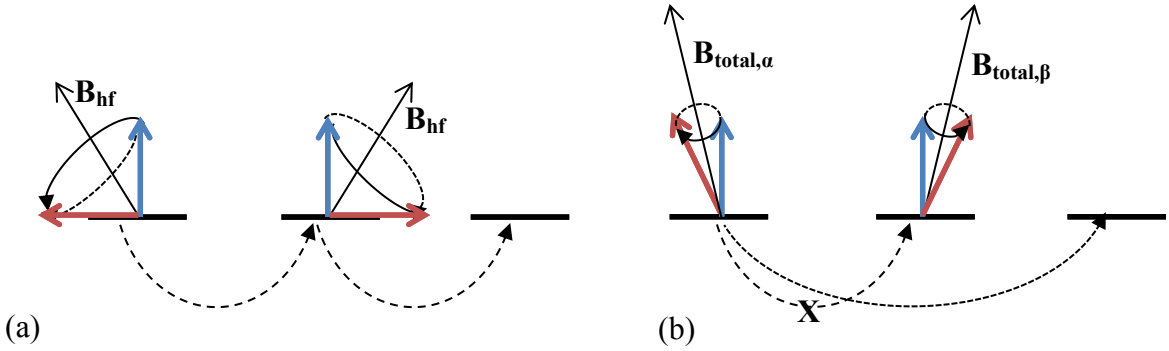

Figure 3.5: *Comparative effect of the magnitudes of the applied magnetic field and the hyperfine field. (a) With $B_{total,i} \approx B_{hf,i}$ the precession turns a parallel configuration into antiparallel, making bipolaron formation possible (b) with $B_{total,i} >> B_{hf}$, polarization of the spin is almost maintained and that which stopped bipolaron formation*

among themselves in parallel and antiparallel configurations to form bipolaron. The main consequence is the increase in hoping towards empty molecular sites and the increase in population of free carriers. The magnetoconductance in this case will be positive.

This shows that, by altering the bipolaron formation rates, the magnetic field changes the current in the device and the sign of the magnetoresistance. All this does not need the charge carriers to be of the opposite signs; hence the bipolaron model seems suitable for explanation of OMAR effect in unipolar devices.

Another important result, based on calculation developed on two-site polaronic model, shows that the increase of the hopping rate leads to a decrease of the magnetoconductance and an increase of the line width of the *MC* vs. *H* (magnetic field) graphs [13].

3.2 Electron-hole pair model

The required element for the use of this model is the presence of positive and negative polarons in the device. The model is based on the different recombination and dissociation rates of singlet and triplet polaron pairs. Prigodin [10] proposed a model of magnetoresistance based on interconversion between singlet and triplet polaron pairs. In this model, negative and positive polarons form a bound pairs in the singlet ($S = 0$, $m = 0$) or triplet ($S = 1$, $m = 0, \pm 1$) spin configuration under effect of electrostatic forces. Without applied magnetic field, singlet polarons and all triplet polarons are degenerate and can be mixed by hyperfine field, resulting in intersystem crossing with a rate m_{ISC} as shown in Figure 3.6.

When an external magnetic is applied, the degeneracy of the triplet pairs is lifted as result of Zeeman effect. Adrian and Monchick [14] show that for electron and hole

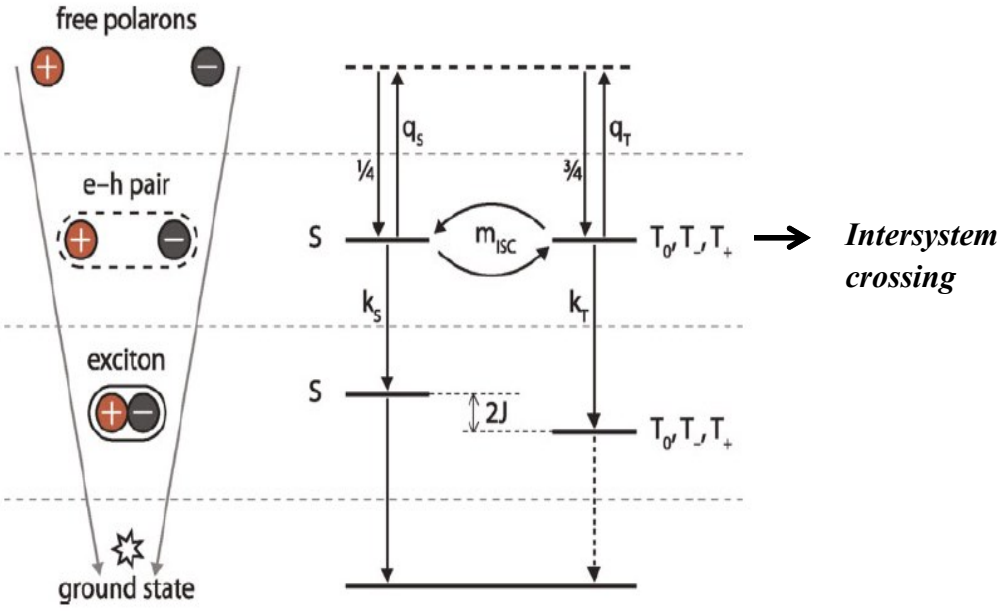

Figure 3.6: *e-h pair formation and intersystem crossing. No external magnetic field applied. q_s and q_t are the dissociation rate of singlet and triplet states, respectively, k_s and k_t are the recombination rate of singlet and triplet states, respectively. From Ref. [8]*

polaron pairs bound by Coulombic interaction and kept at a separation distance greater than the distance required for exciton formation (a distance large enough for the exchange interaction J to be negligible), the mixing will be possible only between the singlet state (S) and triplet state (T_o) . This is illustrated by Figure 3.7.

In this process, the outcome of mixing is the recombination; hence a reduction of the current flow. Therefore, the application of a magnetic field, by reducing the recombination, increases the current flow and leads to a positive magnetoconductance. In other words, this model predicts the growth of the concentration of charge carriers in the device when the magnetic field is applied. The key factors in Prigodin model [10] are the difference between the recombination rate of singlet polaron (k_s) and recombination rate on triplet polaron (k_t) on one hand, and between the dissociation rate of singlet polaron

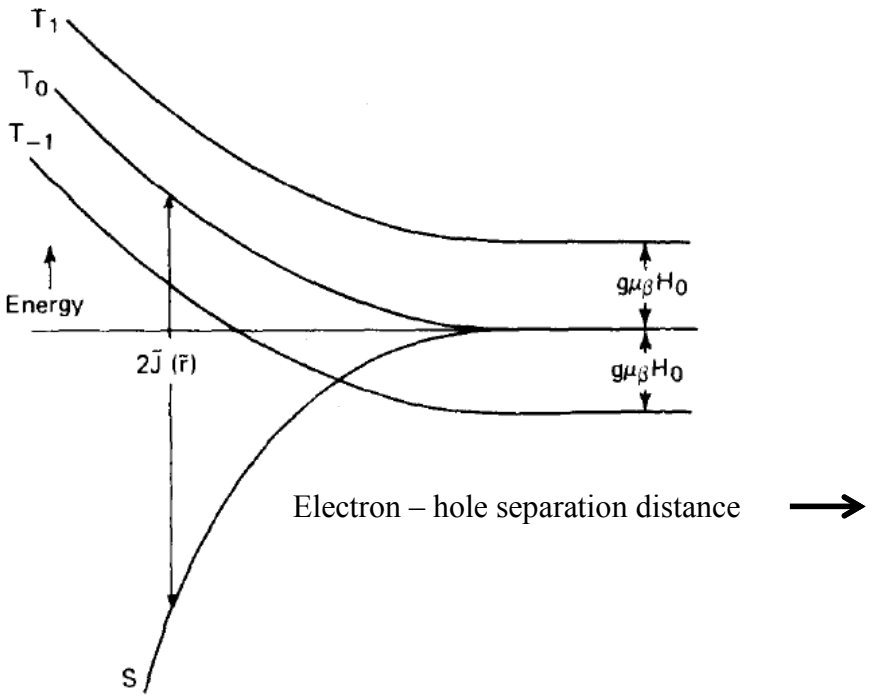

Figure 3.7: *Triplet polaron degeneracy is lifted by external magnetic field. S and T_o are mixed from the point where the exchange effect J(r) is vanished. From Ref [14]*

(q_s) and dissociation rate on triplet polaron (q_t), on the other hand. They assumed that k_s > k_t, and that triplet states mostly contribute to dissociation.

However, in this model which is possible only in the case of bipolar injection of charge carriers, the device is assumed to be in space charged limited regime.

In SCLC regime, the current flowing in the device is giving by [10]:

$$J = \frac{3\varepsilon}{4}\sqrt{\frac{2\pi\mu_n\mu_p(\mu_n+\mu_p)}{\mu_{rec}}}\frac{V^2}{d^3} \tag{3.6}$$

where μ_n and μ_p are the electron and hole mobilities, respectively, μ_{rec} is the recombination mobility, ε is the dielectric constant of the material, V is the applied voltage and d is the thickness of the device.

Assuming only the Langevin recombination and no external magnetic field, Prigodin found that the recombination probability depends on recombination and dissociation rates of singlet and triplet polarons according to equations [10]:

$$\mu_{rec} \propto \left(\frac{1}{4}\right)\frac{k_s}{k_s + q_s} + \left(\frac{3}{4}\right)\frac{k_t}{k_t + q_t} \tag{3.7}$$

With the applied magnetic field and assuming different *g*-factors for electron and hole polarons, the recombination mobility is [10]:

$$\begin{aligned} &\mu_{rec}(0) \propto \frac{k_s + 3k_t}{k_s + 3k_t + q_s + 3q_t} \quad at \;\; H = 0 \\ &and \\ &\mu_{rec}(H) \propto \frac{1}{2}\frac{k_s + k_t}{k_s + k_t + q_s + q_t} + \frac{1}{2}\frac{k_t}{k_t + q_t} \qquad when \;\; H \to \infty \end{aligned} \tag{3.8}$$

The derived magnetoconductance is given by:

$$MC(V,H) = \frac{J(V,H)}{J(V,0)} - 1 = \sqrt{\frac{\mu_{rec}(0)}{\mu_{rec}(H)}} - 1 \tag{3.9}$$

where *MC(V,H)* is the magnetoconductance at applied voltage *V* and applied magnetic field *H, J(V,H)* is the current density at applied voltage *V* and applied magnetic field and *J(V,0)* is the current density at applied voltage *V* and zero applied magnetic field.

From this model, the dependence of the magnetoconductance on the magnetic field and the ratios q/k_s (it is assumed that $q = q_s = q_t$) and k_t/k_s were calculated and presented in Figure 3.8 [13].

The main results predicted by this model are the positive value of the magnetoconductance, the fitting of the *MC* vs. *H* lines with a Lorenztian, the broadening of the line-shape on increasing the ratio of dissociation rate over singlet recombination

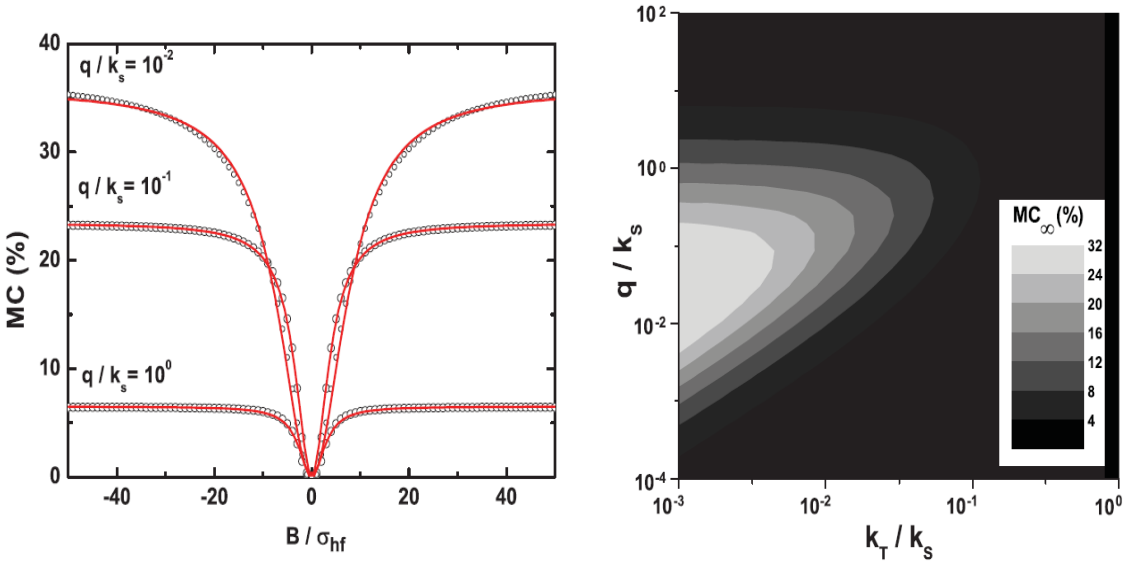

(a) (b)

Figure 3.8: *(a) MC as function of magnetic field and (b) contour plot of the MC as a function of q/k_s and k_t/k_s in the e-h pair model. From Ref. [13]*

rate, the decrease of *MC* when the triplet recombination rate k_t increases irrespective of the ratio q/k_s. No magnetoconductance is predicted by this model when singlet and triplet polarons recombine at the same rate.

3.3 Exciton-charge interaction model

Excitons result from the capture of electron and hole by the same molecule (Figure 3.6). The observation that the efficiency of the OLEDs tends to saturate whilst the magnetoresistance continues to increase suggests that the OMAR effect is not just a consequence of the effect of magnetic field on the recombination. Figure 3.7 shows that at short distances between the carriers, the exchange energy cannot longer be neglected. Hence the mixing of singlet triplet exciton is no longer possible.

The long lifetime of triplet excitons (≈ 25 μs in Alq_3) leads them to be present in the device at a large concentration. Since they are neutral, the triplet excitons will diffuse through the EL layer of the device until they either transfer its energy to a free polaron after recombination or they are quenched the interface. The transfer of energy to a free polaron is called exciton-charge reaction [8].

Ern and Merrifield show that triplets can react with paramagnetic centers such as free carriers in the following manner [12]:

$$T + D_{\pm 1/2} \overset{k_1}{\longleftrightarrow} [T.....D_{\pm 1/2}] \xrightarrow{k_2} D_{\pm 1/2} + S \tag{3.10}$$

where T is triplet exciton, $D_{\pm 1/2}$ is the spin ±1/2 paramagnetic center, S is the singlet ground state of a molecule, k_1 is the rate of formation or backscattering from the pair state and k_2 is dissociation rate of the pair state into a free carrier and a singlet at the ground state.

From equation (3.10), Desai *et al.* [12] noticed that the probability of scattering events increases with the concentration of triplets, oppositely to the mobility of charge carriers. Since an applied magnetic field influences the concentration of triplet excitons, it induces a change in the scattering rate of triplet excitons and free polaron. This change in the scattering rates has effect on the mobility of free polarons, hence on the current. Therefore, the magnetic field changes the *MC* in OLEDs devices through the exciton-charge reaction model. The sign of *MC* depends on the operating conditions of the devices. For example, exciton triplets may detrap trapped electrons and then increase the current in the device or they may act as blocking sites for free carriers moving through the device.

3.4 References

1. J. Kalinowski, M. Cochi, D. Virgili, P.Di Marco, and V. Fattori, "Magnetic field effects on emission and current in Alq3-based electroluminescent diodes," Chem. Phys. Lett. **380**, 710 (2003).

2. J. H. Burroughes, D. D. C. Bradley, A. R. Brown, R. N. Marks, K. Mackay, R. H. Friend, P. L. Burns, and A. B. Holmes, "Light-emitting diodes based on conjugated polymers," *Nature, **347**, 539 (1990).*

3. P. Desai, P. Shakya, T. Kreouzis, and W.P. Gillin, "Magnetoresistance in organic light-emitting diode structures under illumination," Phys. Rev. B, **76**, 235202 (2007).

4. T.L. Francis, O. Mermer, G. Veeraraghavan, and M. Wohlgenannt, "Large magnetoresistance at room temperature in semiconducting polymer sandwich devices," New J. Phys. **6**, 185 (2004).

5. O. Mermer, G. Veeraraghavan, T.L. Francis, Y. Sheng, D.T. Nguyen, M. Wohlgenannt, A. Kohler, M.K. Al-Suti, and M.S. Khan, "Large magnetoresistance in nonmagnetic π-conjugated semiconductor thin film devices," Phys. Rev. B **72**, 205202 (2005).

6. T. D. Nguyen, G. Hukic-Makkosian, F. Wang, L. Wojcik, X.-G. Li, E. Ehrenfreund, Z. V. Vardeny, "Isotope effect in spin response of π-conjugated polymer films and devices," Nat. Mater. **9**, 345 (2010).

7. W. Wagemans, P. Janssen, A.J. Schellekens, F.L. Bloom, P.A. Bobbert and B. Koopmans, "The many faces of organic magnetoresistance," SPIN **1**, 93 (2011)**.**

8. W. Wagemans, B. Koopmans, "Spin transport and magnetoresistance in organic semiconductors," PSSB **248,** 1029 (2011).

9. P.A. Bobbert, T.D. Nguyen, F.W.A. van Oost, B. Koopmans, and M. Wohlgenannt, "Bipolaron mechanism for organic magnetoresistance," Phys. Rev. Lett. **99**, 216801 (2007).

10. V. N. Prigodin, J. D. Bergeson, D. M. Lincoln, A. J. Epstein, "Anomalous room temperature magnetoresistance in organic semiconductors," Synth. Met. **156**,757 (2006).

11. J.D. Bergerson, V.N. Prigodin, D.M. Lincoln, and A.J. Epstein, "Inversion of magnetoresistance in organic semiconductors," Phys. Rev. Lett. 100, 067201 (2008).

12. P. Desai, P. Shakya, T. Kreouzis, and W. P. Gillin, "Magnetoresistance and efficiency measurements of Alq_3-based OLEDs," Phys. Rev. B 75, 094423 (2007).

13. A.J. Schellekens, W. Wagemans, S.P. Kersten, P.A. Bobberet, and B. Koopmans, "Microscopic modeling of magnetic-field effects on charge transport in organic semiconductors," Phys. Rev. B. 84, 075204 (2011).

14. F.J. Adrian, L. Monchick, "Theory of chemically induced magnetic polarization. Effects of S–T±1 mixing in strong magnetic fields," J. Chem. Phys. **71,** 2600 (1979).

CHAPTER 4

EXPERIMENTAL METHODS

4.1 Sample preparation

The studied samples had the multilayer structures of ITO / PEDOT-PSS / MEH-PPV / Ca / Al, ITO / PEDOT-PSS / DOO-PPV / Ca / Al, ITO / MEH-PPV / Ca / Al, and ITO / PEDOT-PSS / MEH-PPV / Au. Samples were made on square glass substrates with side 12.5 *mm*, covered with indium tin oxide (ITO). The ITO anode, a rectangle band of 1 *mm* $\times$ 12.5 *mm*, was obtained after covering a rectangular area of that size with nail polish and then dipping the substrate into HCl solution of concentration 80% for 15 minutes. The substrates are then ultrasonically cleaned in the following steps: two successive baths of 10 minutes each in acetone, two successive baths of 10 minutes in micro-90 cleaning soap and deionized water, two successive rinsing of 10 minutes each in deionized water and two successive baths of 10 minutes each in methanol. The cleaned samples were then stored into propanol.

On the dry sample, a layer of poly [3,4-ethylene dioxy-2,4-thiophene)-polystyrene sulfonate] (PEDOT-PSS) was first spin-coated in ambient condition, and then baked for 30 minutes at 100^{o}C in nitrogen atmosphere in a glove-box with residua 1*ppm* O_2. The following steps were completed in the glove-box without any exposure to ambient conditions: (i) the electroluminescent layer poly[2-methoxy-5-(2'-ethyl)-hexoxy-1,4-

phenylenevinylene] (MEH-PPV) or poly[2,5-dioctyloxy-1,4-phenylenevinylene] (DOO-PPV) was spin-coated; (ii) the structure obtained was placed in the thermal evaporator for successive depositions of 20 *nm* of calcium (Ca) and 80 *nm* of aluminum (Al) at $2\times10^{-6}\,Torr$ vacuum pressure. The thickness of the MEH-PPV varied from 50 *nm* to 150 *nm* and that of DOO-PPV was 50 *nm*. Ca and Al were deposited perpendicularly to the ITO anode through a shadow mask. The last step was the encapsulation of the device with a glass piece which was glued on top of the Al layer via UV adhesive and UV light exposure for 1 minute, at a distance $1\,cm$ from the sample. The OLEDs fabricated were of rectangular cross-section of area $\approx 1\,mm\times 1\,mm$. The complete samples were removed from the glove-box and were stored under vacuum before measurements.

All measurements were performed at room temperature and at atmospheric pressure. The measurements made on the sample can be characterized by the applied voltage across the device, i.e., DC measurements when the driving voltage is of DC type and AC measurements when a small AC excitation is added to a chosen DC bias. Figure 4.1 shows the position of the sample and the home-made measurement system. In that figure, the magnetic field was applied only when it was needed.

4.2 DC measurements

The first measurement made for any sample was the measurement of the current (*I*) vs. the DC bias voltage (*V*), i.e., the *I-V* characteristics of the sample. For this purpose, a DC bias voltage was sent to the ITO anode of the sample and measured with a KEITHLEY 2000 multimeter. The current through the sample is converted to a voltage by an operational amplifier OP1 whose feedback is chosen to allow the maximum current

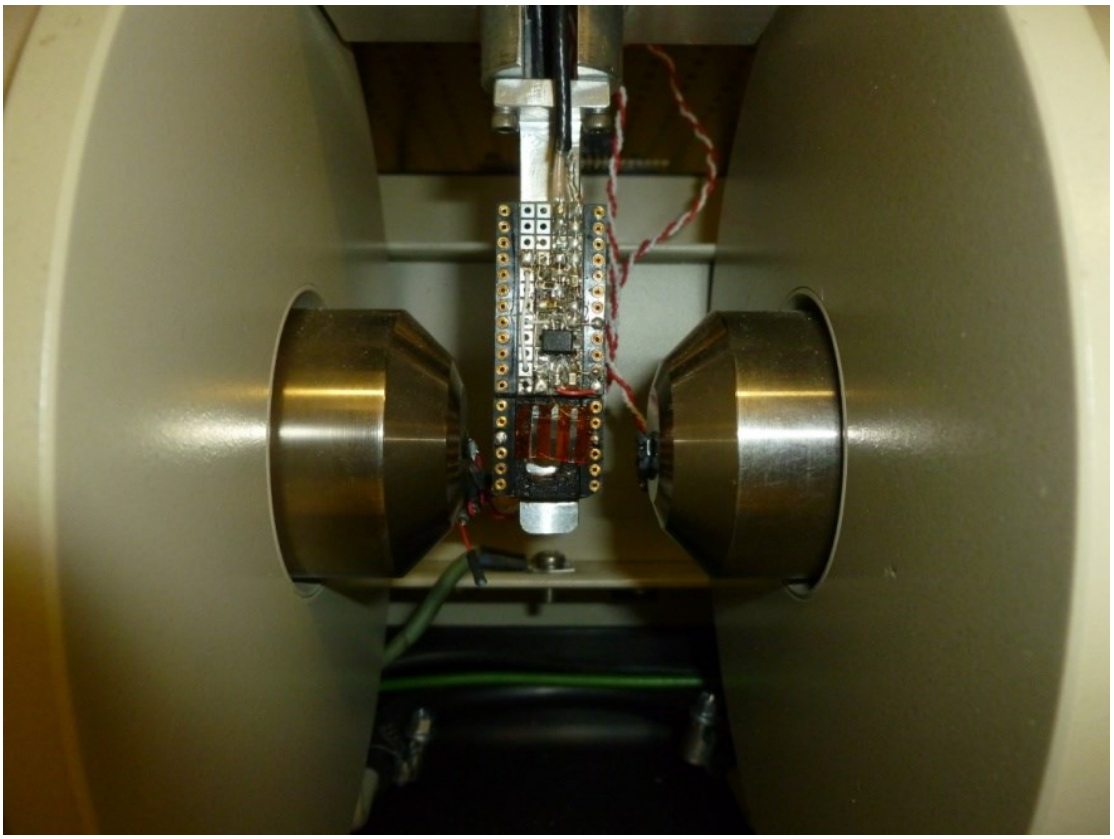

Figure 4.1: *Position of the sample and the home-made measurement system for all experiments*

to go through the device. The same feedback was used for the all set of measurements that were made on the sample.

The amplified output voltage is measured by another KEITHLEY 2000 multimeter and converted into current. Figure 4.2 shows the circuit used for the measurements of *I-V* characteristics.

In another set of experiments, we measured the current as a function of magnetic field (varied in the range -30 *mT* to +30 *mT*) at several selected bias voltages. The curve of *MI* vs *H* was then fitted with a Lorentzian or non-Lorentzian function.

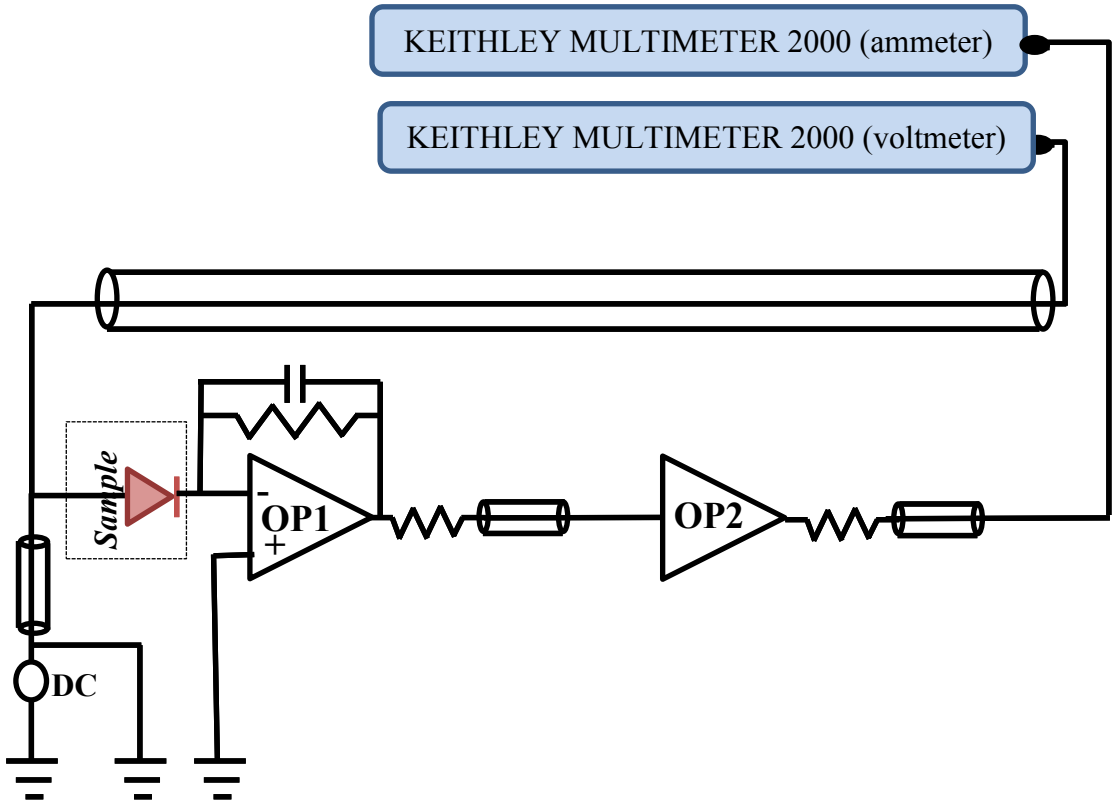

Figure 4.2: *Sample connection for I-V measurements*

4.3 AC measurements: admittance spectroscopy

The setup for admittance measurements is shown in Figure 4.3. The goal of admittance spectroscopy (AS) is to provide characterization of the device components (electronically conducting electrodes + interfaces + polymer) from the device electrical response on a small ac signal superimposed on a dc component, as shown in Figure 4.4.

Macdonald [1] defined ac admittance spectroscopy as the small-signal measurement of the linear electrical response of a material of interest (including electrodes) and the

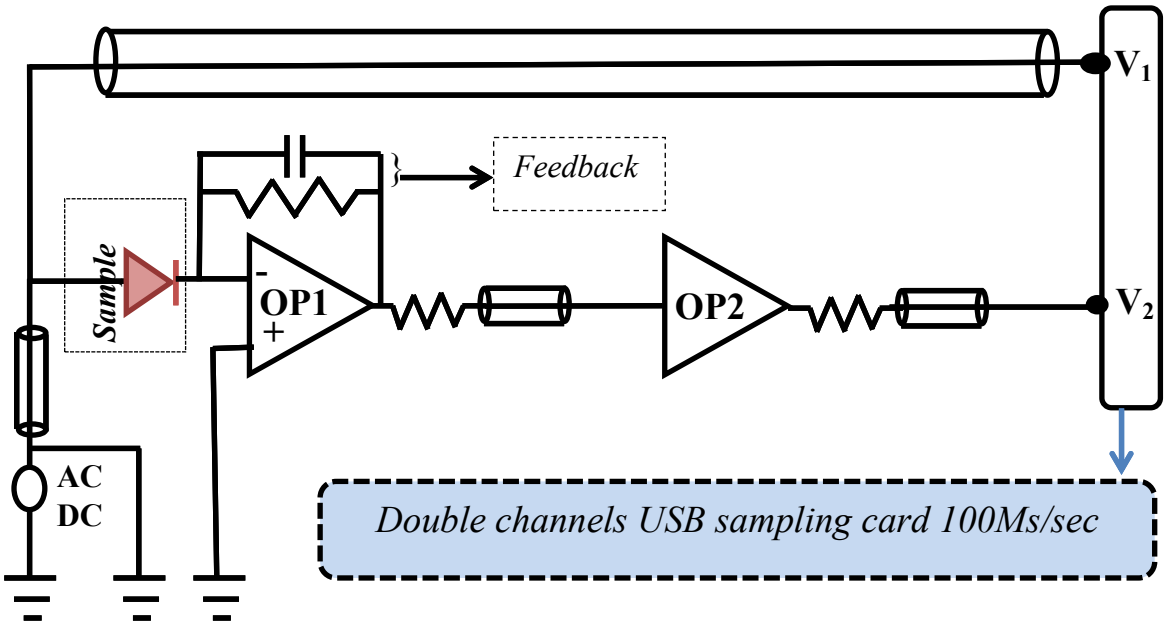

Figure 4.3: *Admittance measurements setup*

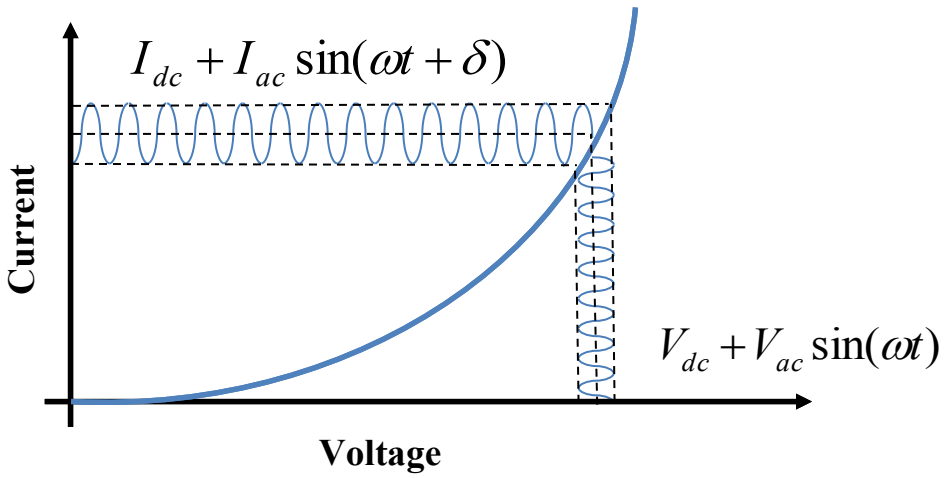

Figure 4.4: *Measurement of AC admittance by application of a small AC signal added to a DC bias. The response is a DC current and a phase-shifted AC current. Adapted from Ref. [2]*

subsequent analysis of the response to yield useful information about the physicochemical properties of the system. In the measurements perspectives, admittance is the derivative of the current versus the voltage:

$$Y = \frac{dI}{dV} \tag{4.1}$$

In general, it is preferable to choose the amplitude of the ac signal lower than the thermal voltage V_T defined as [3]:

$$V_T = \frac{kT}{e} \tag{4.2}$$

where k is the Boltzmann's constant, T is the temperature and e is the charge of electron. At room temperature, V_T is approximately 25 mV. This small amplitude excitation ensures the response signal to be of the same frequency as the incident signal.

In this work, AS was performed by applying a single-frequency voltage superimposed to a chosen dc voltage to the device and measuring the complex gain of the operation amplifier T_s. The corresponding admittance of the sample was then obtained by comparing the real device data with a calibration sample. All the calibration samples used were combinations of resistor and capacitors in parallel, their values being chosen to mimic the real sample parameters. Quantitatively, the total admittance Y_T (the admittance of the polymer diode and the electrodes of resistances R_1 and R_2, as shown in Figure 4.5) is related to the feedback of the operational amplifier admittance Y_f as:

$$Y_T = T_s \times Y_f \tag{4.3}$$

where Y_f is related to the calibration sample's admittance Y_c.

The real admittance of the polymer Y_S is then given by:

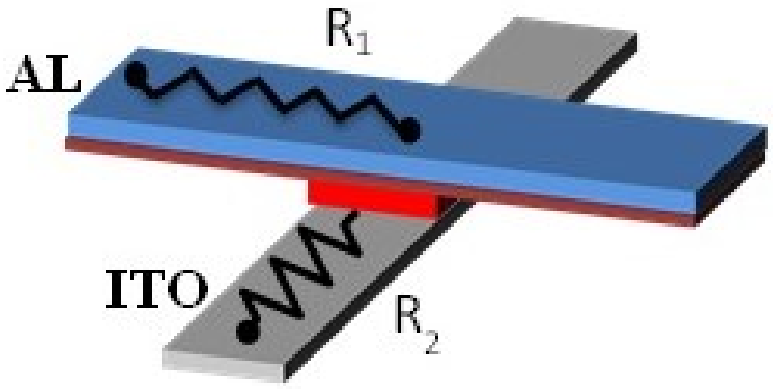

Figure 4.5: *Example of the device with contact points for electrical connection*

$$Y_S = \frac{Y_T}{1 - Y_T(R_1 + R_2)} \tag{4.4}$$

The differential capacitance, which is obtained from the complex admittance of the device, can be used to characterize carrier mobility, rate of trap-mediated and bimolecular recombination processes, and relaxation time of permanent dipoles.

To improve the accuracy of the admittance spectroscopy in our home made measurement system shown in Figure 4.3, the front operational amplifier OP1 was positioned just at about 1 *cm* from the OLED. This minimizes the parasitic capacitance of connecting wires that would have had an impact on the results if a commercial system was used instead. The only input capacitance that limits the performance is that of the FET operational amplifier OP1 itself (≈ 5 – 10 *pF*). The system was calibrated and extensively tested, as shown in Figure 4.7. These figures show the real and imaginary parts of the admittance of some known samples (Figure 4.6), made of resistance R = 500 *kΩ* in parallel with C = 100 *pF* capacitor, and in series resistance r. The values of r were 10 *Ω*, 50 *Ω*, 100 *Ω*, 250 *Ω*, 500 *Ω* and 1 *kΩ*.

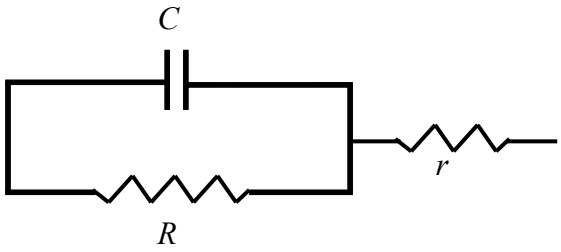

Figure 4.6: *Calibration sample*

The light-blue lines represent the theoretical admittance for each of the measured combination and the bold color show the measured value from the calibration sample. The perfect agreement between the measured and the calculated data proved that the system was suitable to carry admittance measurements. The calibrations were done at zero dc bias voltage and an excitation of amplitude 20 mV.

The admittance spectroscopy study was carried out in the frequency range 1 Hz – 10 MHz, a limit set by the sampling hardware. The magnetic field applied varied from 0 mT to 180 mT. For the OMAR effect experiment, at a given frequency, the admittance was measured for different magnetic fields before moving to another frequency value. This method prevents the data to be changed by the drift in the device due to the high current flowing through.

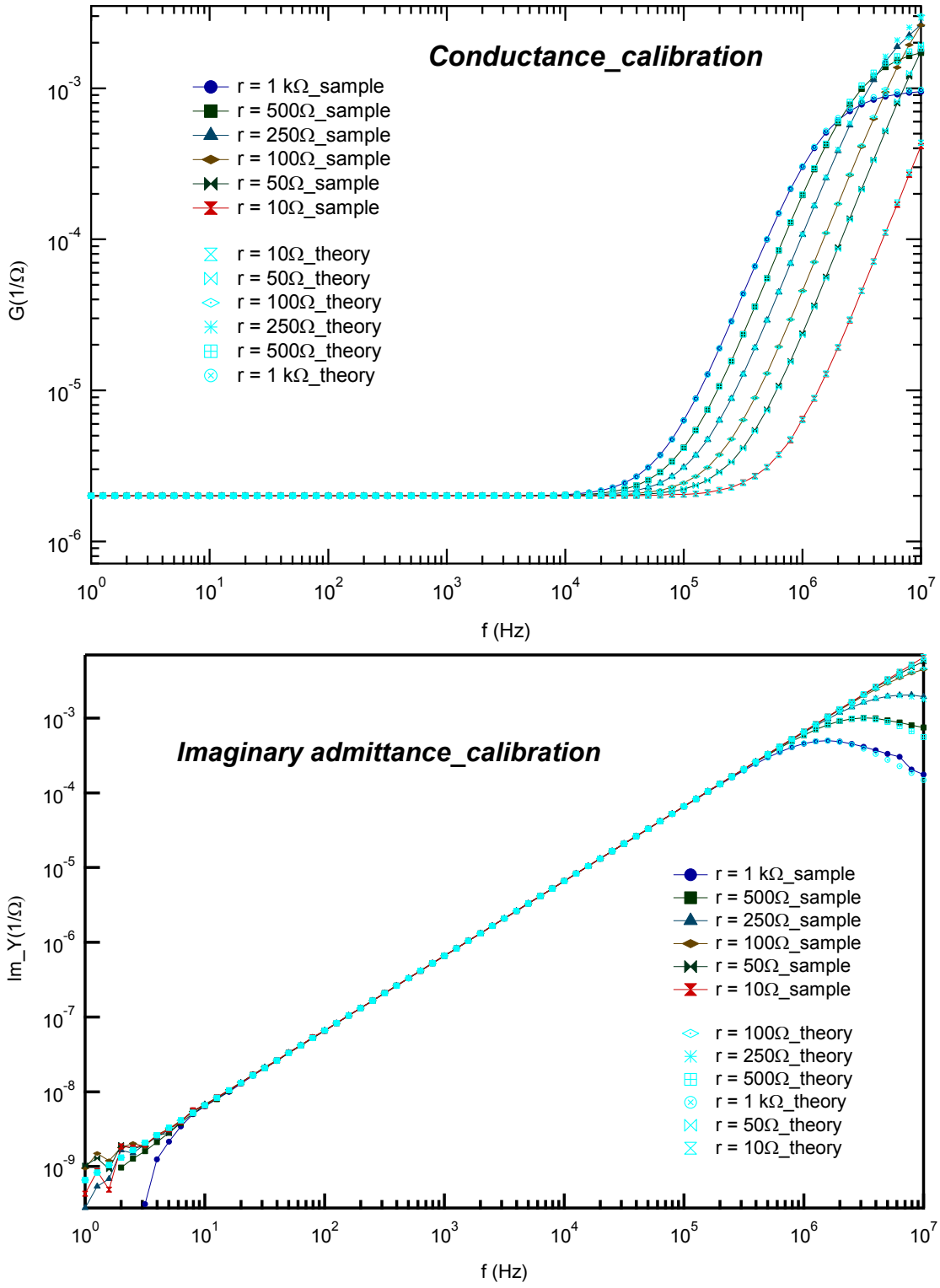

Figure 4.7: *Real and imaginary parts of the calibration sample in bold color. The light-blue shows the theoretical values*

4.4 References

1. J.R. macdonald, “Impedance spectroscopy”, Annals of Biom. Eng. **20,** 289 (1992).

2. P. Stallinga, “Electrical characterization of organic electronic materials and devices”, Wiley 2009.

3. E. Barsoukov, E. MacDonald, J. Ross, “Impedance spectroscopy: theory, experiment, and applications”, 2nd edition, Wiley (2005).

CHAPTER 5

DC MEASUREMENTS: RESULTS AND ANALYSIS

In this chapter, we present the results obtained from DC measurements, i.e., *I-V* characteristics without magnetic field, and magnetocurrent in magnetic fields in the range from -70 *mT* and 70 *mT*.

All the measurements were carried out at ambient conditions. The exposure to oxygen, accompanied by the effect of the electric current applied to the samples, lead to the degradation of the devices with time. However, the glass slide seal on top of the aluminum electrode provides good protection against oxygen, making the samples suitable for measurements for several days. A total of 27 samples were measured, from which the results of 9 are presented in this thesis (Table 5.1). The behavior observed in these 9 samples was typical for the other samples.

5.1 Theory of current injection into solids

The theory for current injection into insulators or semiconductors was developed in 1940 by Mott and Gurney. The current flowing into unipolar or bipolar device is mainly originating from the carriers injected into the polymer from electrodes: holes are injected from the anode and electrons are injected from the cathode. According to A. Rose [1], the

Table 5.1: *Physical description of the devices measured*

Device label	Type	EL polymer	Hole buffer layer	Thickness L (nm)
A	bipolar	MEH-PPV	PEDOT-PSS	80 nm
B	bipolar	MEH-PPV	PEDOT-PSS	150 nm
C	bipolar	MEH-PPV	PEDOT-PSS	150 nm
D	bipolar	MEH-PPV	PEDOT-PSS	150 nm
E	unipolar	MEH-PPV	PEDOT-PSS	150 nm
F	bipolar	MEH-PPV	PEDOT-PSS	160 nm
G	bipolar	MEH-PPV	PEDOT-PSS	50 nm
H	bipolar	DOO-PPV	PEDOT-PSS	50 nm
I	bipolar	MEH-PPV	None	150 nm

charge of electrons Q forced into an insulator or a semiconductor is distributed into free charge carriers in the conduction band and trapped charges in the trap states located in the bandgap of the material. Then, the magnitude of current flowing into a polymer OLED is determined by the charge injection, the charge transport and the recombination mechanism. When the rate of injection of electrons to the conduction band or of hole to the valence band will exceed the recombination rate, the injected carriers get accumulated in the material and form a space charge to limit the injection of additional carriers. Hence, the space charge limit current (SCLC) is bulk limited.

In molecular organic crystals, the forbidden energy gap is large and these materials are strongly disordered. Hence the carrier mobility is low so that the intrinsic resistivity of these materials is high. Thus, SCLC is easily observed in these materials. As there are no perfect crystal, traps created by all types of imperfections are always present in the crystal and interact with injected carriers from contacts, thus controlling the carrier flow

and determining the current density (J) vs. the voltage (V) characteristics [2]. K.C. Kao and W. Hwang [2] reported two types of carrier trap distributions in organic crystals: the traps confined in discrete energy levels in the forbidden energy gap and the traps with a quasicontinuous distribution of energy levels (exponential or Gaussian distribution) having a maximum trap density near the band edge.

Our samples are either unipolar or bipolar. The theory divides the carrier injection into solid in two classes:

- single-carrier injection into unipolar samples. It is predicted that the injected carriers would gradually establish a space charge leading to the well known single carrier SCLC
- double-carrier injection into bipolar devices. In this case, all the electrical properties are controlled by the recombination processes, which may be monomolecular if recombination occurs through one or more sets of localized recombination centers, or bimolecular if it is a direct hole – electron recombination.

5.1.1 Single-carrier injection

Let us consider the case where holes are the only carriers injected in the semiconductor. At a bias voltage V across a device of thickness L in the direction of current flow, the current density is

$$J = qp(x)\mu_p(F(x))F(x) \tag{5.1}$$

where q is the unit charge of the carrier, μ_p is the hole mobility, $F(x)$ is the electric field inside the device as function of the position x, $0 < x < L$.

At low applied voltage, the density of thermally generated free carriers, p_0, inside the material is greater that the density of injected carriers and the field inside the device is

uniform. If we assume a field-independent mobility, the ohmic current density is given by:

$$J = qp_0\mu_p \frac{V}{L} \tag{5.2}$$

At bias voltage high enough to impose a drift in the device, we can assume that the total density of carriers in the device is $p(x) + p_t(x)$ where $p(x)$ represents the density of injected free carriers and $p_t(x)$ is the density of trapped carriers. The electric field satisfies the Poisson's equation

$$\frac{dF(x)}{dx} = \frac{q[p(x) + p_t(x)]}{\varepsilon} \tag{5.3}$$

where $p_t(x) = \int_{E_l}^{E_u} h(E,x) f_p(E) dE$ (5.4)

and $p(x) = N_v \exp(-E_{Fp} / kT)$ (5.5)

The function $f_p(E)$ used above is the probability for a trap to capture a hole. It follows the Fermi-Dirac statistics as

$$f_p(E) = \frac{1}{1 + g_p \exp\left(\frac{E_{Fp} - E}{kT}\right)} \tag{5.6}$$

and the function $h(E,x)$ represents the distribution function for the trap density depending in the energy level E above the edge of the valence band and the distance x from the injecting contact

$$h(E,x) = N_t(E)S(x) \tag{5.7}$$

where $N_t(E)$ and $S(x)$ are respectively, the energy and spatial distribution functions of traps.

If we assumed that there is no trap in the device, $p_t(x) = 0$ and using the boundary condition $V = \int_0^L F(x)dx$, the current density is

$$J = \frac{9}{8}\varepsilon\mu_p \frac{V^2}{L^3} \tag{5.8}$$

In case of traps confined in single or multiple discrete energy levels (Figure 5.1) and field independent mobility in the device, the current density is

$$J = \frac{9}{8}\varepsilon\mu_p\theta_a \frac{V^2}{L_{eff}{}^3} \tag{5.9}$$

where θ_a is the ratio of free carrier density to total carrier and L_{eff} is effective thickness due to the inhomogeneous spatial distribution of free and trapped carriers defined respectively by:

$$\theta_a = \frac{p}{p + p_t} \tag{5.10}$$

and

$$L_{eff} = \left\{ \frac{3}{2} \int_0^L \left(\int_0^t [\theta_a + S(x)]dx \right)^{1/2} dt \right\}^{2/3} \tag{5.11}$$

Since in conjugated polymer, the charge transport mechanism is described by hopping in a Gaussian DOS that is broadened due to disorder, we can assumed that the broadening of trap states is also described by a Gaussian distribution, with the space and energy distribution function of trap being [2]

$$h(E,x) = \frac{N_t}{\sqrt{2\pi}\sigma_t} \exp\left[-\frac{(E - E_{tn})^2}{2\sigma_t{}^2} \right] S(x) \tag{5.12}$$

where σ_t is the width of the distribution, E_{tn} is the hole-trapping energy (Figure 5.1 (a)).

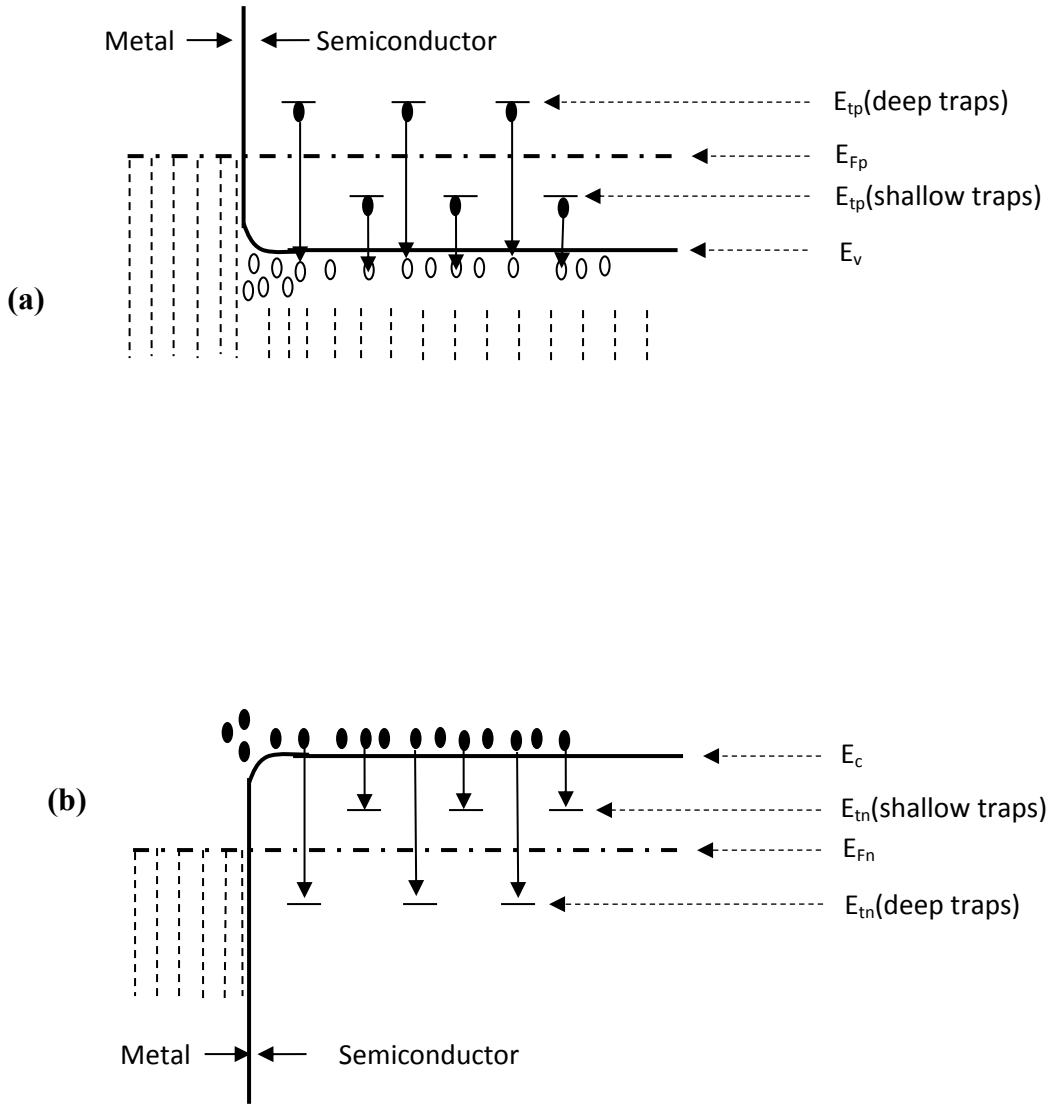

Figure 5.1 *Energy level diagrams for carriers' injection into a semiconductor with shallow and deep traps. (a) holes injecting from a hole ohmic contact, (b) electron injection from electron ohmic contact.*

In the case where the traps energy level is below the quasi-Fermi energy level (shallow traps) for p-type semiconductors, the current density is defined by

$$J = \frac{9}{8}\varepsilon\mu_p\theta_d \frac{V^2}{L_{eff}^{\ 3}} \tag{5.13}$$

where L_{eff} is given by equation (5.11) and the ratio of free carrier density to total carrier θ_d is given by [3]:

$$\theta_d = \frac{N_v}{N_t}\exp\left[-\frac{E_{tn}}{kT}+\frac{1}{2}\left(\frac{\sigma_t}{kT}\right)^2\right] \tag{5.14}$$

When the quasi-Fermi level is below the traps energy level (deep traps for p-type semiconductor), the current density is given by [2]:

$$J = N_v\mu_p q\left(\frac{\varepsilon_0\varepsilon_r}{qN_t}\frac{n-1}{n}\right)^{n-1}\left(\frac{2n-1}{n}\right)^n \frac{V^n}{L_{eff}^{\ 2n-1}} \tag{5.15}$$

where

- ε_0 and ε_r are respectively, the permittivity of free space and the relative permittivity of the material,
- the power n shows the regime of transport occurring in the device and is given by $n = 1+\sqrt{1+\frac{2\pi\sigma_t^{\ 2}}{16k^2T^2}}$ (5.16)
- L_{eff} is the effective thickness of the device. In the approximation $p_t >> p$, it is given by $L_{eff} = \left\{\frac{2n-1}{n}\int_0^L\left[\int_0^t S(x)dx\right]^{(n-1)/n}dt\right\}^{n/(2n-1)}$ (5.17)

5.1.2 Double-carriers injection

When electrons and holes are injected into a semiconductor, a nonequilibrium situation characterized by $np > n_i^2$ is reached, where n and p are the respective electron and hole concentration inside the material and n_i is the intrinsic density of charges. In bipolar OLEDs devices, the carrier density distributions will return to equilibrium through a recombination process of electrons and holes. The traps present in the bandgap of the polymer influence the recombination process by acting sometimes as recombination centers for indirect recombination. Depending on their positions in the bandgap, the traps can be classified either as electron traps when their energy level is close to the bottom of the LUMO band (E_c), or as hole traps when their energy levels are close to the top of valence band (E_v), or as recombination centers when their energy levels are between the demarcation levels for electrons (E_{Dn}) and holes (E_{Dp}) (Figure 5.2). The demarcation level for electron (for hole) is defined as the level at which a captured electron (hole) has equal probabilities of being excited into the conduction band (into the valence band) and of recombining with a hole from the valence band (an electron from the conduction band). It is quantitatively defined with respect to the quasi-Fermi levels as [2]:

$$E_{Dn} - E_{Fn} = E_{Dp} - E_{Fp} = kT \ln\left(\frac{p\sigma_p}{n\sigma_n}\right) \tag{5.18}$$

where σ_n and σ_p are the capture cross sections of electron trapping center and hole trapping center, respectively.

In the case when the mobilities of free holes and free electrons are independent of the electric field, the presence of traps and recombination centers, the behavior of the current

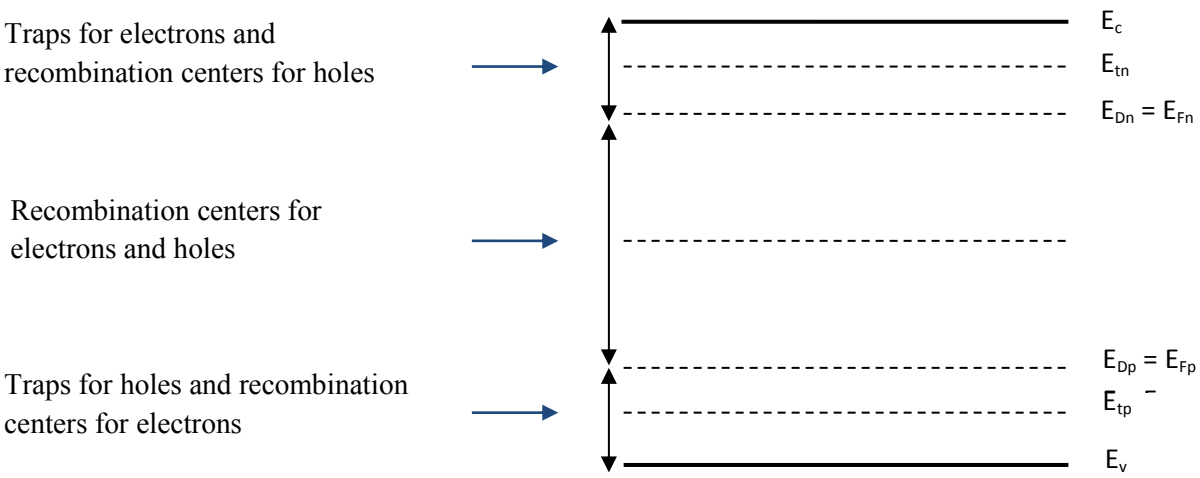

Figure 5.2: *Demarcation levels, Fermi levels, energy levels for trapping and recombination centers for* $n\sigma_n = p\sigma_p$

flowing in the semiconductor (J), which is the sum of electron current (J_n) and the hole current (J_p), is governed by the following equations [2]:

- current flow equations

$$J_n = q\mu_n n\frac{dV}{dx} \tag{5.19}$$

$$J_p = q\mu_p p\frac{dV}{dx} \tag{5.20}$$

$$J = J_n + J_p \tag{5.21}$$

- continuity equations

$$\frac{1}{q}\frac{dJ_n}{dx} = -\frac{1}{q}\frac{dJ_p}{dx} = R \tag{5.22}$$

- Poisson's equation

$$\frac{dE}{dx} = \frac{q}{\varepsilon}\left[p(x) + p_t - (n(x) + n_t)\right] = \frac{\rho}{\varepsilon} \tag{5.23}$$

where x is the direction perpendicular to the electrodes plane located at $x = 0$ and $x = L$, E is the electric field, ρ is the charge density, n, p, n_t and p_t are given by:

$$n = N_c \exp\left(-\frac{E_c - E_{Fn}}{kT}\right) \tag{5.24}$$

$$p = N_v \exp\left(-\frac{E_{Fp} - E_v}{kT}\right) \tag{5.25}$$

$$n_t = \int_{E_l}^{E_u} \frac{h_n(E,x)}{1+\exp\left[(E - E_{Fn})/kT\right]} dE \tag{5.26}$$

$$p_t = \int_{E_l}^{E_u} \frac{h_p(E,x)}{1+\exp\left[(E_{Fp} - E)/kT\right]} dE \tag{5.27}$$

where $h(E,x)$ is the energy and space distribution function for electron and hole traps.

In the case of band-to-band recombination, i.e., recombination with neither traps nor recombination centers, the flowing current is

$$J = \frac{9}{8} \varepsilon \mu_{eff} \frac{V^2}{L^3} \tag{5.28}$$

where μ_{eff} is the effective mobility given by [2]:

- For small recombination cross section σ_R,

$$\mu_{eff} = \frac{4}{3}\sqrt{\frac{\pi q \mu_n \mu_p (\mu_n + \mu_p)}{\varepsilon \langle v \sigma_R \rangle}} \tag{5.29}$$

  where v is the microscopic relative velocity of an electron and hole.

- For very large recombination cross section σ_R, there is no region where electrons and holes can overlap since there would be an infinite recombination current. Then, the electron current will exist only on the cathode side and the hole current on the anode side, and they will meet and

annihilate at a certain plane dividing the bulk into these two regions that correspond to two space-charge-limited currents:

$$\mu_{eff} = \mu_n + \mu_p \tag{5.30}$$

When the traps' energy level are Gaussianly distributed and the recombination mobility $\langle v\sigma_R \rangle$ is large as it is in the case for polymers [2], the flowing current is given by equation (5.28), where $\mu_{eff} = \theta_n \mu_n + \theta_p \mu_p$. The parameters θ_n and θ_p here are the ratios of free electron density to total electron injected and free hole density to total holes injected into the semiconductor.

In the case where recombination centers and traps are present, Schwob and Zschokke-Granacher have derived a simple expression for double injection J – V characteristics by dividing the crystal specimen into three regions: (a) hole injection region ($p >> n$ and n can be neglected), (b) space charge free region (traps are emptied by recombination and the thickness of this region is proportional to the applied voltage), and (c) electron injection region ($n >> p$ and the thickness of this region is much smaller than the specimen thickness) [2]. They obtained:

$$J = A\left(\frac{V_A}{V_A - V}\right)^{n-1} \frac{V^n}{L^{2n-1}} \tag{5.31}$$

where A is a function of trap parameters and physical parameters of the crystal, V_A is given by

$$V_A = \frac{L^2}{\mu_n \tau_n (\Delta \ln n)} \tag{5.32}$$

with $\Delta \ln n$ being the difference in value of $ln\ n$ between the boundaries of the space charge free regions. Equation (5.31) fitted the experimental results for anthracene crystals

with the value of n between 3 and 4 for low injection levels and with $n > 6$ for higher injection [2].

5.2 Results and analysis

5.2.1 I - V characteristics

Figures 5.3 (a), (b) and (c) display the current density vs. voltage graphs for MEH-PPV devices of thickness 150 *nm*, but in three different configurations.

The experimental data are modeled using the equation

$$I \propto V^n \tag{5.33}$$

where the exponent n determines the transport regime at a given bias voltage. It can be calculated from experimental data as

$$n = \frac{dLn(I)}{dLn(V)} \tag{5.34}$$

The exponent n is plotted on the right axis of Figures 5.3 (a), (b) and (c).

Comparing devices B and E, which differ by the work functions of their electrodes, it can be observed that the transport regimes in the devices, as described by n vs V, are really different. From Figure 5.3 (b), we can see that bipolar device B is in the ohmic regime, $n = 1$, when the applied voltage(V_b) is less than 1.5 V. As the voltage increases and exceeds the built-in potential $V_{BI} \approx 2\,V$, the exponent n starts increasing, reaching a constant value, $n \approx 4$ in the interval $2\ V < V_b < 3\ V$. This value of $n > 2$ indicates a space charged limited current (SCLC) in presence of traps.

This trap-mediated SCLC is likely due to electron transport in the device. In SCLC, the current density is given by [3]:

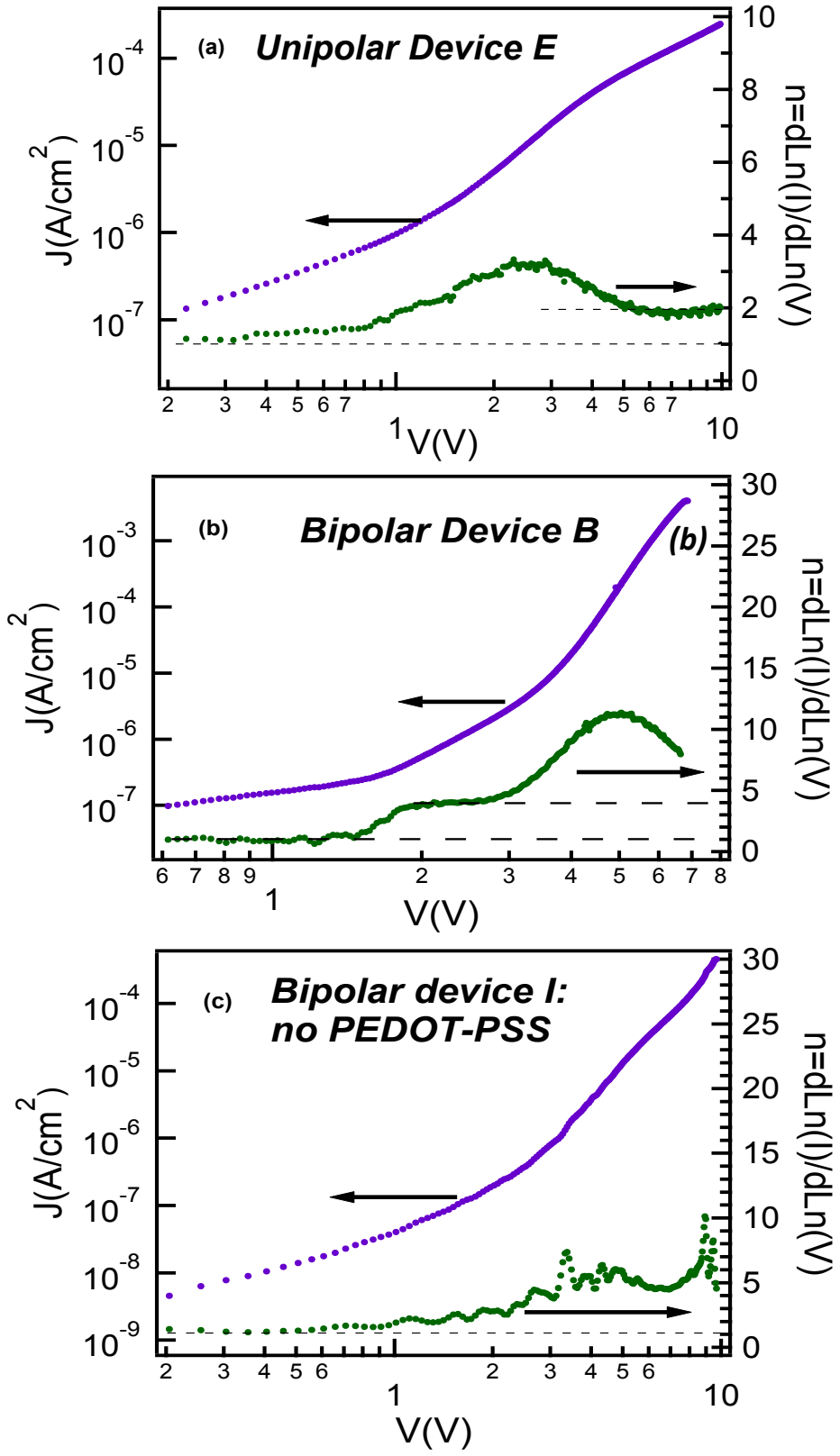

Figure 5.3: *J vs. V (a) unipolar device E; (b) bipolar device B; (c) bipolar device I*

$$J \propto \frac{V^n}{L^{2n-1}} \tag{5.35}$$

where L is the device thickness.

Recent analysis of transport data indicated in the presence of trap states that have a Gaussian distribution, the exponent *n* in equation (5.35) is given by equation (5.16), i.e.,

$$n = 1 + \sqrt{1 + \frac{2\pi\sigma_t^{\,2}}{16k^2T^2}}$$

where σ_t is the width of the distribution, k is the Boltzmann constant and T is the temperature.

For $n \approx 4$ as we found in the range $2V < V_b < 3V$, the value of the width of distribution of trap states is $\sigma_t \approx 0.117eV$; this is closed enough to the value of $\sigma_t = 0.1eV$ obtained by Mandoc *et al.* [3] in their simulation of the trapped carriers density vs. free carrier density with total trap density being equal to $1\times10^{-24}m^{-3}$.

As $V_b > 3\,V$, n increases roughly exponentially with V_b. This is the regime of bipolar injection. In fact, an exponential dependence of the current was recently reported for MEH-PPV based organic light emitting diodes [4]. In the bias voltage range $V_b > 5\,V$, the dependence of *n vs. V* from Figure 5.3 (b) tends to a value of *n* in the range 2 – 3; this is expected at high injection level in the SCLC regime depending on the relative strength of bimolecular or trap mediated recombination processes [2].

For unipolar device E shown in Figure 5.3 (a), three different transport regimes are present:

- at $V_b < 0.7\,V$, $n \approx 1$, this corresponds to an ohmic regime
- at $0.7\,V < V_b < 5\,V$, n is not constant: the sample is in the trap-filling regime

The current increases with the bias up to 3 V, n varying from approximately 1.25 to 3. At 3 V, the maximum value of n is reached and all traps are filled. The additional injected holes will subsequently create a space-charged limit regime. This is shown by the progressive decreasing in the value of n in the bias range from 3 V to 5 V

- at $V_b > 5\,V,\ n = 2$, this corresponds to a SCLC regime due to a unipolar (hole) current. Since the traps are filled, all carriers injected in the EL layer are free. The absence of bipolar injection in this case leads to a fast SCLC. This is a trap-free SCL regime.

The bipolar device I, which differs from device B by an absence of PEDOT-PSS, presents a current density of one order of magnitude less than the one of B. This is expected because PEDOT-PSS is used to facilitate holes injection in the device. The transport regimes are not as distinct as in the previous samples, but the following can be distinguished:

- at $V_b < 0.6\,V,\ n \approx 1$, this corresponds to an ohmic regime
- at $0.6\,V < V_b < 1.7\,V,\ n \approx 2$, this corresponds to a SCLC regime without traps. A similar result was obtained in electron-rich device in [4]
- at $V_b > 1.7\,V$, $n > 2$ and its variation with V_b may be the result of either the absence of a layer to smooth the rough ITO surface and eliminate shorts due to spikes on the ITO surface, or to protect the EL layer from inorganic atoms diffusing from ITO. A strong increase of n with the applied bias is not observed. We may conclude in that bias range, the device is in SCL regime with traps, and up to the highest voltage applied, $10V$, and the device did not reach the regime

where all the traps are filled.

5.2.2 Magnetocurrent

In this section, I describe the effect of the magnetic field on the current and the differential conductance of the device. The results shown here are obtained from measuring device C (ITO/PEDOT-PSS/MEH-PPV/Ca/Al) with 150 *nm* thick MEH-PPV layer. After getting the I vs. V characteristics of device C, the magnetocurrent $MI(B)$ defined by equation (5.36), was measured at several selected V_b values.

$$MI(B) = \frac{I(B) - I(0)}{I(0)} \tag{5.36}$$

For device C, the $MI(H)$ response shown in Figure 5.4 was fitted using the empirical non-Lorentzian equation

$$\frac{\Delta I(B)}{I(0)} = \Delta I_0 \frac{B^2}{(|B|^2 + {B_0}^2)} \tag{5.37}$$

The data show that the magnetocurrent is positive in the full range of magnetic fields applied. This is not in agreement in with bipolaron theory which predicts a negative magnetocurrent in magnetic fields less than 10 *mT*. The different behaviors of the Lorentzian and non-Lorentzian magnetocurrents when they converge to their maximum values were highlighted in Figure 3.4 of Chapter 3. The fitting of our magnetocurrents with the non-Lorentzian is in good agreement with that prediction. But oppositely to Wagemans *et al.* [25] who predicted B_0 to be in the range 3 *mT* – 6 *mT*, the quarter-saturation field for our data was found to be $B_0 = 2.5mT$.

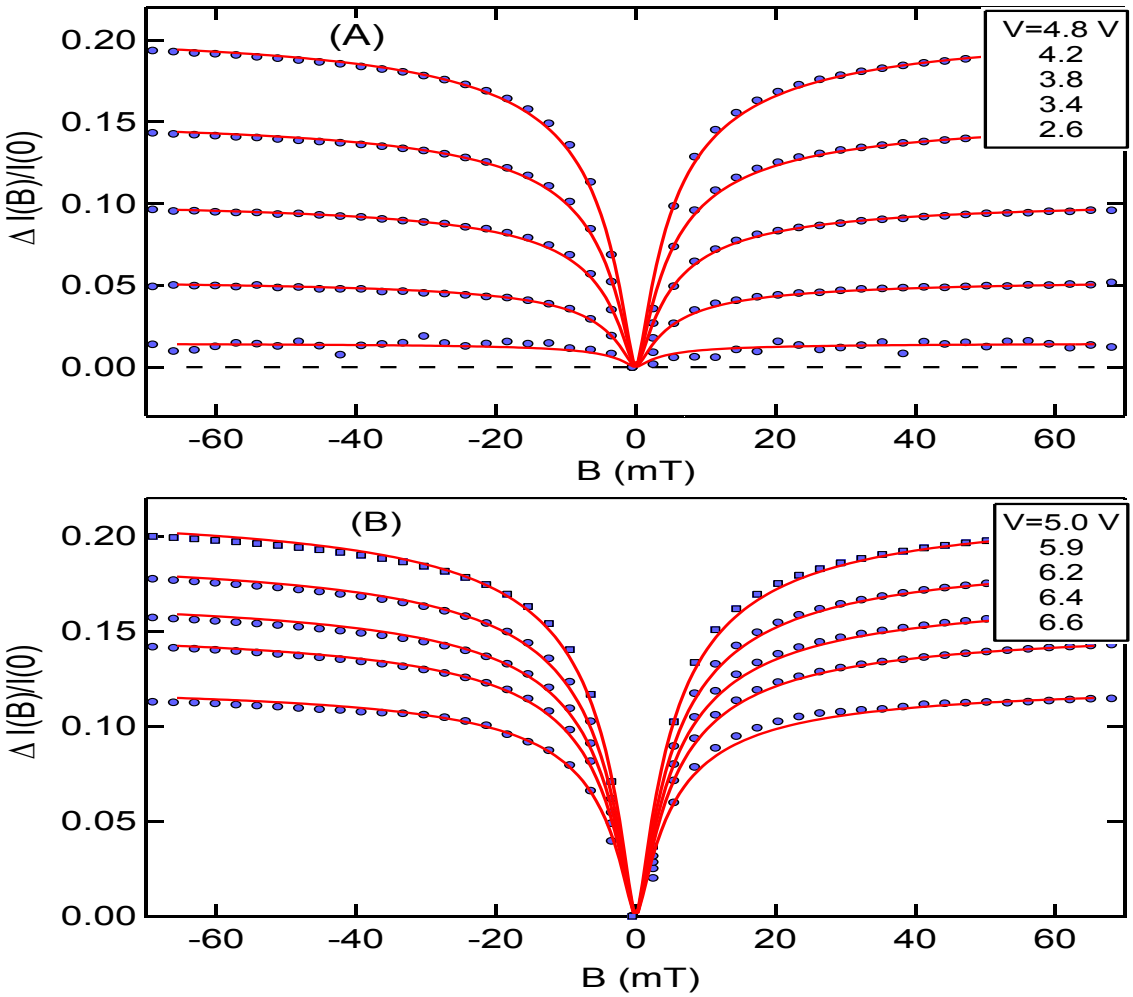

Figure 5.4: *Magnetocurrent MI (B) for bipolar device C at different applied voltage, as function of external magnetic field B*

This result shows that at a given magnetic field B, $MI(B)$ increases with bias voltage (V_b) for V_b in the range 0 V – 5 V, then starts decreasing for V_b > 5 V. We also found that the parameter B_0 increases with the bias voltage as predicted by T.D. Nguyen *et al.* [5].

Similar measurements were performed on the unipolar devices. The effect of the magnetic field was not detected on these devices in the magnetic field varying from -30 mT to 30 mT. This supports the view that the bipolaron model is not appropriate to explain the OMAR in our devices.

5.3 References

1. A. Rose, “Space-charge-limited currents in solids,” Phys. Rev. **97,** 1538 (1955).

2. K.C. Kao, W. Hwang, “Electrical transport in solids”, Pergamon, Oxford, (1981).

3. H.T. Nicolai, M.M. Mandoc, P.W.M. Blom, “Electron traps in semiconducting polymers: exponential versus gaussian trap distribution” Phys. Rev. B. 83, 195204 (2011).

4. W.J. Baker, D.R. McCamey, K.J. Van Schooten, J.M. Lupton, C. Boehme, “Differentiation between polaron-pair and triplet-exciton polaron spin-dependent mechanisms in organic light-emitting diodes by coherent spin beating,” Phys. Rev. B. **84**, 165205 (2011).

5. T.D. Nguyen, G. Hukic-Makkosian, F. Wang, L. Wojcik, X.-G. Li, E. Ehrenfreund, Z.V. Vardeny, “Isotope effect in spin response of π-conjugated polymer films and devices,” Nat. Mater. **9**, 345 (2010).

CHAPTER 6

ADMITTANCE SPECTROSCOPY: RESULTS AND ANALYSIS

In this chapter, we present the results obtained from ac measurements (admittance spectroscopy). All the measurements were carried out at ambient conditions, always after dc measurements were performed on the sample. The samples used are the same that were listed in Chapter 5.

6.1 Theory

The ac admittance is defined as:

$$Y(\omega) = \frac{dI(\omega)}{dV(\omega)} \tag{6.1}$$

Because the current and voltage can have a phase shift, the admittance is a complex number written as

$$Y(\omega) = G(\omega) + i\omega C(\omega) \tag{6.2}$$

where ω is the angular frequency, $i^2 = -1$, $G(\omega)$ and $C(\omega)$ are respectively, the conductance and the capacitance of the device.

Since the device has the shape of a parallel plate capacitors, $C(\omega)$ can be expressed as:

$$C(\omega) = \varepsilon(\omega)\frac{A}{L} \tag{6.3}$$

where A is the cross-sectional area of the device, L is its thickness and ε is the dielectric constant of the EL polymer.

In general, the dielectric constant depends on frequency [1] as:

$$\varepsilon(\omega) = \varepsilon'(\omega) - i\varepsilon''(\omega) \tag{6.4}$$

where ε' and ε'' are respectively, the real part and the imaginary part of the permittivity of the EL polymer.

The combination of equations 6.2, 6.3 and 6.4 leads to and admittance of the form:

$$Y(\omega) = \omega\frac{A}{L}\varepsilon''(\omega) + i\omega\frac{A}{L}\varepsilon'(\omega) \tag{6.5}$$

The Kronig-Kramers relations help to derive $\varepsilon'(\omega)$ from $\varepsilon''(\omega)$ and vice-versa; the exact relations being related to the full knowledge of $\varepsilon(\omega)$.

A phenomenological approach that helps to interpret the admittance of a two-terminal semiconductor device under the effect of small harmonic excitation was given by Ershov *et al.* [2]. As shown in Figure 6.1 [2], the authors analyzed the time evolution of a transient current in the device after application of a voltage step (Figure 6.1 a). The results (Figure 6.1 b) can be described as:

$$\delta V(t) = V(t) - V(0^-) = \Delta V\theta(t) \tag{6.6}$$

$$\delta I(t) = I(t) - I(0^-) = \underbrace{[I(t) - I(\infty)]\theta(t)}_{\delta J(t)} + \underbrace{[I(\infty) - I(0^-)]\theta(t)}_{DC\,current} \tag{6.7}$$

where $\theta(t)$ is the unity step function, the "+" and "-" superscripts denote single-sided values of the discontinuous functions ($V(0^-) = \lim_{\tau\to 0} V(\tau),\ \tau \prec 0$) , δJ(t) represents the transient current (δJ(t) → 0 as t → ∞).

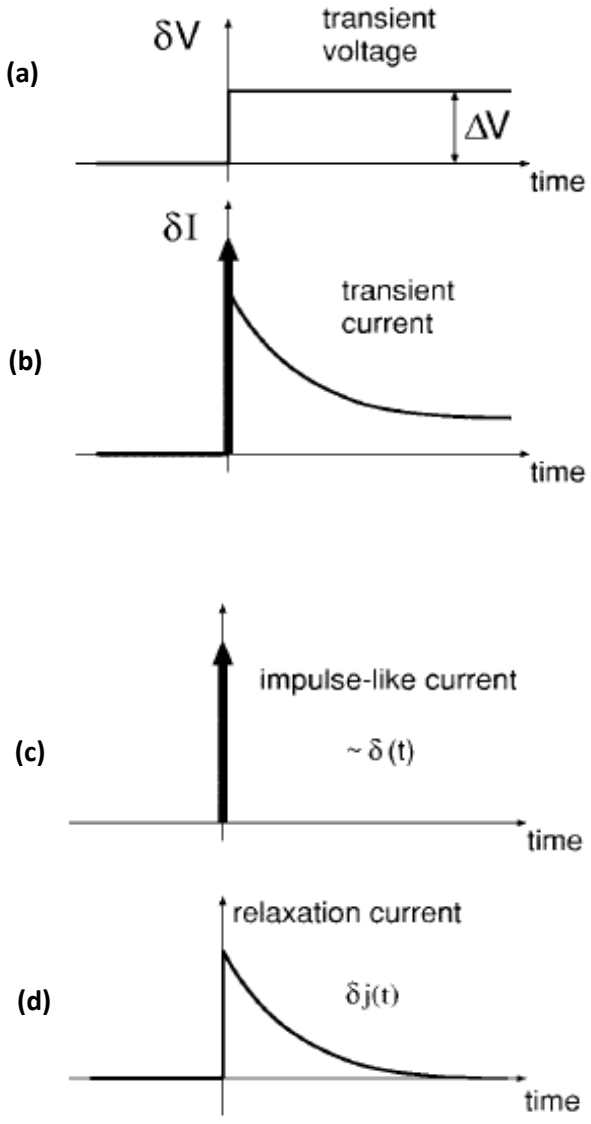

Figure 6.1: *Transient current as response of a voltage step applied to a semiconductor. From Ref. [2]*

The transient current, δJ(t), is the sum of an impulse-like current and a varying relaxation component described as:

$$\delta J(t) = C_0 \Delta V \delta(t) + \delta j(t) \tag{6.8}$$

where $C_0\Delta V\delta(t)$ corresponds to a current charging the geometric capacitance, assuming that application a voltage step results in an instantaneous change of charges on the contacts; δj(t) is the relaxation current due to charge transport, trapping or other physical process.

Combining the Fourier expansions of (6.6) and (6.7) with equation (6.1), and noting that $\int_{-\infty}^{\infty} \theta(t) e^{-i\omega t} = -i/\omega$, the admittance is:

$$Y(\omega) = \frac{i\omega}{\Delta V} \int_0^{\infty} \delta I(t) e^{-i\omega t} dt \tag{6.9}$$

After expansion of equation (6.8) and use of equation (6.2), the conductance and the capacitance of the device are given respectively, by:

$$G(\omega) = \frac{I(\infty) - I(0^-)}{\Delta V} + \frac{\omega}{\Delta V} \int_0^{\infty} \delta J(t) \sin \omega t \, dt \tag{6.10}$$

$$C(\omega) = \frac{1}{\Delta V} \int_0^{\infty} \delta J(t) \cos \omega t \, dt \tag{6.11}$$

The combination of equation 6.8 with equations 6.10 and 6.11 leads to:

$$C(\omega) = C_0 + \frac{1}{\Delta V} \int_0^{\infty} \delta j(t) \cos \omega t \, dt = C_0 + \frac{1}{\omega \Delta V} \int_0^{\infty} \left[-\frac{d\delta j(t)}{dt} \right] \sin \omega t \, dt \tag{6.12}$$

and

$$G(\omega) = G(0) + \frac{\omega}{\Delta V} \int_0^{\infty} \delta j(t) \sin \omega t \, dt = G(\infty) + \frac{1}{\Delta V} \int_0^{\infty} \left[\frac{d\delta j(t)}{dt} \right] \cos \omega t \, dt \tag{6.13}$$

If $-d\delta j(t)/dt$ is positive and decreases monotonically to zero, the positive contribution to the right part of equation (6.12) over the first half of the sine period overweighs the

negative contribution over the second half of a period [2]. This leads to a value of $C(\omega) > C_0$. In the opposite case, i.e., when $-d\delta j(t)/dt$ is negative and increases monotonically to zero, then $C(\omega) < C_0$ and it can reach a negative. Figure 6.2 illustrates the effect of the time behavior of $-d\delta j(t)/dt$ on the capacitance of the device.

Let us follow the work done by Ershov *et al.* to get a better understanding of the effect of times scales on the capacitance of the device. The authors considered a transient current represented by two exponential functions with different time scales τ_1 and τ_2:

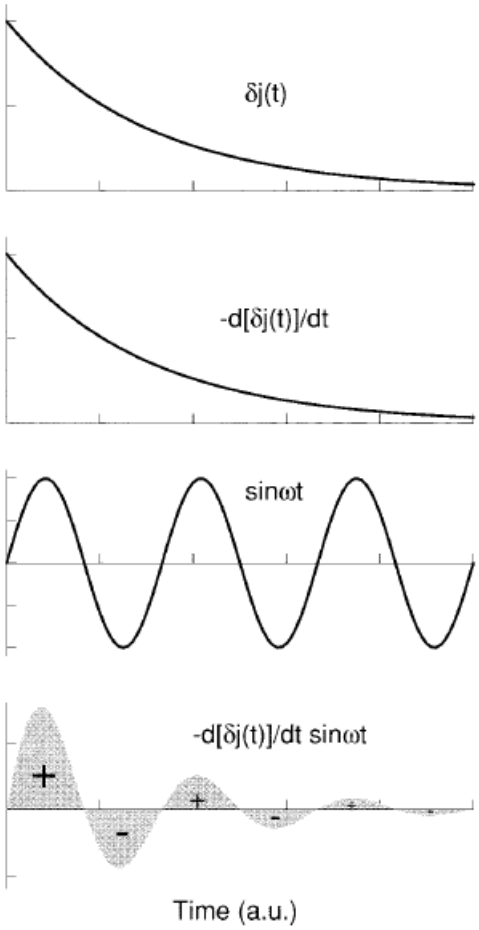

Figure 6.2: *Effect of the behavior of $-d\delta j(t)/dt$ on the capacitance $C(\omega)$. From Ref. [2])*

$$\Delta j(t) = \Delta V\left\{a_1 \exp\left(-\frac{t}{\tau_1}\right) - a_2 \exp\left(-\frac{t}{\tau_2}\right)\right\} \tag{6.14}$$

Using equations (6.12) and (6.13), the capacitance and conductance are respectively,

$$C(\omega) = C_0 + \frac{a_1\tau_1}{1+(\omega\tau_1)^2} - \frac{a_2\tau_2}{1+(\omega\tau_2)^2} \tag{6.15}$$

and

$$G(\omega) = G(0) + \frac{a_1(\omega\tau_1)^2}{1+(\omega\tau_1)^2} - \frac{a_2(\omega\tau_2)^2}{1+(\omega\tau_2)^2} \tag{6.16}$$

Figure 6.3 shows that the capacitance at certain frequencies of the device can be negative, depending on the value of time scales defining the relaxation current, and the sign and magnitude of their amplitude a_1 and a_2.

label	τ_1	τ_2	a_1	a_2
1	1	2	1	0
2	1	2	2	1
3	2	1	1.5	2
4	1	2	0	0.5

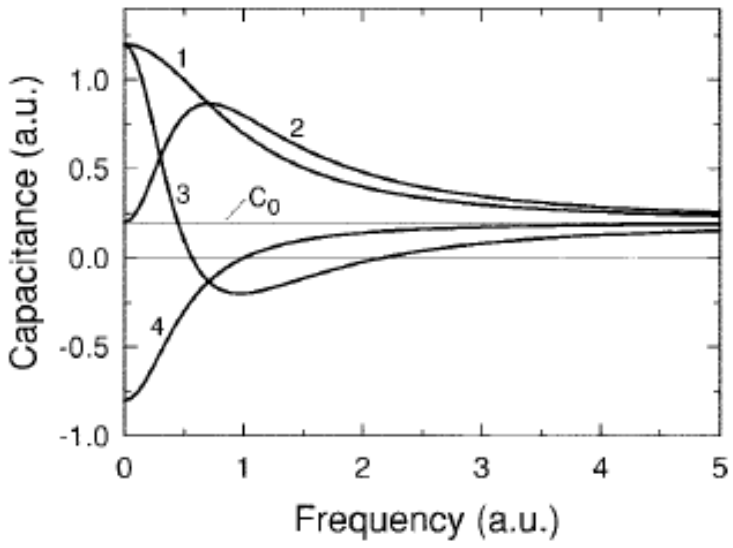

Figure 6.3: *Effect of the phenomena time scales on the capacitance C(ω). From Ref. [2]*

This phenomenological approach was used in [3] to derive the bimolecular recombination time in MDMO-PPV devices. We will use it as the basis to fit our experimental data.

The effect of the magnetic field is studied by measuring the admittance of the device with and without the magnetic field. Two dimensionless parameters were introduced to characterize that effect, i.e., the magnetoconductance MG(B,ω) and the magnetocapacitance MC(B, ω) respectively, defined as:

$$MG(B,\omega) = \frac{G(B,\omega) - G(0,\omega)}{G(0,\omega)}$$

and (6.17)

$$MC(B,\omega) = \frac{C(B,\omega) - C(0,\omega)}{C(0,\omega)}$$

6.2 Experimental Results

6.2.1 Unipolar devices

The experimental results obtained for device E, which has the stacking sequence ITO/PEDOT-PSS/MEH-PPV/Au are presented in Figure 6.4. At each frequency, the admittance was measured at 0 *mT*, then at 30 *mT* with a waiting time of 2 seconds. This procedure ensures that the magnetic field effects are not due to drift in the device characteristics [4]. It can be observed from that figure that the magnetic field effect was detected neither in the conductance nor in the capacitance of the device. Figure 6.4(b) shows that no deviation of MG from zero was resolved. The capacitance data in Figure 6.4(c) indicate the presence of a negative low frequency contribution at bias voltage larger than 2 *V*. The magnitude of this contribution increases as the bias voltage increases.

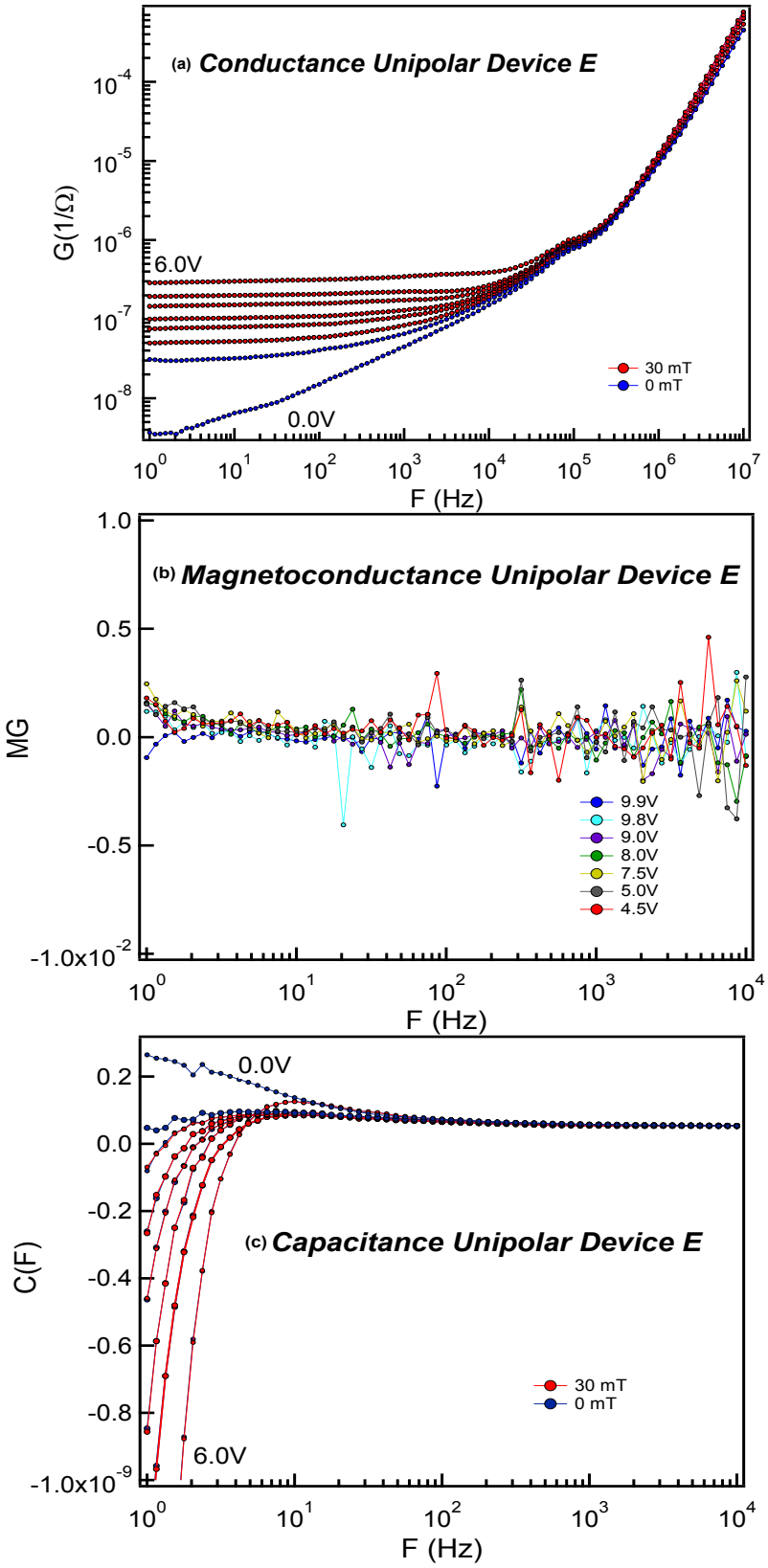

Figure 6.4: *Admittance data for unipolar device E, (a) is the conductance; (b) is the magnetoconductance; (c) capacitance*

6.2.2 Bipolar devices with PEDOT-PSS

In Figures 6.5 and 6.6, respectively, we display the conductance and capacitance data obtained for bipolar device B (ITO/PEDOT:PSS/MEH-PPV/Ca/Al). The conductance and capacitance were obtained using equation 4.4, where the sum of the resistances of ITO and aluminum electrodes R_1+R_2 was 36Ω, and the magnetoconductance was calculated using equation 6.17. The experimental results for the bipolar sample show the strong effect of the magnetic field on the conductance and the capacitance of the device.

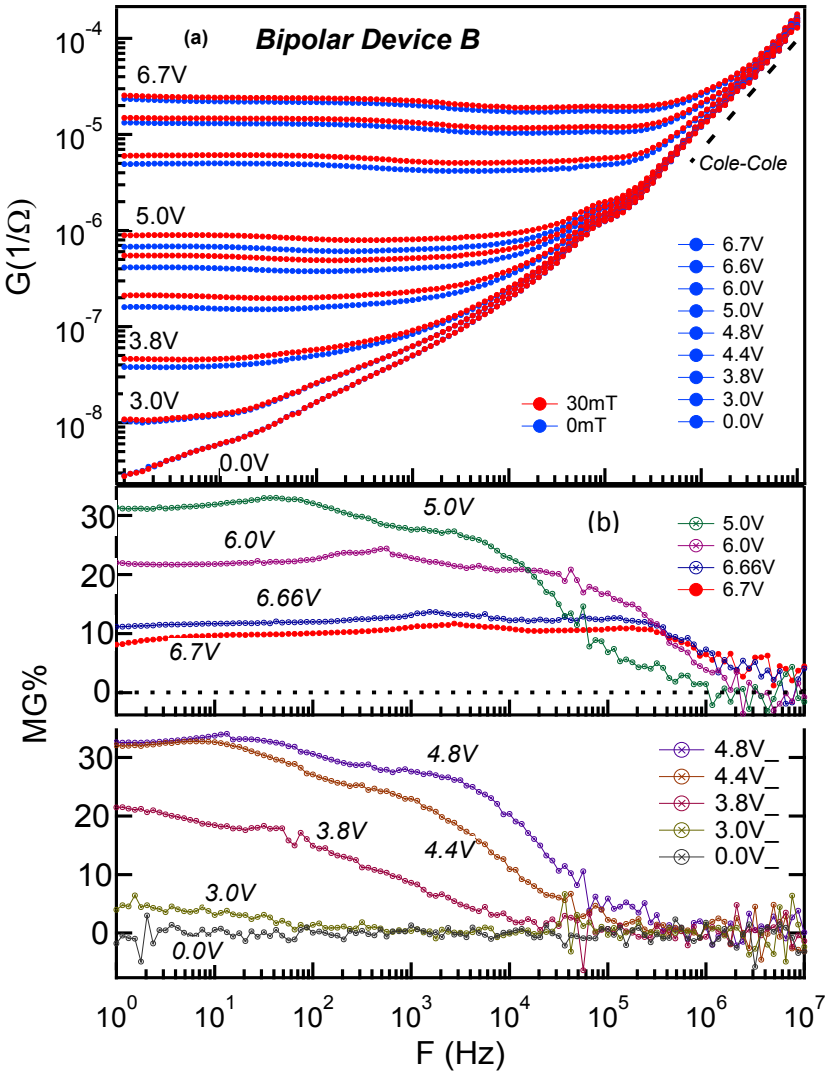

Figure 6.5: *(a) Conductance data for bipolar device B; (b) magnetoconductance data for bipolar device B*

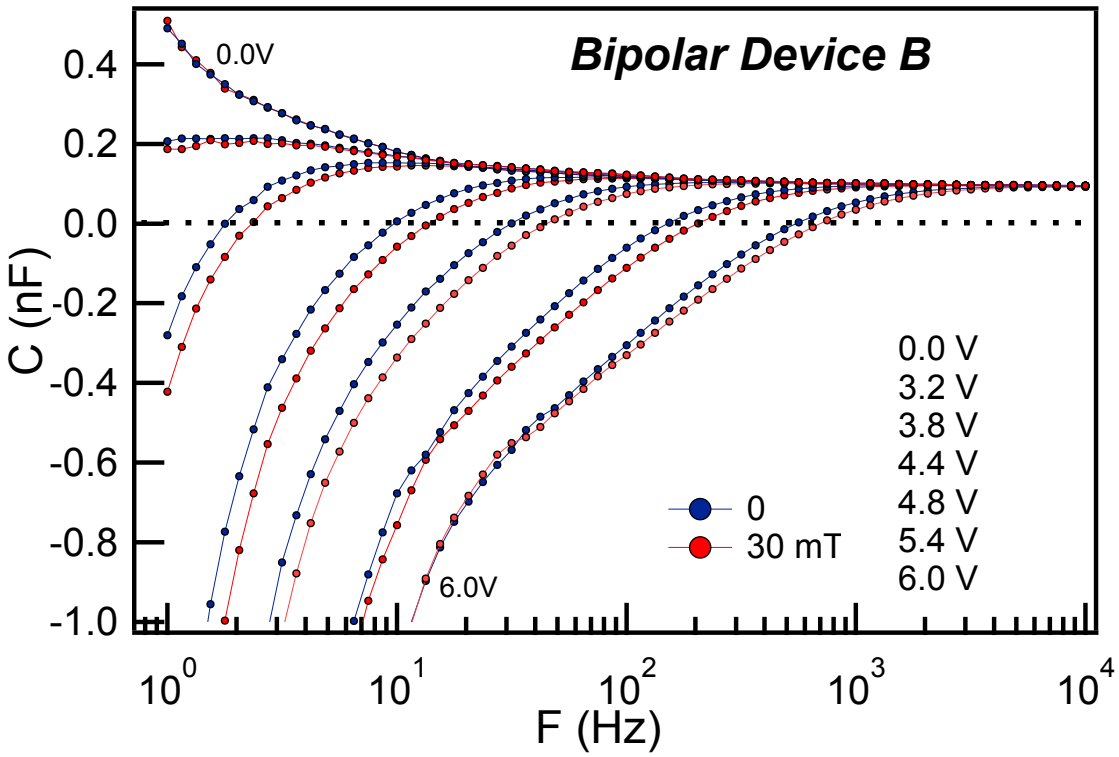

Figure 6.6: *Capacitance data for bipolar device B*

6.2.3 Bipolar device without PEDOT-PSS

The sample measured here is the bipolar ITO/MEH-PPV/Ca/AL, with the thickness of MEH-PPV being 150 *nm*. In Figure 6.7, we display the conductance and capacitance data obtained for bipolar device I (ITO/ MEH-PPV/Ca/AL). The conductance and capacitance were obtained using equation 4.4, where the sum of the resistances of ITO and aluminum electrodes was $R_1+R_2 = 36\ \Omega$.

6.3 Analysis and discussions

In order to verify the correctness of our experimental technique, the consistency between the measured capacitance and conductance was checked using the Kramers-Kronig (KK) relation. Using the capacitance of device B (Figure 6.6) at 0.0 V ($C_0(0,\omega)$), the expected conductance can be calculated using the Kramers-Kronig (KK) relations.

For the complex dielectric $\varepsilon(\omega) = \varepsilon'(\omega) - i\varepsilon''(\omega)$, the real and imaginary parts are related one to the other according to the KK relations [1]:

$$\varepsilon'(\omega) = \varepsilon_\infty + \frac{1}{\pi}\int_{-\infty}^{+\infty}\frac{\varepsilon''(\theta)}{\theta-\omega}d\theta \tag{6.18}$$

and

$$\varepsilon''(\omega) = \frac{1}{\pi}\int_{-\infty}^{+\infty}\frac{\varepsilon'(\theta)}{\theta-\omega}d\theta \tag{6.19}$$

According to the phenomenological theory developed by Bottcher and Bordewijk [1], relations (6.18) and (6.19) have been derived for the case that the induced polarization can be assumed to follow the field without any delay. This implies that the integration should be cut off at a frequency in the range between the characteristic frequencies of the orientational and the induced polarization. They [1] also pointed out

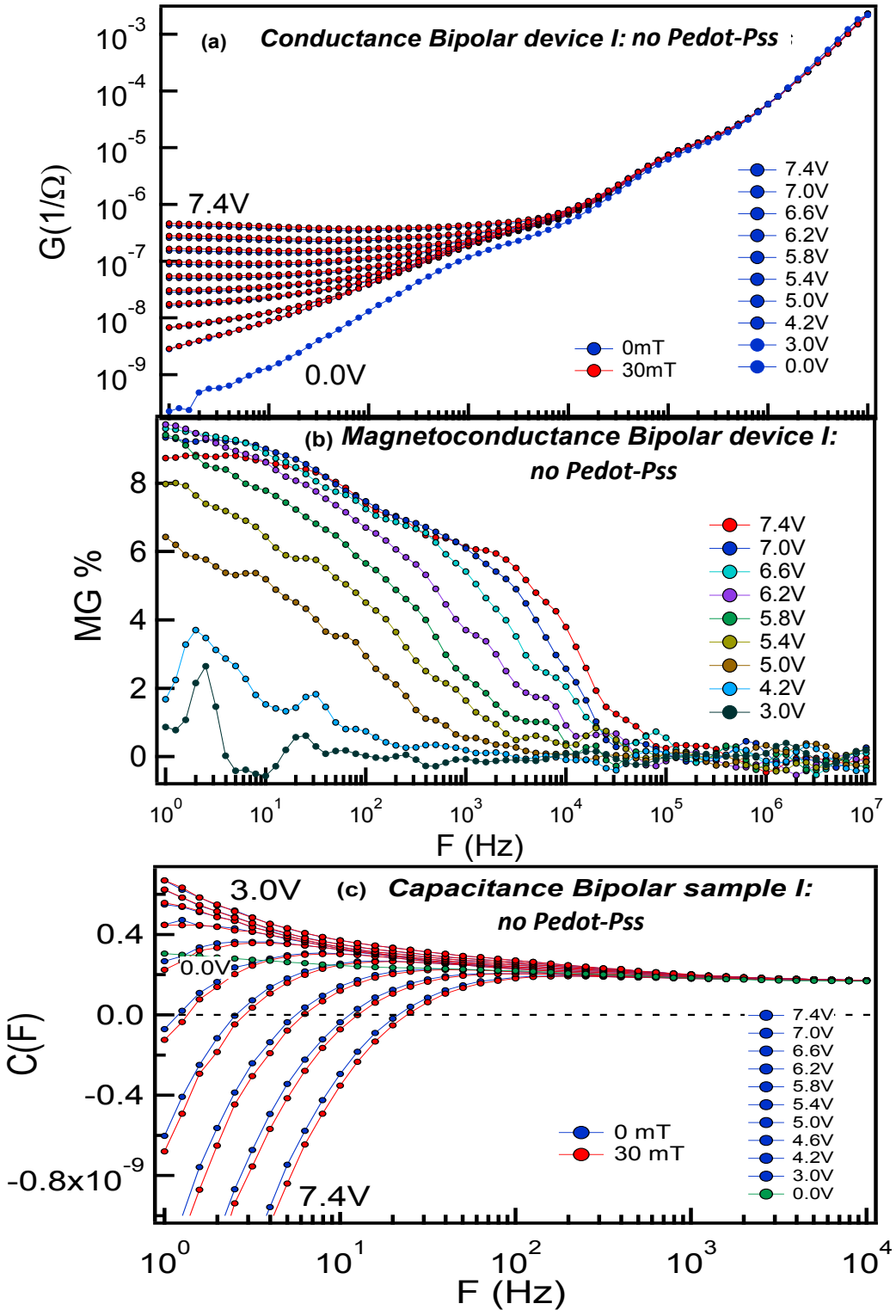

Figure 6.7: *Admittance data for bipolar device I, (a) is the conductance; (b) is the magnetoconductance; (c) capacitance*

that the behavior of the orientational polarization of most condensed systems in time-dependent fields can, as a good approximation, be characterized with a distribution of relaxation times. Assuming that the distribution of relaxation times is very broad, they approximated the factor $\frac{\theta^2}{\omega^2-\theta^2}$ by the unit-step function $S(\theta-\omega)$ and used it in equation (6.18) to get:

$$\begin{aligned}
\varepsilon'(\omega) = \varepsilon_\infty + \frac{1}{\pi}\int_{-\infty}^{+\infty}\frac{\varepsilon''(\theta)}{\theta-\omega}d\theta = \varepsilon_\infty + \frac{2}{\pi}\int_0^\infty \frac{\theta\varepsilon''(\theta)}{\omega^2-\theta^2}d\theta \qquad (a)\\
= \varepsilon_\infty + \frac{2}{\pi}\int_0^\infty \frac{\theta^2\varepsilon''(\theta)}{\omega^2-\theta^2}dLn\theta \qquad (b)\\
= \varepsilon_\infty + \frac{2}{\pi}\int_\omega^\infty S(\theta-\omega)\varepsilon''(\theta)dLn\theta \qquad (c)\\
= \varepsilon_\infty + \frac{2}{\pi}\int_\omega^\infty \varepsilon''(\theta)dLn\theta \qquad (d)
\end{aligned} \tag{6.20}$$

It follows from equation 6.20 (d) that:

$$\varepsilon'' = -\frac{\pi}{2}\frac{d\varepsilon'(\omega)}{d(\ln(\omega))} \tag{6.21}$$

From equation 6.5 and Figure 6.6, the calculated conductance at 0.0 V and 0 mT, G_{KK} is

$$G_{KK} = \omega\frac{A}{L}\varepsilon''(\omega) \tag{6.22}$$

The good agreement (Figure 6.8) between the calculated G_{KK} and the measured $G(0,\omega)$ at 0.0 V confirms the overall accuracy of our measurements.

This observation also points out that the low-frequency $G(\omega)$ and $C(\omega)$ responses at zero bias come from the same physical process, which is related to the presence of trap states [4].

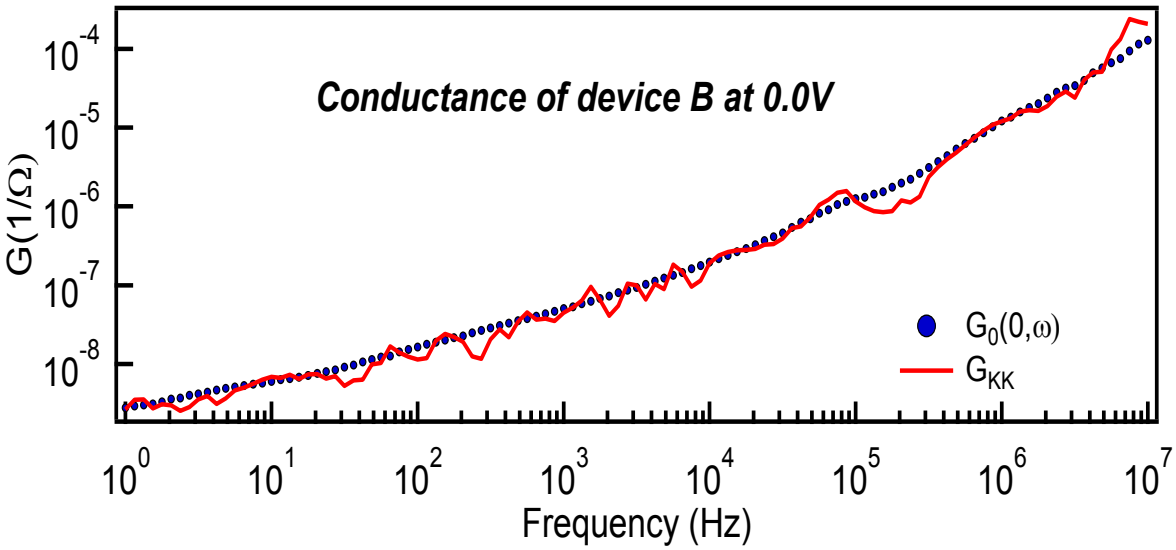

Figure 6.8: *Conductance of device B. In blue, the measured conductance at 0V and 0mT; in red, the conductance obtained from the corresponding capacitance and KK relation*

6.3.1 Unipolar devices

The experimental results shown in Figure 6.4 tell us that the admittance of the ITO/PEDOT-PSS/MEH-PPV/Au stays the same when measured at 0 *mT* and 30 *mT*. From Chapter 3, the only model supporting the OMAR effect in unipolar samples is the bipolaron model. This model predicts a negative magnetoconductance at low magnetic field (< 10 *mT*) and a positive magnetic field at high magnetic field. Thus, our measurements were done in high field regime. The lack of any detectable magnetoconductance strongly suggests that the bipolaron process gives very small (or perhaps even zero) contribution to the OMAR effect in MEH-PPV.

The capacitance of bipolar device shows negative values at low frequency, for high bias voltages. E. Ehrenfreund *et al.* [3] and H.H.P. Gommans *et al.* [5] explanations of the negative capacitance is based on recombination process, hence on bipolar injection. From this perspective, the presence of negative contribution to the device capacitance at

high biases can be taken as the evidence of bipolar injection. If this is the case, the polaron pair model and the exciton-charge interaction model should also be considered for the understanding of the OMAR effect in this unipolar device.

The capacitance vs. frequency graphs were fitted using equation (6.15) with a single time constant ($\tau_2 = 0$), i.e., $C(\omega) = C_0 + \frac{a_1\tau_1}{1+(\omega\tau_1)^2}$. The relaxation time obtained was $\tau_1 = 0.8\ s$ and it was not bias voltage dependent. At low frequency and $V_b = 6\ V$ the negative capacitance term has the same time constant $\tau_1 = 0.8\ s$ as in the bipolar device, but its magnitude is about 100 times smaller than C_{10} in bipolar device B at the same bias. In fact, the behavior of the unipolar device can be better understood within the trap-assisted recombination assuming that at sufficiently high bias electrons are directly injected into localized trap states. Within this mechanism the trap assisted recombination is confined to a narrow layer of PPV adjacent to the cathode, and consequently is expected to produce a much smaller contribution to the negative capacitance. The life time is still determined by the hole capture and is expected to be the same as in bipolar devices.

6.3.2 Bipolar devices with PEDOT-PSS

6.3.2.1- High frequency cut-off of OMAR. Figures 6.5 and 6.6 show that the OMAR effect is large in our bipolar devices. The difference between the conductance G(ω) at 0 *mT* and 30 *mT* can be easily observed; the same goes for C(ω) at 0 *mT* and 30 *mT*. Figure 6.5 (b) shows that the magnetoconductance increases with the applied voltage, reaches a maximum of 35% at 4.8 *V*, and then starts decreasing as the bias increases. It is also observed that MG(ω) has a characteristic frequency cutoff that shifts to higher

frequencies as the bias voltage increases. At the highest voltage measured, 6.7 V, this sample shows OMAR effect in the full frequency range: MG was detected at 10 MHz and its value was about 4.5%. We believe that the cutoff frequency does not represent a process associated with the OMAR effect. It is observed that for all bias voltages, the device conductance strongly increases at high frequencies. This effect was also observed in OC_1C_{10}-PPV devices and was attributed to the presence of permanent electric dipoles in the organic material [6]. If the dipoles' response is characterized by a distribution of relaxation times, then the dielectric constant can be described by the empirical Cole-Cole equation [4]

$$\frac{\varepsilon(\omega)}{\varepsilon_0} = \varepsilon_\infty + \frac{\varepsilon_s - \varepsilon_\infty}{1 + (i\omega\tau_0)^{1-\beta}} \tag{6.23}$$

where β is the "dispersion parameter" and τ_0 is the dipoles' mean relaxation time.

Combining equation (6.23) and the real part of equation (6.5), $G(\omega)$ is calculated with $A = 0.9\ mm^2$ and $L = 150\ nm$. The calculated $G(\omega)$ is plotted in Figure 6.5 (a), which is downshifted for clarity. The best fitting parameters for this approximation are: $\varepsilon_s - \varepsilon_\infty = 0.4$, $\beta = 0.8$, and $\tau_0 = 0.5\ ns$. The value of the capacitance at high frequency is $\varepsilon_\infty = 2.5$. This approximation matches the data well at high frequencies. At f < 100 *kHz* the experimental conductance exceeds the estimated value from the Cole-Cole model; this indicates the presence of additional physical processes that contribute to the conductance at low frequency. Indeed the capacitance response at zero voltage (Figure 6.6) reveals a strong positive frequency-dependent contribution. This contribution is typically associated with the presence of trap states in the active material [4]. At high bias voltage (6 V for example), the conductance is almost frequency-independent at low

frequencies (< 500 *kHz* for 6 *V*); at high frequency, it merges with the conductance at 0 *V*. This means that at high frequency, the effect of the injected carriers on the conductance becomes negligible and the conductance of the device is dominated by the relaxations processes that are likely related to the relaxation of permanent dipoles.

6.3.2.2- Times scales of different physical processes. The magnified version of Figure 6.6, presented here as Figure 6.9, reveals that at frequencies above 10 *kHz* the capacitance does not depend on voltage or frequency; it is in fact equal to the 'geometrical' capacitance, C_0. The behavior at f < 10 *kHz*, however, is much richer. At zero bias $C(\omega)$ is positive and increases with decreasing frequency. This positive contribution is typically associated with the presence of trap states in the EL layer [6]. As the applied voltage (V_B) increases, a negative contribution starts to appear at low frequency, and shift to higher frequency as V_B increases. Bimolecular and trap assisted recombination [3, 5], electrons injection through interfacial states [7] are possible physical explanations of the negative capacitance. Close inspection of the data suggests that there are two negative contributions to the device capacitance, C_1 and C_2, where C_1 is dominant for the frequency less than 10 *Hz* and C_2 is dominant for the frequency interval 10 *Hz* < f < 1 *kHz*. Both contributions are strongly affected by the magnetic field.

To verify the presence of C_1 and C_2 contributions, we plotted $-Z''(\omega)$ vs. $Z'(\omega)$ (the Cole-Cole plot) where Z'' and Z' are the imaginary and real part of the device impedance, respectively. Figure 6.10 shows the Cole-Cole plots for device B at bias voltages $V_B = 4.4\,V$ and $V_B = 6.0\,V$. For both biases the low-frequency part of the Cole-Cole plot shows a characteristic bend. The change in the curvature of the Cole-Cole curve

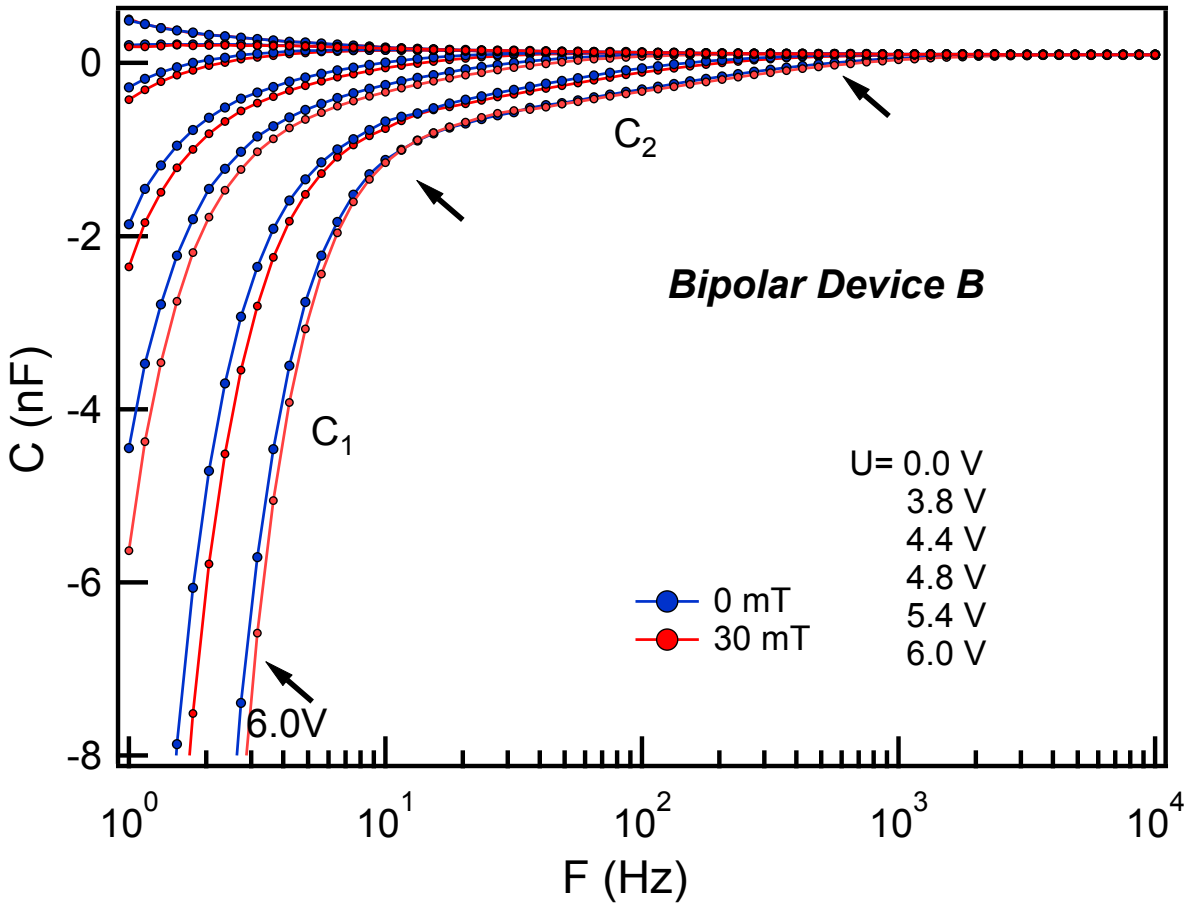

Figure 6.9: *C vs. F of bipolar device B. The areas of C_1 and C_2 contributions are highlighted*

suggests an additional process with distinct time constant [4]. For these plots, the impedance of the devices were determined as

$$Z(B,\omega) = \frac{1}{Y(B,\omega)} = Z'(B,\omega) + iZ''(B,\omega) \tag{6.24}$$

From the theory developed in section 6.1, it was shown that when $-dj(t)/dt$ is negative and increases monotonically to zero, $C(\omega)$ is smaller than the geometrical capacitance C_0 and total differential capacitance in fact can be negative.

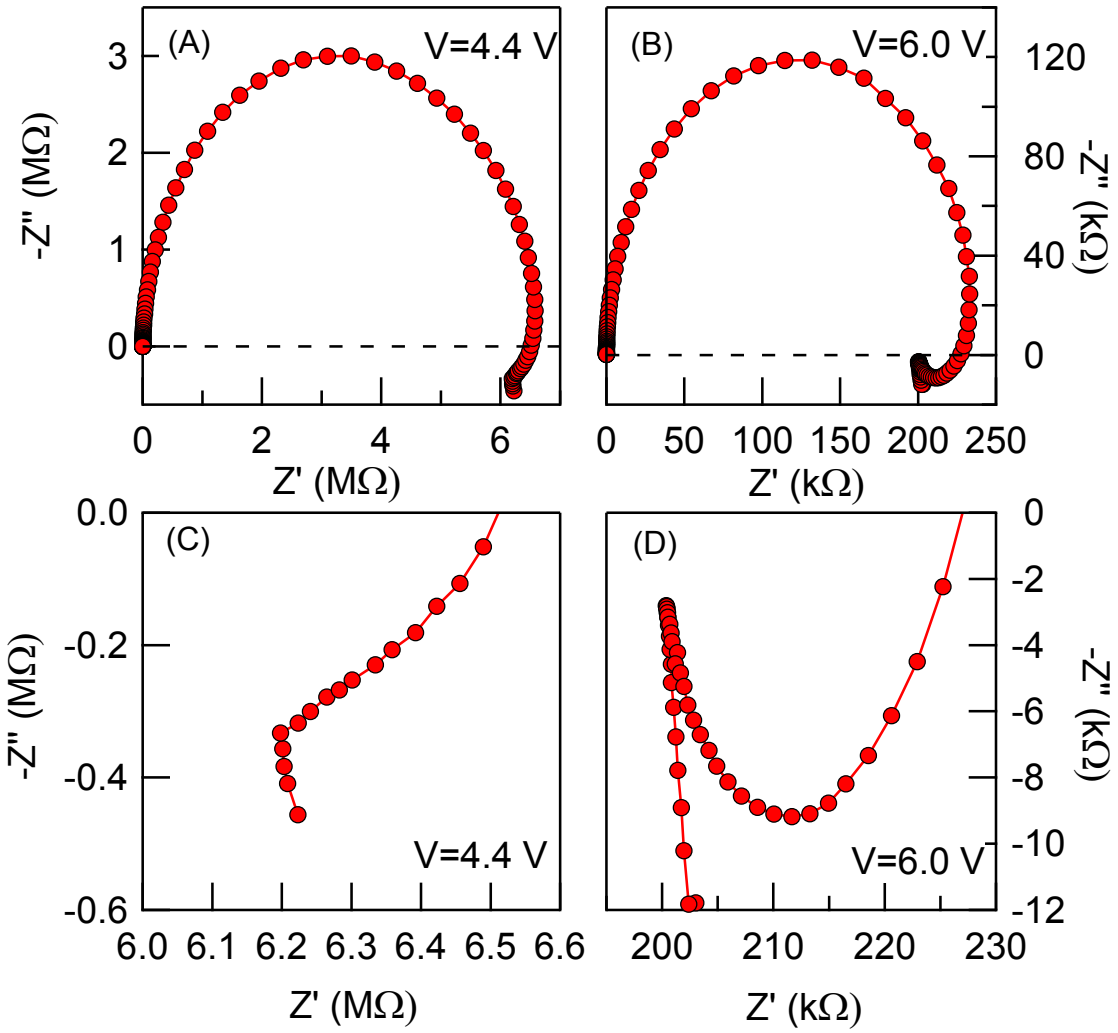

Figure 6.10: *The Cole-Cole plot for the bipolar device B. Panel (A) bias voltage V=4.4 V and panel (B) V=6 V. Panels (C) and (D) emphasize the low frequency regions of (A) and (B), respectively.*

In a simple case when the transient current relaxes exponentially in time with a single time constant as

$$\Delta j(t) = \Delta V a_1 \exp\left(-\frac{t}{\tau_1}\right) \tag{6.25}$$

with $a_1 \Delta V$ negative, the admittance is determined by equation (6.9) and the capacitance and the conductance are as derived in equations (6.15) and (6.16), i.e.,

$$C(\omega) = C_0 + \frac{a_1 \tau_1}{1 + (\omega \tau_1)^2} \tag{6.26}$$

and

$$G(\omega) = G_0 + \frac{a_1 (\omega \tau_1)^2}{1 + (\omega \tau_1)^2} \tag{6.27}$$

where G_0 represents the steady state conductance.

Equations (6.26) and (6.27) can be used to approximate C_1, i.e., $C(\omega)$ below 10 *Hz*. The high-frequency contribution, as shown by the Cole-Cole plots, needs to take into account the distribution of relaxation times. This is done by introducing a dispersion parameter α for the second high-frequency term in equation (6.28):

$$C(\omega) = C_0 - C_{10} \frac{1}{1 + (\omega \tau_1)^2} - C_{20} \mathrm{Re}\left[\frac{1}{1 + (i\omega \tau_2)^{1-\alpha}}\right] \tag{6.28}$$

where $\alpha = 1$ for nondispersive transport, *Re* represents the real part of the complex expression in bracket. C_{10}, C_{20}, τ_1, τ_2, and α are the fitting parameters that characterize the two contributions to the negative capacitance. The equation was used to fit C vs. f (frequency) dependences for sample B and sample A, which are both bipolar ITO/PEDOT-PSS/MEH-PPV/Ca/Al with respective thicknesses of MEH-PPV 150 *nm*

and 80 *nm*. For both devices, fits agree quite well with the experimental data. Figure 6.11 shows the fits of *C* vs. *f* for device B.

The data are fitted for biases in the range 4.4 $V < V_B < 6\ V$. For the capacitance at $6V$, the fitting with dispersion parameter $\alpha = 0$ (single time constant at high frequency) and $\alpha = 0.16$ are shown in Figure 6.11. It is observed that α improves the agreement between the fit and the experimental data, but it only slightly affects the values of the other fitting parameters.

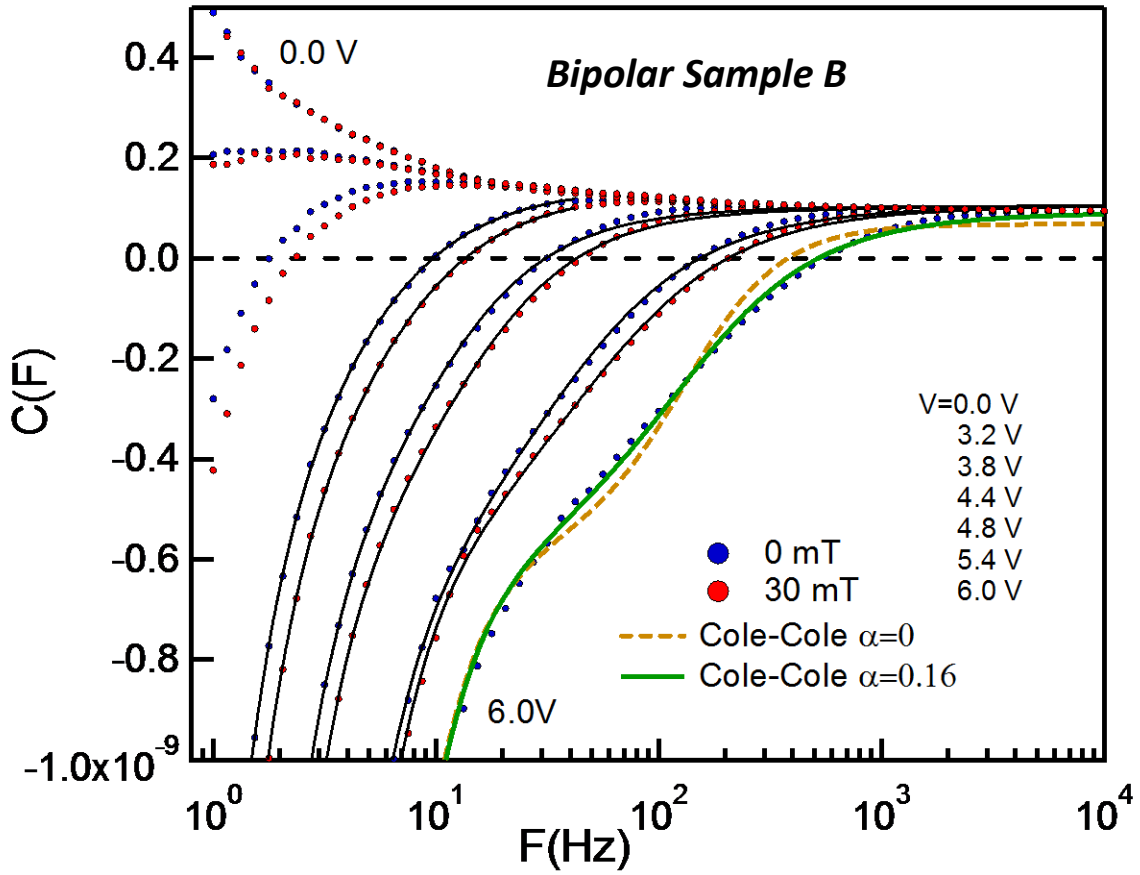

Figure 6.11: *Differential capacitance vs. frequency at the magnetic field B=0 mT and B=30 mT for device B at indicated voltages. The dashed line is a fit to the theoretical model with the dispersive parameter α set to zero, whereas the solid lines are fits with α as a free parameter.*

The fitting parameters $\tau_1 \approx 0.8\ ns$, $C_{20} \approx 0.6\ nF$ and $\alpha \approx 0.16$ were found to be bias independent, oppositely to C_{10} and τ_2 that show bias dependence, as illustrated in Figure 6.12. It is noticeable that both C_{10} and τ_2 are exponential functions of V_B, C_{10} increasing with V_B as $C_{10} \approx \exp(\gamma V_B)$, whilst τ_2 is decreasing as $\tau_2 \approx \exp(-\lambda V_B)$ where the constant γ and λ are positive. The fittings of C_{10} and τ_2 as functions of V_B show that $\gamma = -\lambda = 2.25\ \mathrm{V}^{-1}$ for device B and $\gamma = -\lambda = 2.7\ \mathrm{V}^{-1}$ for device A. Following equation (6.28), the conductance of the device can be fitted by:

$$G(\omega) = G_0 - C_{10}\frac{\omega^2\tau_1}{1+(\omega\tau_1)^2} + C_{20}\,\mathrm{Im}\left[\frac{\omega}{1+(i\omega\tau_2)^{1-\alpha}}\right] + G_{CC} \qquad (6.29)$$

where *Im* represents the imaginary part of the complex expression in bracket and G_{CC} is the Cole-Cole contribution to the AC conductance. G_{CC} can be evaluated from $G(\omega)$ at zero-bias.

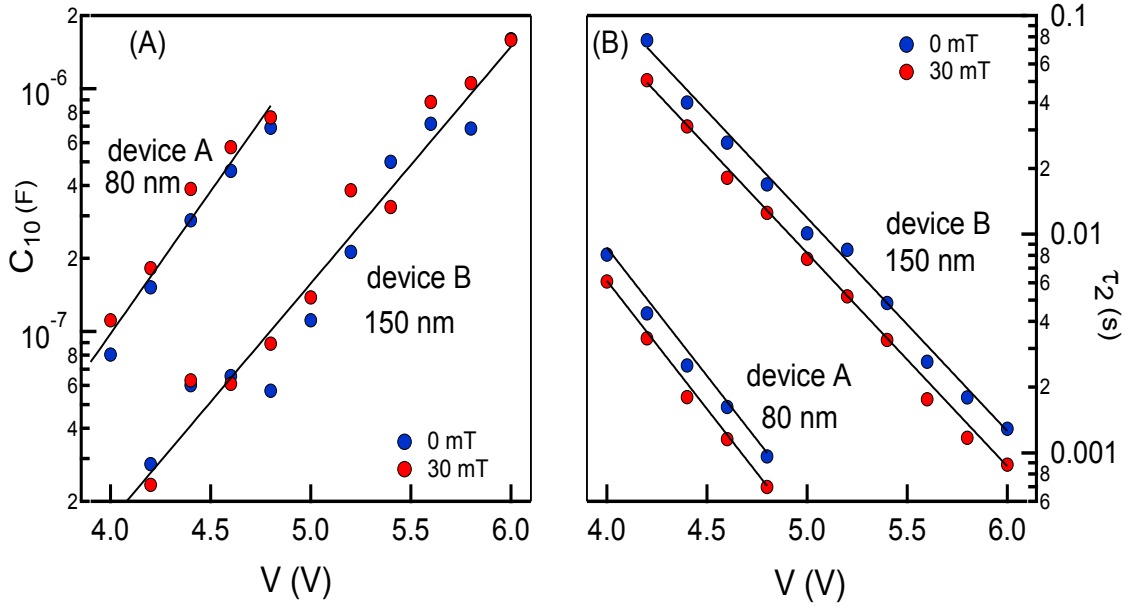

Figure 6.12: *The dependence of the fitting parameters on the bias voltage for devices B and: (A) C_{10} and (B) τ_2*

At 6.0 V, equation (6.29) fits $G(\omega)$ vs. f at 0 mT and 30 mT quite well, with the fitting parameters C_{10}, C_{20}, τ_1, τ_2, and α being the same that fit $C(\omega)$ at 6.0 V (Figure 6.13). The parameter G_0 does not depend on the frequency, but may be magnetic field dependent.

For the fitting at 0 mT and 30 mT in Figure 6.13, we used the same parameters C_{20}, τ_1, and α; whilst C_{10}, τ_2 and G_0 depend on the magnetic field ($\tau_2 = 1.2\ ms$ at 0 mT and $\tau_2 = 0.9\ ms$ at 30 mT). C_{10} and τ_2 are obtained from Figure 6.12 and G_0 is obtained from Figure 6.5 (a). The combination of equations (6.17) and (6.29) leads to a theoretical value of $MG(\omega)$ at 6.0V. That theoretical value is plotted against the frequency in Figure 6.13 (B). It agrees quite well with the experimental curve at that bias voltage. In particularly, the theory reproduces a small broad peak with the center at $f = 300Hz$ that is due to the effect of the magnetic field on τ_2. The cutoff of the magnetoresistance is also well approximated and can be related to the magnetic-field-independent Cole-Cole contribution to the conductance.

It is clear that the physical processes that manifest themselves in the device under bias are of two different regimes, i.e., C_1 and C_2, with characteristic times scales τ_1 and τ_2.

The time τ_2 shows a strong dependence on electric field and hence on the concentration of charge carriers in the device. The application of a magnetic field of 30 mT decreases the time τ_2 by approximately 30% and this variation is bias independent. In the polaron pair (PP) model of OMAR by Prigodin, the key element is the effect of the magnetic field on the dissociation and recombination rates of positive and negative

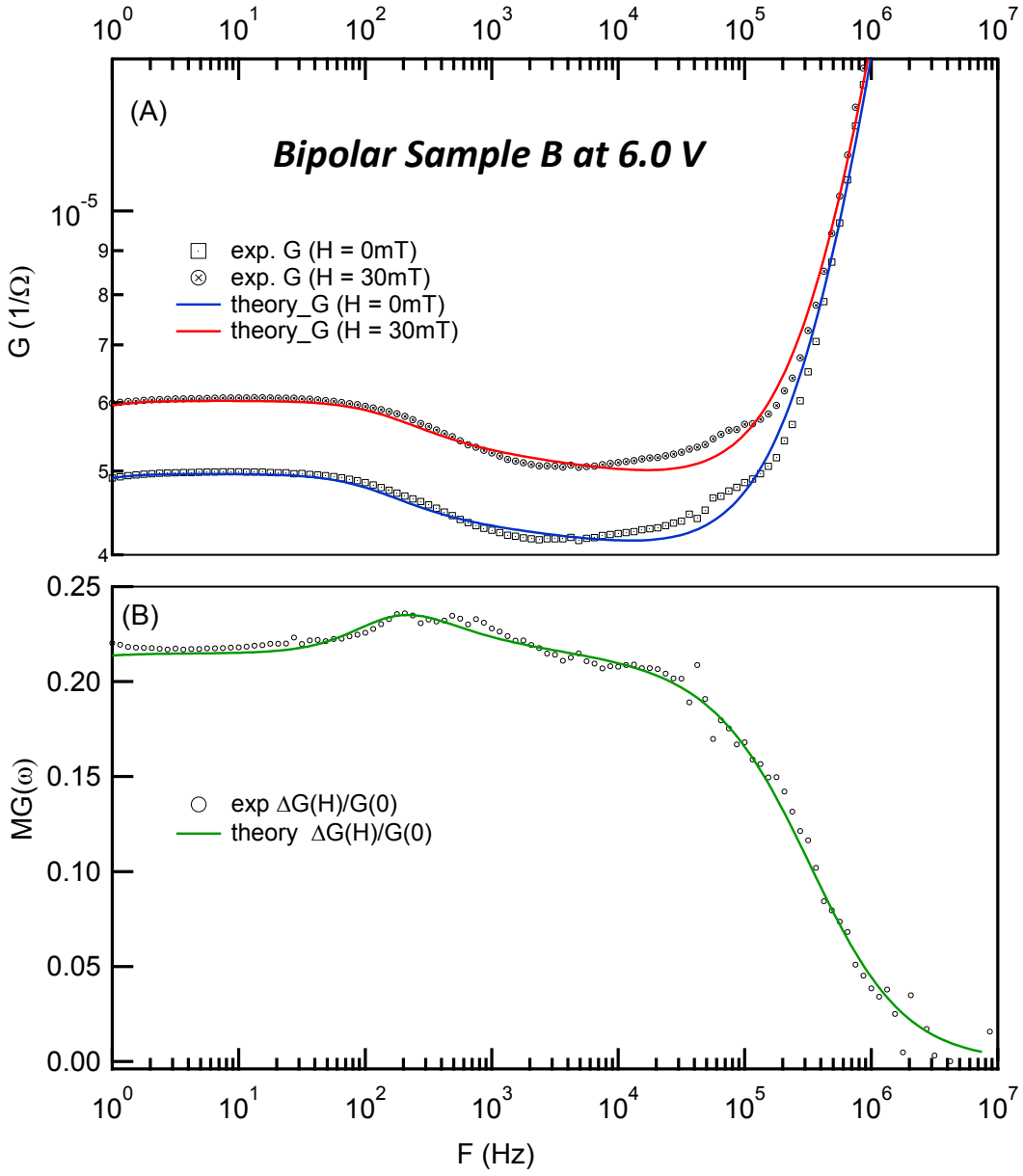

Figure 6.13: *(A) Differential conductance as a function of frequency for device B at* $V_B = 6V$ *and indicated magnetic fields. (B) The magnetoconductance, MG (ω), of device B measured at 30 mT and 6V*

polaron pairs. The Langevin-type bimolecular recombination predicts that the recombination time decreases as the carrier concentration grows.

To emphasize the dependence of τ_2 on the carrier's concentration, the graphs of $1/\tau_2$ vs. V and the current I vs. V were plotted in the range of 4 V < V_B < 6 V (Figure 6.14). This figure shows that $1/\tau_2$ and current I have the same dependence on V_B in this voltage range. In fact, both are affected in the same way by the charge density in the device.

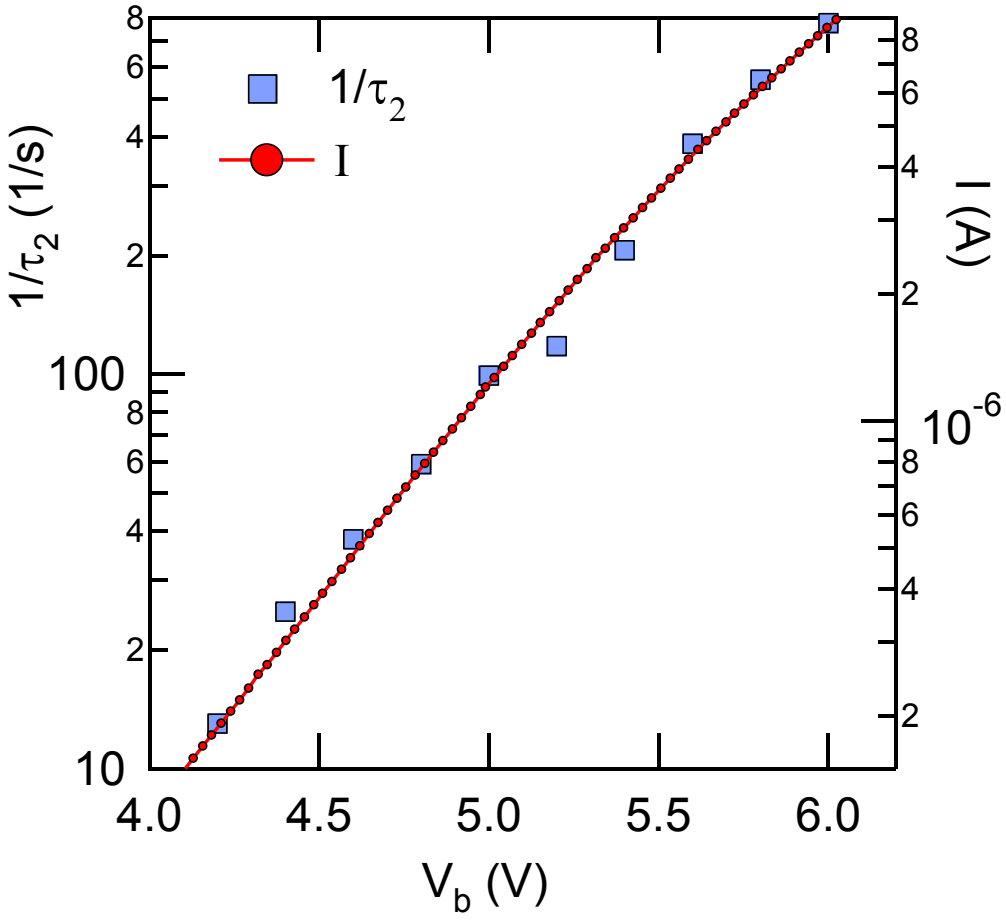

Figure 6.14: *The inverse of the relaxation time τ_2 as a function of the bias voltage (left axis) alongside with the DC current vs. bias voltage (right axis)*

The similarity between the behaviors of τ_2 and the recombination time as described by Langevin suggests that the C_2 regime results from bimolecular recombination taking place in the device. Moreover, this C_2 contribution is absent in the capacitance vs. frequency dependence of unipolar device presented in Figure 6.4 (c).

The life-time of excess carriers for bimolecular recombination (BMR) kinetics may be written as $\tau_{BM}^{-1} \approx \lambda\langle n\rangle$, where $\lambda = \langle v\rangle\sigma_R$, $\langle v\rangle$ is the relative velocity of positive and negative polarons, $\langle n\rangle$ is an average concentration of carriers and σ_R is their recombination cross-section. From this relation, we expect that τ_{BM}^{-1} depends strongly on the carrier concentration and correspondingly on the bias voltage. This behavior is clearly displayed by the time constant τ_2. If we assume that the bias dependence of τ_2 comes from the increase in charge carrier density, we can also explain why parameter C_{20} does not depend on the bias voltage. From equations (6.27) and (6.28), we have $C_{20} = j_{20}\tau_2 / \Delta V$ where $j_{20} = -a_1\Delta V$ is a magnitude of the relaxation current for the fast process at $t = 0$, immediately after application of a voltage step ΔV. j_{20} is expected to be directly proportional to the carrier concentration $\langle n\rangle$. Since $\tau_2 \sim \langle n\rangle^{-1}$, the two dependencies cancel each other and $j_{20}\tau_2$ is not carrier density dependent. Hence the parameter C_{20} is expected to be bias-independent [4].

For frequencies less than 10 *Hz*, i.e., in C_1 regime, the effect of the magnetic field on the negative capacitance is more difficult to interpret. In fact, the fittings reveal a value of $\tau_1 \approx 0.8\ s$ that is independent on electric field and magnetic field and the term C_{10} which, even though dependent on the bias voltage, does not display a clear dependence on the magnetic field.

N.D. Nguyen *et al.* [8] showed that the negative capacitance in the low frequency regime (0.1 Hz < f < 20 Hz) obtained from admittance spectroscopy measurements of α-NPD can be due to the presence of a band of traps which modifies the charge distribution within the organic layer and the injection of electrons from the cathode. E. Ehrenfreund [3] showed that for trap mediated recombination in MDMO-PPV, the recombination time should be interpreted as the characteristic capture time for positive (negative) charge into a negatively (positively) charged trap. Moreover, the capture rate is not expected to be bias dependent and hence does the recombination time. The similarity between the bias independence of τ_1 and the physical explication proposed by E. Ehrenfreund [3] suggests that the C_1 regime corresponds to the regime of trap mediated recombination. This interpretation allows understanding why the magnitude of the term C_{10} has the same dependence on voltage as the inverse recombination time $1/\tau_2$ and the DC current. From equation (6.26), we have $C_{10} = j_{10}\tau_1 / \Delta V$. Since τ_1 is expected to be constant for trap-assisted recombination, the term C_{10} is determined by the magnitude of the relaxation current j_{10}, which as well as the dc current and $1/\tau_2$ is determined by the carrier density. Thus, the attribution of C_1 term to the trap-assisted recombination and C_2 term to the bimolecular recombination gives mutually consistent explanation for our dc and ac data.

Recently trap-assisted recombination of electron and holes was studied in MEH-PPV [11] by transport measurements and numerical simulations. It was demonstrated that the rate limiting step for this process is the diffusion of holes towards trapped electrons. The hole capture coefficient was estimated to be $C_p = 9.0 \times 10^{-19}\, m^3 s$ [13], and the trap density $N_t = 1.1 \times 10^{23}\, m^{-3}$ [12]. With these values the carriers lifetime associated with this process

was calculated to be $\tau_{tr} = (N_t C_p)^{-1}$ =10 μs, which is much smaller than the experimentally observed lifetime of 0.8 *s* in the present studies. The reason for such disagreement is not understood.

A different interpretation of the negative capacitance was recently proposed to explain the behavior of the admittance in PPV copolymer 'super yellow' [7]. In this work the negative capacitance was attributed to the sequential electron injection at the organic/metal interface. Intermediate states were attributed to a dipole layer at the interface between PPV and Ba electrode, which was used as a cathode material in this work. This mechanism could explain the C_1 term in our bipolar MEH-PPV devices, where a dipole layer can be formed at the PPV/Ca interface. However, as it is shown in Figure 6.4, the low-frequency negative capacitance was also detected in unipolar device E, where gold was used as a cathode material.

However, the effect of the magnetic field on the device in this frequency range is still to be explained. It is important to remind us at this point that the values of C_{10} and τ_1 reported here, are obtained with no constraint on the fitting parameters C_{10}, C_{20}, τ_1, τ_2, and α. More insight on the magnetic field effect on the diode at low frequency will be given in the next session.

Figure 6.5 and Figure 6.6 represent the admittance of device B just at several selected bias voltages. In fact, in the range from 0 to 6 *V*, the measurements were carried out with 0.2 *V* interval and we have much more data available for analysis. This allows showing that in the regime where the effect of magnetic field on the admittance of the device is detectable, the frequency-dependent response of the device to a small magnetic field (30 *mT* for sample B) is equivalent to the response to a small increase in the bias

voltage in zero magnetic fields. To illustrate this observation, two new parameters were introduced: the normalized derivative of the conductance ΔG_S and the normalized derivative of the capacitance ΔC_S defined as:

$$\Delta G_S(V,f) = \frac{1}{S}\frac{G(V_1,f) - G(V_0,f)}{G(V_0,f)}, \tag{6.30}$$

$$\Delta C_S(V,f) = \frac{1}{S}\frac{C(V_1,f) - C(V_0,f)}{G(V_0,f)}, \tag{6.31}$$

where $G(V,f)$ and $C(V,f)$ are, respectively, the experimental conductance and capacitance of the device at zero magnetic field, S is an adjustable scaling factor, $V_0 = V$, and $V_1 = V_0 + \delta V$ (in this experiment, $\delta V = 0.2\ V$).

These two parameters were calculated at different bias voltages and compared with the magnetoconductance $MG(V,f)$ and the magnetocapacitance $MC(V,f)$ of the biased device measured from the effect of 30 mT magnetic field on the biased device. For $V = 4.2\ V$ and $V = 5.8\ V$, Figures 6.15 and 6.16 show, respectively, the comparison between $\Delta G_S(V,f)$ and $MG(V,f)$ on one hand, and on the other hand, the comparison between $\Delta C_S(V,f)$ and $MC(V,f)$.

For $V = 4.2\ V$, we used the measured conductance and capacitance dependences $V_0 = 4.2\ V$ and $V_1 = 4.4\ V$. Similarly, for $V = 5.8\ V$, we used the measured conductance and capacitance dependences for $V_0 = 5.8\ V$ and $V_1 = 6.0\ V$.

For $V = 4.2\ V$, the same scaling coefficient $S = 2.1$ brings in good agreement the conductance parameters $MG(V,f)$ and $\Delta G_S(V,f)$, and the capacitance parameters $\Delta C_S(V,f)$ and $MC(V,f)$ as shown in Figure 6.15 (A) and Figure 6.16 (A), respectively.

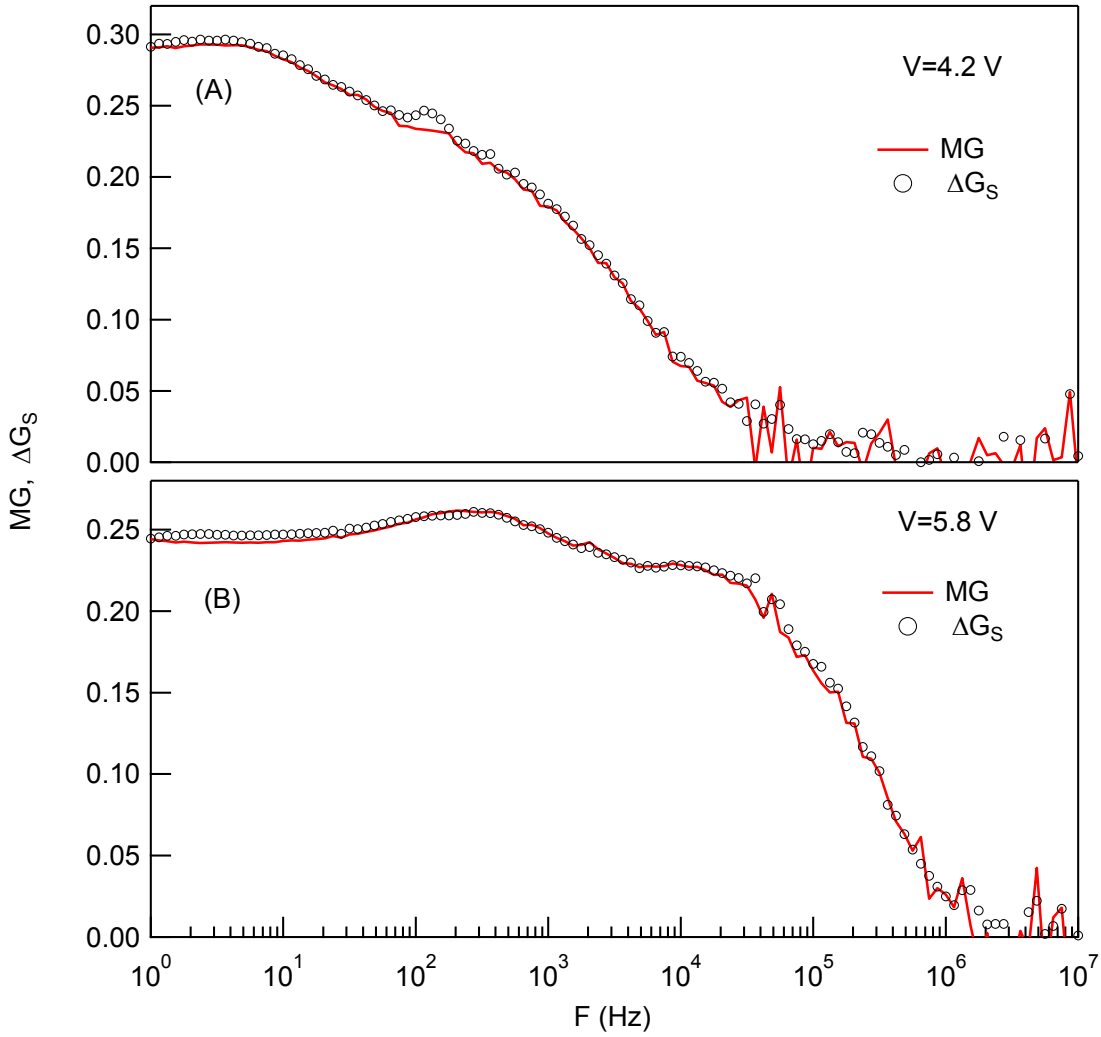

Figure 6.15: *Magnetoconductance, MG, and the scaled normalized derivative of the conductance at zero field, ΔG_S, as function of frequency for device B. At the bias voltage (A) 4.2V and (B) 5.8V*

At the applied voltage of 5.8 V, the conductance and capacitance parameters present an equally good agreement with the scaling coefficient $S = 1.75$. The quality of the agreement between $MG(V, f)$ and $\Delta G_S(V, f)$ is highlighted by their behaviors at 300 Hz at 5.8 V. At that point, the change in τ_2 due to the application of the magnetic field is represented by a broad peak. Similarly, $\Delta C_S(V, f)$ and $MC(V, f)$ agree well for the change in sign of the capacitance of the device at 300 Hz.

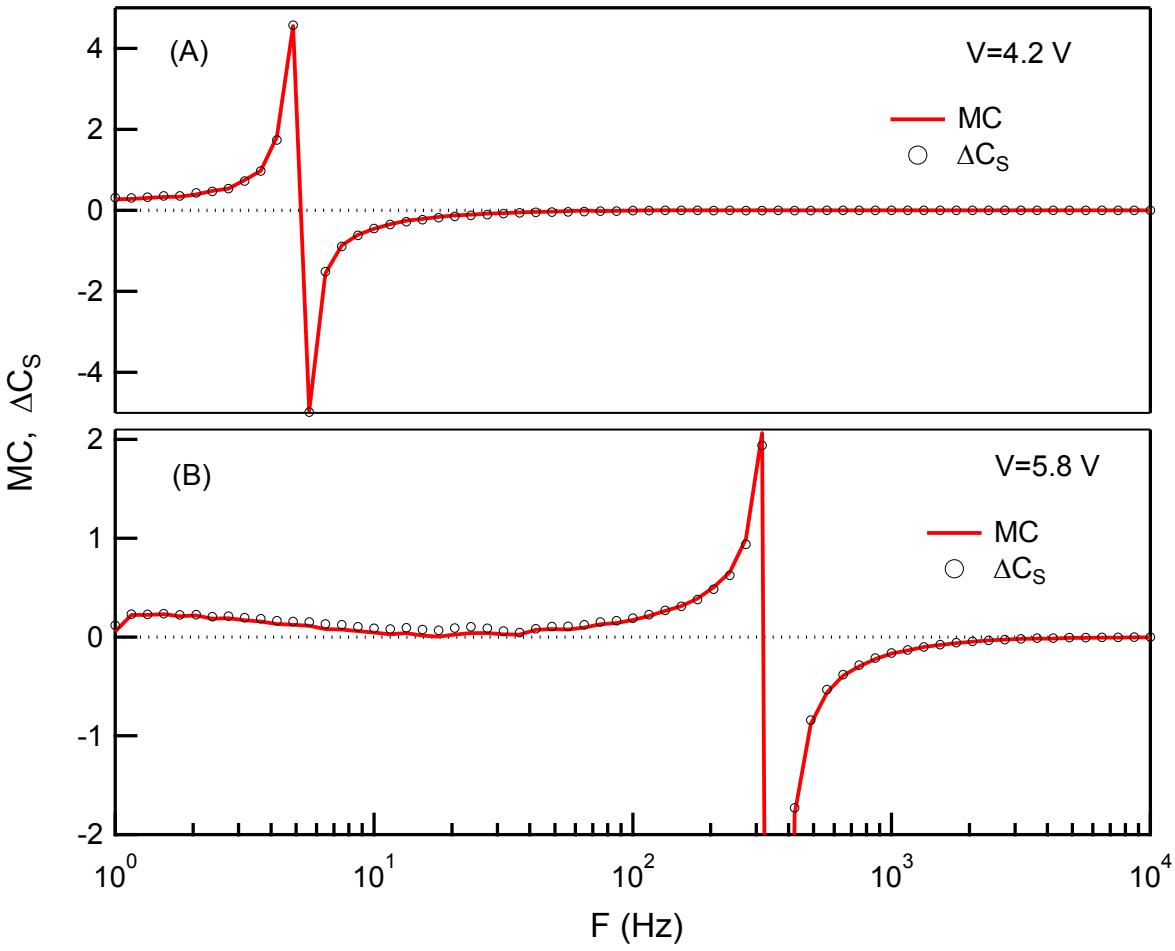

Figure 6.16: *Magnetocapacitance, MC, and the scaled normalized derivative of the capacitance at zero field, ΔC_S, as function of frequency for device B. At the bias voltage (A) 4.2 V and (B) 5.8 V*

6.3.2.3- Magnetic field induced transition from negative to positive capacitance in bipolar MEH-PPV and DOO-PPV diodes. The effect of the magnetic field on the differential capacitance of device B was observed in several samples having the same structure and different thicknesses. The variation of sign of the dynamical capacitance (C) vs. bias voltage (V) in the sequence positive – negative – positive and the sign change of the capacitance at low frequency under the action of a magnetic field are presented here.

- "positive-negative-positive" C vs. V. The differential capacitance of devices G (bipolar device made of 50 *nm* of MEH-PPV) is shown in Figure 6.17. Sample G is biased with a DC component and an AC component of amplitude 20 *mV* and a constant frequency of 3 *Hz*.

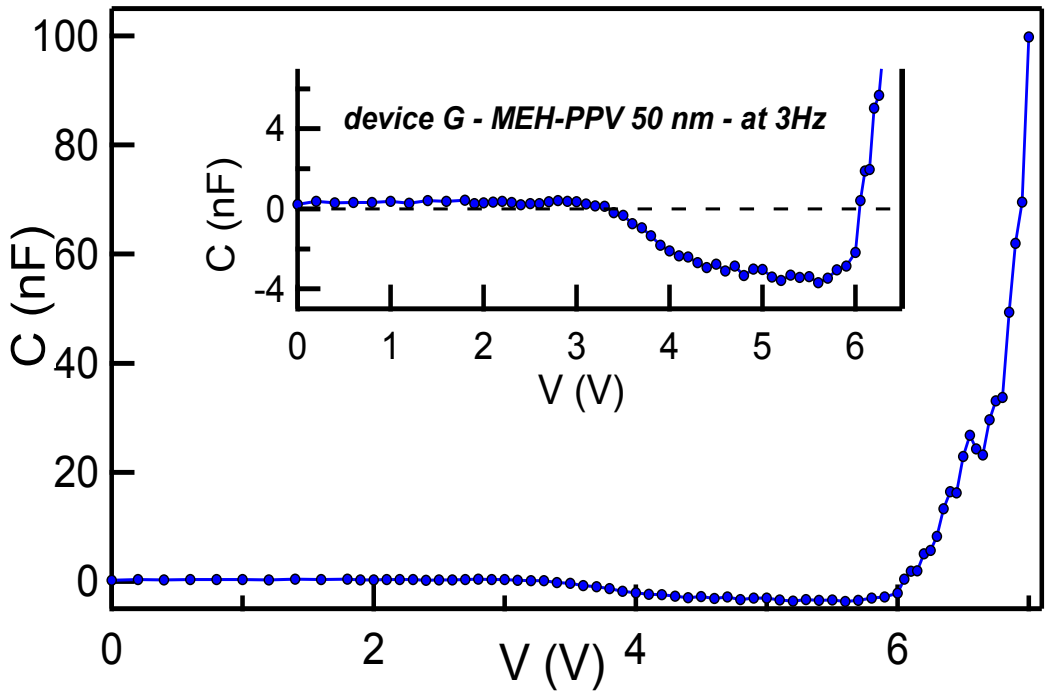

Figure 6.17: *Capacitance at 3 Hz as a function of bias voltage for device G (MEH-PPV thickness is 50 nm). The inset shows the same data on the magnified scale*

The measured capacitance is positive from 0.0 V to about 3.0 V, and then it gets negative up to 6 V, and becomes positive again for higher voltages. Its magnitude in the last regime strongly increases with bias: at 6.5 V, it reaches the high value of 100 nF.

J. Bisquert [7] observed similar "positive-negative-positive" behavior of C vs. V in OLEDs based on PPV copolymer "super yellow" and suggested that it originated from sequential electron injection through trap states at the interface PPV/Ba. In MEH-PPV OLEDs, negative capacitance with the same time constant was observed not only in bipolar devices but also in a unipolar device with the layer sequence ITO/PEDOT-PSS/MEH-PPV/Au. This suggests that if interface states are indeed responsible for C_1 regime, these should be states at the PEDOT-PSS/PPV interface. Efficiency of carrier injection from PEDOT-PSS is known to depend on chemical or ultraviolet light-ozone treatment, so this material likely has electrically active surface defects. Within the model proposed by Bisquert *et al*., negative capacitance occurs because the occupancy of intermediate interface states decreases with increasing bias. Then, it is noticeable that qualitatively similar effect may involve bulk traps, namely negative capacitance may occur if the occupancy of bulk trap states decreases with increasing bias. For example, this may happen if the trapped states act as centers of monomolecular recombination with a recombination rate that grows with bias faster than the trapping rate [9].

- Magnetic field dependent flip of differential capacitance from negative to positive at low frequency. The capacitance data of device F (160 *nm* MEH-PPV) are shown in Figure 6.18. As in the previous section, the effect of the magnetic field on the capacitance is well noticeable at low frequency. In this device, we can also distinguish C_1 and C_2 regimes. From the previous explanations and reference [4], the regime C_2 is caused by

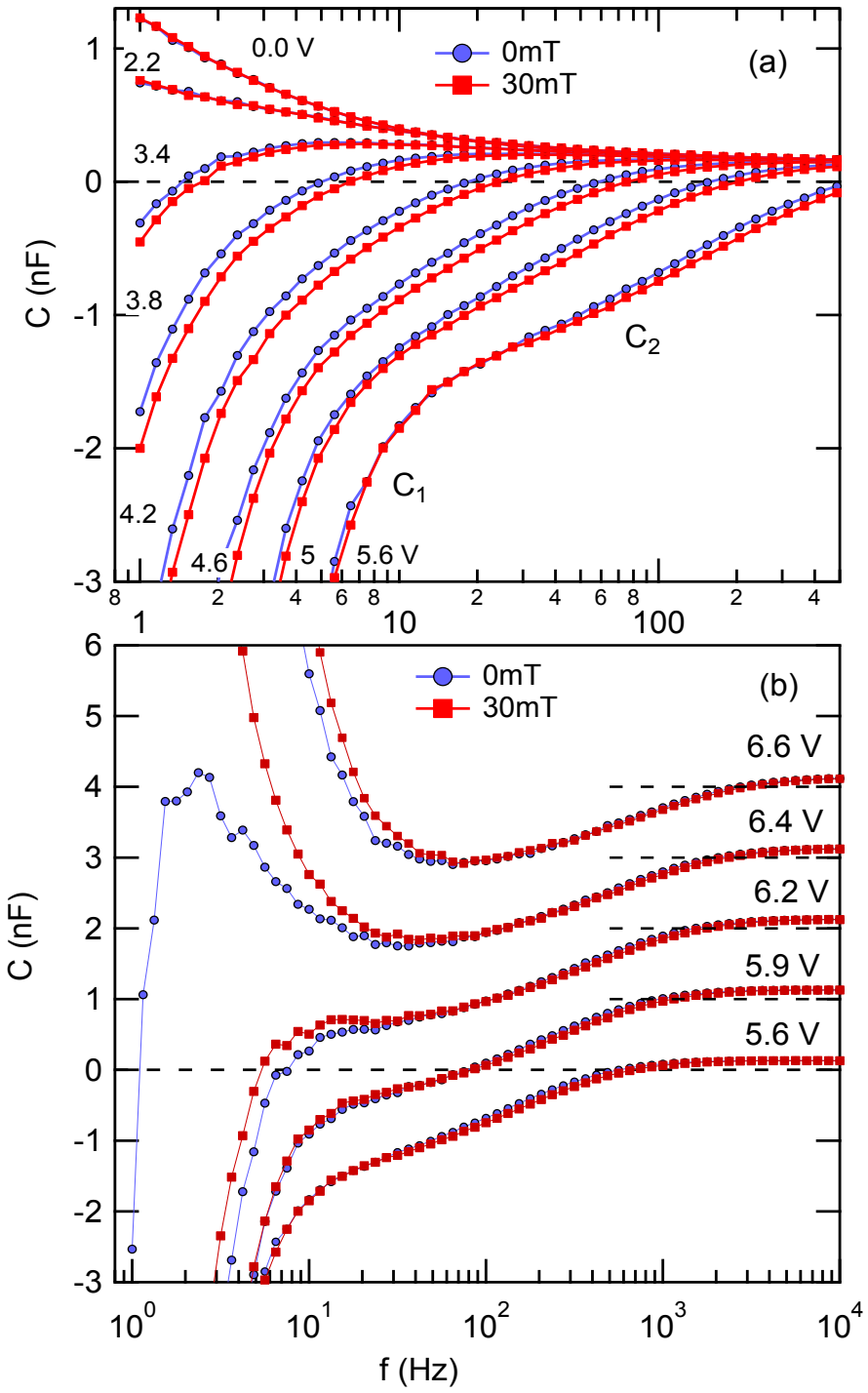

Figure 6.18: *Conductance of device F (thickness 160 nm) vs. frequency. (a) Low and intermediate bias regimes. (b) High bias regime. The data for indicated bias voltages are shifted for clarity. Dashed lines indicate level of zero capacitance.*

bimolecular recombination in the device that occurs mostly in the trap filled regime.

Through the polaron pair model of Prigodin [10], C_2 is subjected to the influence of the magnetic field. Similarly, a strong effect of the magnetic field on the capacitance of the device at frequencies less than 10 *Hz*, i.e., in C_1 regime, is observed. The relaxation time constant, $\tau_1 = 0.8\,s$ associated with the regime C_1 was calculated previously and in [4]. τ_1 showed neither bias voltage dependence, nor magnetic field dependence.

One of the main observations is that at 6.4 *V*, the negative capacitance is reversed under the influence of the magnetic field and became divergent positive. This point, where the reversal of the sign of the differential capacitance could be induced just by the magnetic field, was found in several samples. A better illustration is displayed in Figure 6.19. There, the effect of the magnetic field on the differential capacitance of device C, which is based on 150 *nm* MEH-PPV, is shown.

At 7.1 *V*, it was possible to tune the device C from a state where the differential capacitance is negative to a state where the capacitance is frequency independent by applying a magnetic field of 12 *mT*. The increase in magnetic field leads to a positive differential capacitance. The bias voltage at which this flip of capacitance induced by applied magnetic field occurs was investigated. Figure 6.20 highlights these positions.

In Figure 6.20, n is calculated according to equation (5.2). Similarly to transport regimes shown in the bipolar device B in Figure 5.1 (b), the bipolar devices shown in Figure 6.20 are all in ohmic regime at bias voltage less than the built-in potential, approximately 2 *V*.

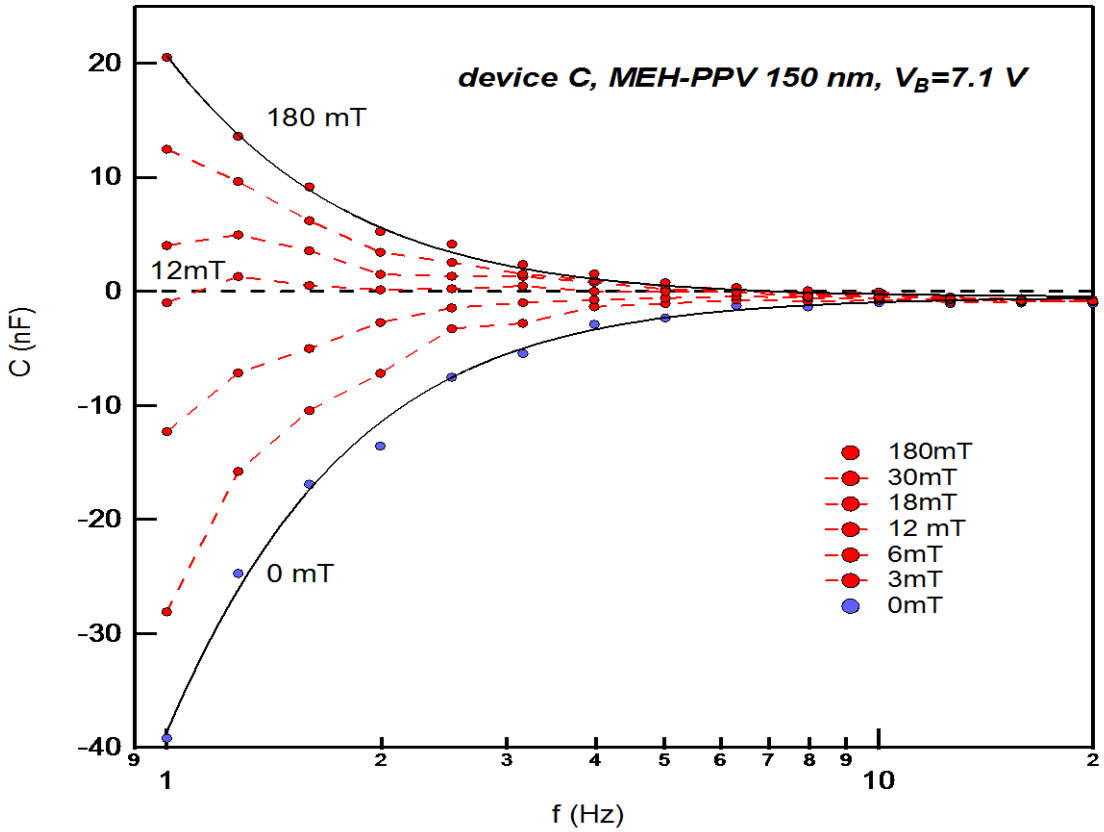

Figure 6.19: *Capacitance of device C (thickness 150 nm) at bias voltage 7.1 V vs. frequency at indicated magnetic fields. The solid black lines are theoretical fits to the data at B=0 mT and 180 mT.*

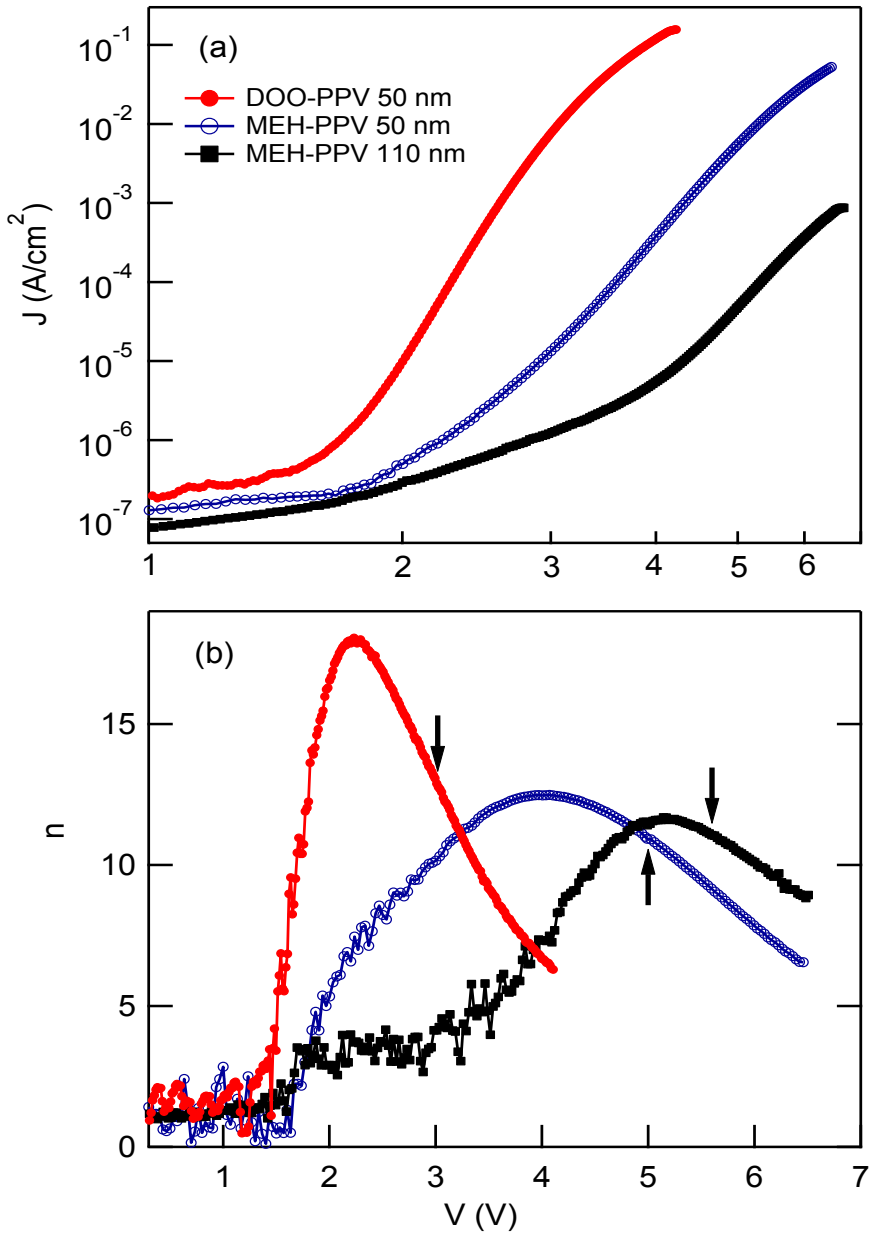

Figure 6.20: *(a) Current density vs. bias voltage for several studied OLEDs; (b) the parameter* $n = d(\ln(J))/d(\ln(V))$ *as function of bias for the same OLEDs. Vertical arrows indicate biases at which the capacitance reverses from negative to positive.*

At strong bias voltage, when the device goes to the bipolar SCLC, the application of the magnetic field can tune the state of the diode operation at low frequency from negative differential capacitance to a positive value.

In the low-frequency regime, the data C_1 were fitted using the equation:

$$C(\omega) = C_A + C_{10}\frac{1}{1+(\omega\tau_1)^2}\ , \tag{6.32}$$

where C_A is the sum of the geometrical capacitance and the capacitance due to relaxation processes in C_2.

Equations (6.32) fits C vs. f of Figure 6.19 at both 0 mT and 180 mT with fitting parameters $C_A = -500\,pF$ and $\tau_1 = 0.35\,s$.

The same equation was used to fit the C vs. f obtained for device H, which is 50 nm thick DOO-PPV based OLED. For this fitting, shown in Figure 6.21, we found that $\tau_1 = 0.4\ s$ and does not appreciably change with bias voltage. At 1 Hz and under a bias of 4.16 V, the capacitance of this sample is 17 μF, which is 10^5 times larger than its geometrical capacitance. The similarity between the value of τ_1 in MEH-PPV and DOO-PPV suggest that C_1 regime is likely related to trap states in these materials that have similar chemical and electronic structures.

The polaron-polaron (PP) model is found to be the most natural way to explain the response of the capacitance on the magnetic field. In bipolar MEH-PPV OLEDs, a small increase in a bias voltage increases the concentration of positive, n_+, and negative, n_-, polarons. (For example this is evident from the enhancement of electroluminescence.) Within the PP model, the effect of the magnetic field is to decreases the rate of bimolecular recombination, which allows the injection of more carriers, and as a result

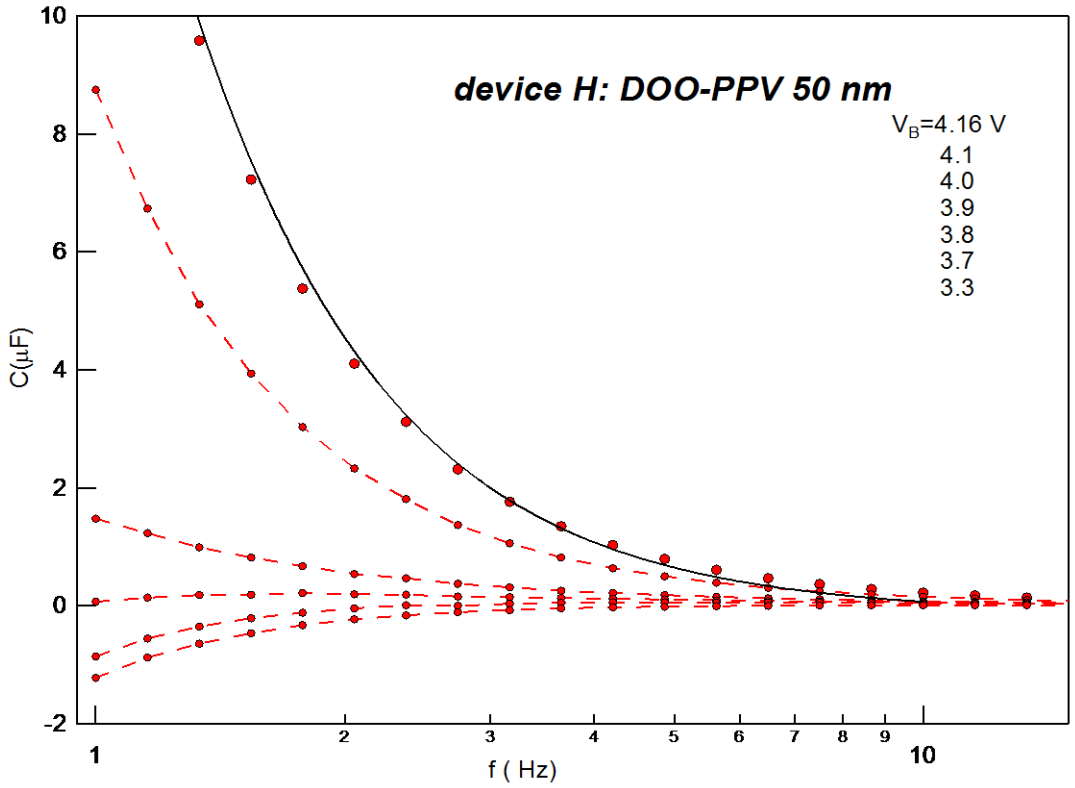

Figure 6.21: *Capacitance vs. frequency at indicated biases for device H with 50 nm-thick DOO-PPV active layer. The solid line is the theoretical fit to the data at* V_B *=4.16 V.*

increases n_+ and n_-. Then, the response of the system to AC electrical filed (which involves several processes and can be rather complicated) simply reflects the changed carrier concentration regardless of what causes it, magnetic field or increased bias voltage. It is interesting to notice that even though the low-frequency term C_1 is strongly affected by magnetic field, within the PP model an elementary physical process responsible for C_1 does not need to depend on B. For example, it can be assumed following Bisquert *et al.* [7] that C_1 is determined by the occupation of surface defects, n_S.

However, n_S is in steady state equilibrium with bulk free carriers. So even though the elementary charge transfer between a surface site and a site in the bulk may not

depend on B, the effect of magnetic field can occur indirectly through the magnetic field dependence of the bulk carrier concentration [9].

6.3.3 Bipolar devices without PEDOT-PSS

The main consequence of the absence of PEDOT-PSS in the device is the reduction of hole concentration in the device, and as result the reduction of the total current. A comparison between samples I (without PEDOT-PPV) and B (with PEDOT-PSS), both having 150 *nm* thick MEH-PPV layer, shows that in sample I maximum of MG occurs at 7 V and is about 9 %, whilst for sample B, the maximum of MG occurs at 4.8 V and is about 35 %. The C vs. f plotted in Figure 6.7, shows that the capacitance is negative at $f <$ 10 Hz and bias voltage above 5.8 V. The "positive-negative-positive" behavior of the C vs. V was not observed in this sample for the range of applied voltage used. A regime similar to C_2 observed in bipolar sample with PEDOT-PSS is not detectable in device in the bias voltage applied. Although the effect of the magnetic field on the capacitance is well displayed, the change in sign of the magnetocapacitance was not observed. The presence of OMAR effect in this sample, which differs from sample B by one interface, shows that OMAR effect is related to the bulk of the device and not the layers interfaces.

6.4 References

1. C.J.F. Bottcher and P. Bordewijk, "Theory of electric polarization," vol.2, Elsevier (1978).

2. M. Ershov, H.C. Liu, L. Li, M. Buchanan, Z.R. Wasilewski, and K. Jonscher, "Negative capacitance effect in semiconductor devices," IEEE Trans. Electron Devices **45,** 2196 (1998).

3. E. Ehrenfreund, C. Lungenschmied, G. Dennler, H. Neugebauer, and N.S. Sariciftci, "Negative capacitance in organic semiconductor devices: bipolar injection and charge recombination mechanism," Appl. Phys. Lett. **91**, 012112 (2007).

4. T.K. Djidjou, T. Basel, and A. Rogachev, "Admittance spectroscopy study of polymer diodes in small magnetic fields," J. Appl. Phys. **112,** 024511 (2012).

5. H.H.O Gommans, M. Kemerink, and R.A.J. Janssen, "Negative capacitances in low-mobility solids," Phys. Rev. B. **72,** 235204 (2005).

6. H.C.F. Martens, H.B. Brom, and P.W.M. Blom, "Frequency-dependent electrical response of holes in poly(*p*-phenylene vinylene)," Phys. Rev. B. **60**, R8489 (1999).

7. J. Bisquert, G. Garcia-Belmonte, A. Pitarch, and H. J. Bolink, "Negative capacitance caused by electron injection through interfacial states in organic light-emitting diodes," Chem. Phys. Lett. **422**, 184 (2006).

8. N.D. Nguyen, M. Schmeits, and H.P. Loebl, "Determination of charge-carrier transport in organic devices by admittance spectroscopy: application to hole mobility in α-NPD," Phys. Rev. B **75**, 075307 (2007).

9. T.K. Djidjou, T. Basel, and A. Rogachev, "Magnetic-field dependent differential capacitance of polymer diodes," Appl. Phys. Lett **101,** 093303 (2012).

10. V. N. Prigodin, J. D. Bergeson, D. M. Lincoln, A. J. Epstein, "Anomalous room temperature magnetoresistance in organic semiconductors," Synth. Met. **156**,757 (2006).

11. M. Kuik, L.J.A. Koster, G.A.H. Wetzelear, and P.W.M. Blom, "Trap-assisted recombination in disordered organic semiconductors," Phys. Rev. Lett. **107**, 256805 (2011).

12. H.T. Nicolai, M.M. Mandoc, and P.W.M. Blom, “Electron traps in semiconducting polymers: exponential versus Gaussian trap distribution,” Phys. Rev. B **83**, 195204 (2011).

13. M.Kuik, H.T. Nicolai, M. Lenes, J.A.H. Wetzelear, M. Lu, and P.W.M. Blom, “Determination of the trap-assisted recombination strength in polymer light emitting diodes,” Appl. Phys. Lett. **98,** 093301 (2011).

CHAPTER 7

CONCLUSIONS

Understanding the mechanism of organic magnetoresistance in polymer diodes on different time's scales was the motivation of this work. It required an understanding of the polymer based OLEDs under the action of DC bias, and DC plus AC bias.

In this thesis, we studied the effect of small magnetic fields on MEH-PPV based organic light emitting diodes using admittance spectroscopy in the frequency range 1 $Hz < f < 10\ MHz$ at room temperatures. The magnitude of the magnetic field varies from 0 mT to 180 mT. The devices measured were in two configurations: unipolar where we assumed only holes as charge carriers, and bipolar where the carriers are electrons and holes polarons.

The DC measurements performed on the unipolar samples revealed an ohmic regime at bias voltage less than 1 V, followed by a trap filling regime up to 3 V and a space charged trap free limited regime above 5 V. This is in good agreement with the theory of single carrier injection into semiconductors. The effect of the magnetic field on the unipolar samples was not detected, leading us to conclude that the bipolaron model was not appropriate to explain the OMAR mechanisms in our devices. For the bipolar samples where PEDOT-PSS was inserted between ITO and the

electroluminescent polymer (MEH-PPV, DOO-PPV), we noticed four distinguishable transport regimes, i.e., an ohmic regime at bias voltage less than 1.7 V followed by space-charged limited regime due to electrons in presence of traps up to a bias voltage almost equal to 3 V. At bias voltage ranging from 3 V to 5 V, we noticed an exponential increase in current due to bipolar injection. This is followed by another space-charged regime in presence of electrons and holes. The effect of the magnetic field on bipolar devices was measured and the data were fitted with a non-Lorentzian function. The quarter-saturation field for our data was found to be 2.5 mT, a value not in the predicted range of 3 mT to 6 mT. In the bipolar sample without the buffer PEDOT-PSS layer, the current was one order of magnitude less than in the similar sample with PEDOT-PSS. This sample is in the ohmic regime when the applied voltage is less than 1 V. Then it is in SCL regime up to 1.7 V. Above 1.7 V, we noticed that a strong fluctuation in the transport regime; this may be cause by the interface ITO/MEH-PPV.

The admittance measurements performed on all samples show a conductance almost independent of the frequency in an interval of frequencies which shift to higher values with the increase of bias voltage. At high frequencies, all conductance curves merged into a single curve. The reason for this behavior is that at high frequencies, all conductive processes associated with injected carriers are shorter by the dissipative processes that are present in unbiased samples. These high-frequency processes are likely related to the depolarization of permanent dipoles. The data show that the bipolar sample with PEDOT-PSS experienced the strongest OMAR effect, of approximately 35% at 4.8 V when a magnetic field of 30 mT was applied. In a bipolar

sample with PEDOT-PSS, we observed that the conductance at 10 *MHz* was enhanced by 4.5% when a magnetic field of 30 *mT* was applied. We found that the differential capacitance of bipolar devices contains two negative contributions that are affected by the magnetic field. The first contribution that occurred at frequencies below 10 *Hz*, is likely associated with trap-associated recombination. The second contribution, which is associated with the bimolecular electron-hole recombination, dominates the negative capacitance above 10 *Hz*. We found that its time constant, τ_2, exponentially decreases with the bias voltage. Application of a magnetic field of 30 *mT* decreases τ_2 by 30%. At low frequency, we observed that the capacitance of the device structured as ITO/PEDOT-PSS/MEH-PPV/Ca/Al is divergent and sequentially changes its sign with increasing bias voltage, from positive to negative and to positive again. By carefully selecting the bias voltage, we were able to tune some diodes of this configuration from the state of negative capacitance to positive capacitance by applying the magnetic field only. We found that the polaron-pairs model is the most natural way to explain the response of the capacitance on the magnetic field. In fact, within this model, magnetic field decreases the rate of bimolecular recombination, allows for more injection, and consequently increases the concentrations of positive and negative polarons. We also found that the frequency-response of the device to a small magnetic field is equivalent to the response to a small increase in the bias voltage at zero magnetic field.